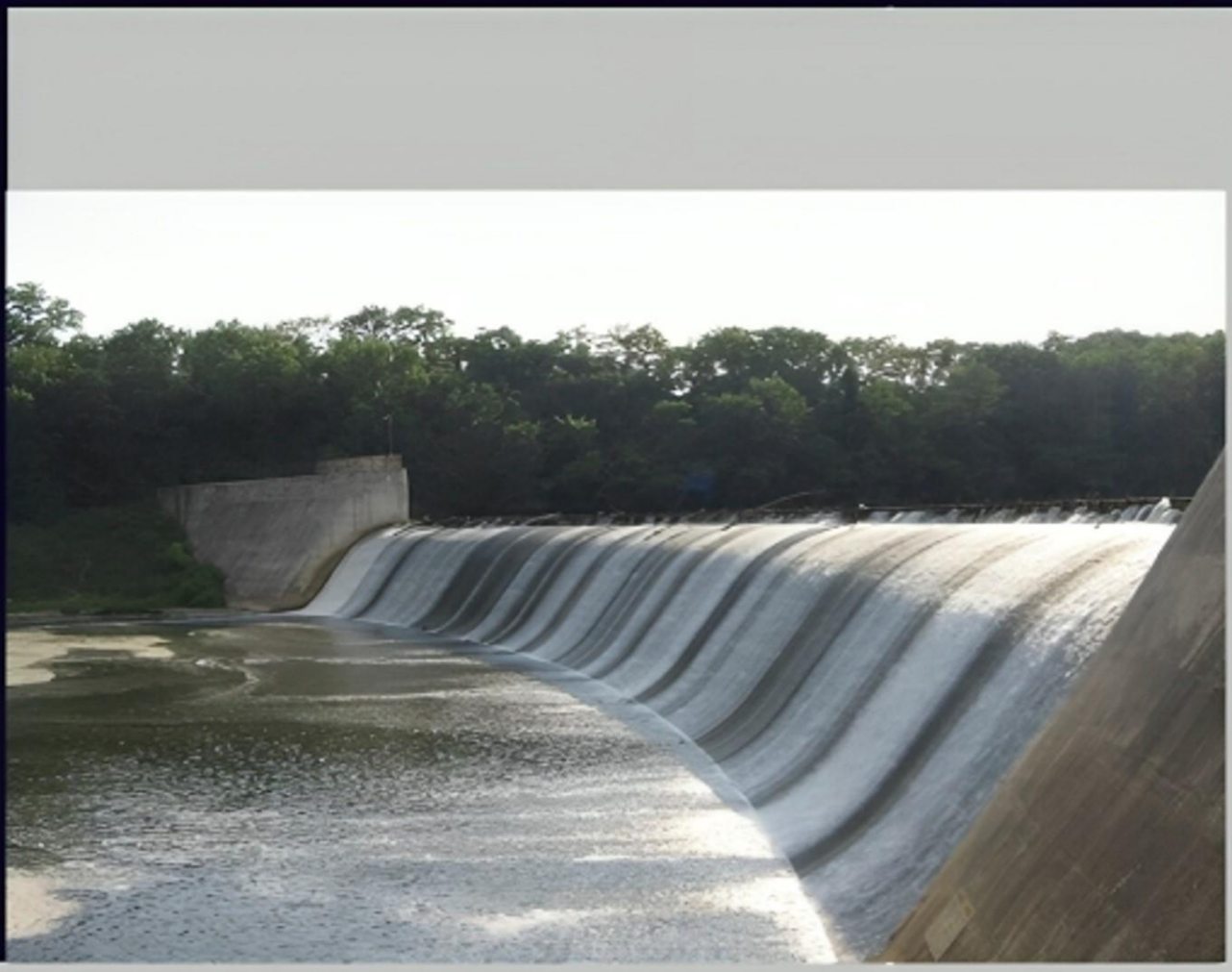
Iranian Hydraulic Association

Shahid Chamran University of Ahvaz

Journal of Hydraulic Structures

Scientific Professional Journal



January 2024
Volume 10, Issue 1

ISSN (Online): 2345-4156
https://jhs.scu.ac.ir/

Aims and Scope

Journal of Hydraulic Structures is an interdisciplinary journal which publishes high-quality peer-reviewed articles addressing the latest developments and applied methods in analysis and design, construction, maintenance, management, and operation policy of Hydraulic Structures.

The Journal aims at providing an efficient route to fast-track publication, within 10-12 weeks after manuscript submission.

The general areas covered by the Journal include:

- Advances in numerical and analytical methods applicable to hydraulic structures
- Hydro informatics and soft computing
- Hydraulic aspects of hydraulic structures
- Applied surface and subsurface hydrology and hydrometeorology
- Forecasting approaches in water resources engineering
- Economic and social aspects of hydraulic structures
- Uncertainty analysis and risk management in hydraulics and water resources engineering
- Application of Nanotechnology in hydraulic structures
- Geotechnics of hydraulic structures
- Damage detection techniques
- Technical and methodological advances in application, design/selection, production, construction materials of hydraulic structures.
- Application of Artificial Intelligence techniques in all aspects of hydraulic structures.

General Information:

Title: Journal of Hydraulic Structures

Publisher: Shahid Chamran University of Ahvaz

ISSN (Print): 2345-413X

ISSN (Online): 2345-4156

Website: https://jhs.scu.ac.ir/

Address: Faculty of Civil Engineering and Architecture, Shahid Chamran University of Ahvaz, Ahvaz, Iran

Email: jhs@scu.ac.ir

Journal of

Hydraulic Structures

Shahid Chamran University of Ahvaz

Director-in-Charge: Prof. Ali Haghighi

Editor-in-Chief: Prof. Hamid R. Ghafouri

Managing Editor: Dr. Amir H. Shafiee

Contents:

01

Using PAT for Energy Recovery and Pressure Reduction in Water Distribution Networks

Hamed Mohammadi; Mahnaz Ghaeini-Hessaroeyeh; Ehsan Fadaei-Kermani

13

Experimental evaluation of dune formation downstream of pier scour hole with upstream debris accumulation

Ali Mahdian Khalili; Pouria Akbari Dadamahalleh; Mehdi Hamidi

29

Investigating the settlement of the stone boulders breakwater located on the marine soft fine-grained soil

Amin Falamaki; Amir Hossein Shafiee; Jamal al-Din Iranmahboob; Farzad Arjmand

46

Investigation of the Performance of Soft Computing Methods in the Hydraulic Evaluation of the Slot Fishway on the Inclined Drop

Ehsan Aminvash; Farhoud Kalateh; Rasoul Daneshfaraz; John Abraham

66

Hydraulic Response to Geometry: Finite Element Modeling of Underground Spaces in Saturated Environments

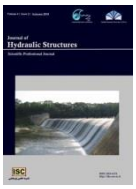
Hadi Farhadian; Zahra Gholami

80

Integrated Hydrodynamic Modeling of Dam Failure and Downstream Flood Inundation near Kathmandu, Nepal using MIKE Hydro River Model

Kuldeep Pareta

Journal of Hydraulic Structures
J. Hydraul. Struct., 2024;10(1):1-12
DOI: 10.22055/jhs.2024.45699.1279



OPEN ACCESS

Using PAT for Energy Recovery and Pressure Reduction in Water Distribution Networks

Hamed Mohammadi [1]
Mahnaz Ghaeini-Hessaroeyeh [2]
Ehsan Fadaei-Kermani [1]

Abstract

Leakage is one of the main problems of urban water distribution networks. Leakage control and management can play an important role in increasing network efficiency and reducing water loss. Pressure reduction in water distribution networks is usually done using Pressure reducing valve (PRV), while the energy dissipated from head loss can be recovered to generate hydropower. In this study, the possibility of using pump as turbines (PATs) instead of PRVs in a water distribution network has been investigated. Regarding this purpose, the genetic algorithm is used by MATLAB software, in which the hydraulic model of the water distribution network is carried out in WaterGEMS software. At first, the aim of optimization is to determine the optimum output of PRVs. Then after replacing the PRVs with the PATs, the optimal curve for the PATs can be determined. Results show that the use of PATs to control the pressure is effective, so that compared to the basic model, the leakage rate has decreased by about 33% and the Nodal Pressure Reliability Index (NPRI) has increased by 0.41. Moreover, the nodal pressures have been significantly reduced, and the average pressure of the network decreased by 58%.

Keywords: Leakage; Water Distribution Networks; PRVs; PATs; Genetic Algorithm.

Received: 21 January 2024; Accepted: 14 March 2024

1. Introduction

Water leakage is a common problem in many aging urban water networks. A worldwide average of 45 to 88 million cubic meters of water is lost during every day due to leaks in Water Distribution Networks (WDNs) [1]. In leakage management studies, pressure management is the simplest, fastest, and most economical method to reduce leakage. The control of pressure is one of the primary concerns in water distribution networks. High pressure values increase both leakage and risk of pipe damage, while low pressure may reduce water supply for consumers. As

[1] Department of Civil Engineering, Faculty of Engineering, Shahid Bahonar University of Kerman, Kerman, Iran.
[2] Department of Civil Engineering, Faculty of Engineering, Shahid Bahonar University of Kerman, Kerman, Iran. Email: mghaeini@uk.ac.ir **(Corresponding Author)**

a result, excess pressure on systems must be reduced to standard range. Utilization of a Pressure Reducing Valve (PRV) to maintain standard pressures has been a common way for this purpose [2]. A PAT can be used instead of a PRV to produce hydropower energy and to control pressure. The use of renewable energy is increasing due to concerns about climate change and global warming. One of the renewable energies is hydropower, which derives energy from falling or running water which can be harnessed for useful purposes [3]. Micro Hydro Power (MHP) is another branch of hydropower; its capacity differentiates it from other branches. The application of MHP is in the class of small-scale hydropower projects. Pump as turbine (PAT) is one of the (MHP) projects that can be use instead of a Pressure Reduce Valve (PRV) in water distribution networks [4].

Due to the dynamic action of the fluid flowing through rotating elements, energy is continuously transferred in turbo machinery. Therefore, it is possible for the turbomachines to be used in reverse. A PAT is a turbine that works in a way similar to pumps [5]. In this mechanical device, water flow is used to generate electricity instead of energy to boost water flow. As a PAT works similarly to a regular pump, its implementation in the network does not require numerous modifications. Additionally, PATs' maintenance operations do not require specially trained personnel. The advantages of PATs utilization in water networks have been evaluated in various studies. The results have shown that PATs can be a reasonable alternative in a water distribution network. Fecarotta et, al [6] investigated the feasibility of hydropower potential in a water distribution network. The research results demonstrated that the installation of hydropower can produce interesting economic benefits. Morani et, al [7] introduced a novel mixed integer non-linear approach to find the optimal locations of both pressure reducing valves and pumps as turbines. The results showed that the proposed model can lead to good solutions, in term of energy and water saving purposes. Fontana et, al [8] investigated and analyzed various layouts for the installation of PATs in water distribution networks. They presented the procedure to determine the most appropriate and effective installation layout respect to different head and flow patterns. Pillay et, al [9] investigated the feasibility analysis of recovering energy in water distributions networks using PATs. They applied EPANET software to determine the strategic adjustment of PATs in water distribution networks. This study investigates the possibility of replacing PRVs with PATs using in a real water distribution network. Fernández García et, al [10] determined the optimal location and number of PATs in an irrigation network. They tried to maximize the amount of energy recovered by installation of PATs. The results showed that by using PATs, in addition to recovering energy, a significant amount of Co2 emissions can be saved. Stefanizzi et, al [11] presented an optimal strategy for hydraulic energy harvesting in water distribution networks by installing PATs. They proposed two new approaches for PAT selection according to maximum available energy, average flow rate and maximum energy recovery. Results showed that over 3.5 MWh per day was achieved by utilizing PATs.

In the present study, the feasibility of using PATs for pressure control in water distribution networks is investigated. Using WaterGems software, the Baharan network located in Sanandaj city in Iran is simulated. For this purpose, three scenarios have been defined to compare and evaluate the effect of PRVs and PATs on leakage reduction, pressure control and recovering energy.

2. Case study and methodology

For the purpose of evaluating the effectiveness of the suggested method and the importance of applying PRVs and PATs in controlling pressure (minimizing leakage) and producing energy, the proposed method has been exerted to a water distribution network. It is called the Baharan network, located in the city of Sanandaj, Iran. The city is located in the foothills of the Zagros Mountains. As it is restricted by mountains, the city contains large height differences. The Baharan network is located in northwest Sanandaj which is supported by a reservoir that located 1,541 meters above sea level. The elevation changes between 1,430 and 1,1488 meters above sea level. The high-altitude difference observed causes the city's WDN to be under high pressure as a result of gravity. The water distribution system consists of 121 pipes and 113 nodes. The pipes are made of asbestos cement, cast iron, ductile iron and polyethylene with diameters between 63 and 500 mm. The water distribution network has been divided into four District Metered Areas (DMAs). dividing a water distribution network into DMAs can be assumed as one of the most efficient and cost-effective methods of optimizing the performance of a water distribution network in terms of reducing the real water loss rates [12]. Segmenting the network has been accomplished by installing isolation valves in pipes that define DMA boundaries. A PRV or PAT can only be installed in pipes that supply water to one or more DMAs. Figure 1 shows the Baharan WDN. The elevations of the network nodes have also been demonstrated in Figure 2.

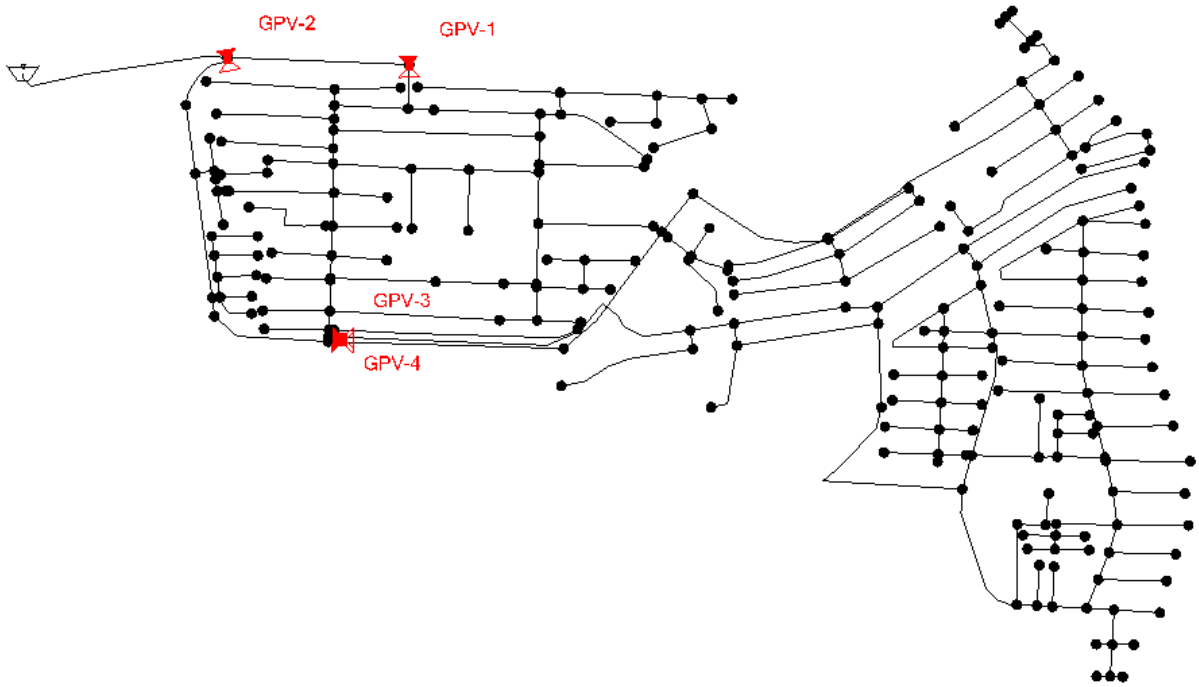


Figure 1. The Baharan layout of water distribution network

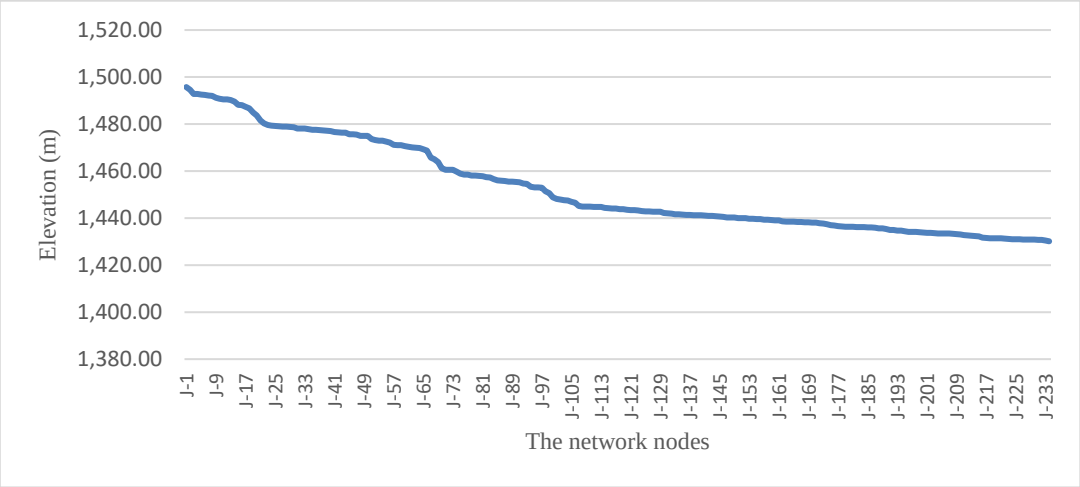


Figure 2. The elevation of the network nodes

Three scenarios were developed for comparing PRV and PAT implementations in the Baharan water distribution network. All the scenarios happened on the same pressure zones. In scenario 1, no PRVs or PATs are placed in the entrance of pressure zones. In scenario 2, PRVs are placed in the entrance of pressure zones for the PRVs performance a pattern is defined for different times. In scenario 3, the PRVs are being replaced by PATs, in exact same point where the PRVs were installed in previous scenarios. WaterGEMS software was used to evaluate each scenario separately, and results were compared. There are two explanations of numerical water distribution system modeling including steady-state analysis and extended period analysis [13,14]. In case of extended period analysis, computations are performed over an extended time period at variables water consumption and system operating conditions [15]. In the present study, the extended period analysis has been applied to the Baharan WDN. The population density of the study area is 321 people per hectare, and the consumption of water is considered to be 200 liters per capita per day (LPCD). Figure 3 shows the demand pattern considered for the simulation. The consumption coefficient has been determined according to hourly fluctuations in water consumption levels during day and night.

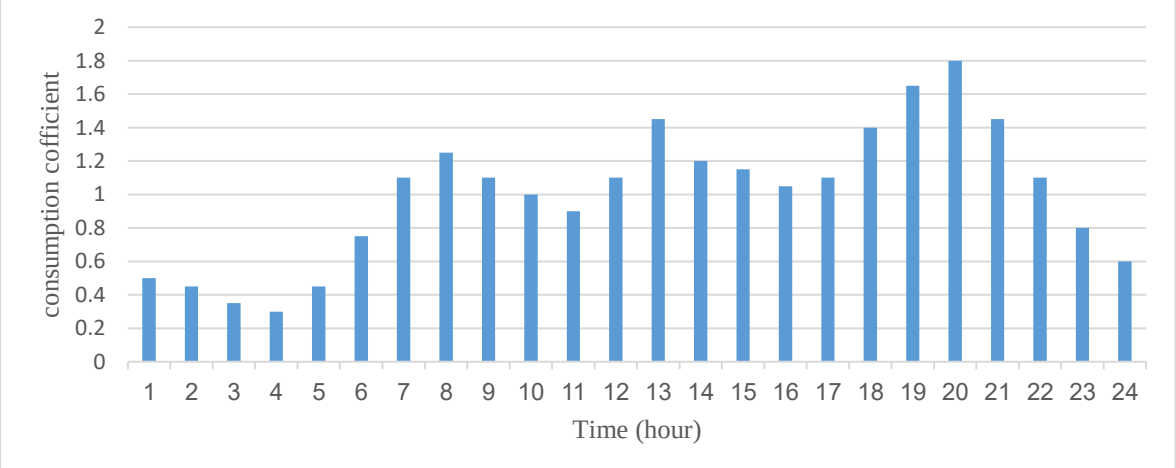


Figure 3 The demand pattern of the case study

3. Hydraulic modeling

The present study proposed a procedure to choose and define the optimum scheduling for PATs and PRVs separately, in order to maximize network node pressure reliability and minimize network leakage. The metaheuristic algorithm GA is utilized to maximize the benefits of network node pressure reliability and leakage reduction. The objective function used to evaluate network reliability is as follows:

$$NPRI(j,t) = \begin{cases} 0, & p < 10 \\ \frac{1}{32}(p-10), & 10 < p < 26 \\ \frac{1}{10}(p-26)+0.5, & 26 < p < 31 \\ 1 & p = 31 \\ -\frac{1}{38}(p-31)+1, & 31 < p < 50 \\ -\frac{1}{40}(p-50)+0.5, & 50 < p < 60 \\ 0.25, & 60 < p \end{cases} \quad (1)$$

where NPRI (j,t) is the value of the Nodal Pressure Reliability Index at node j and time t which is utilized to evaluate the reliability of WDN. p refers to nodal pressure in node j respect to time t. The network nodal pressure index of reliability is obtained from relation 2 [16]:

$$NPRI = \frac{\sum_{j=1}^{NN} Q_{j,t}^{req}(NPRI(j,t))}{\sum_{j=1}^{NN} Q_{j,t}^{req}} \quad (2)$$

where NPRI is the index of network nodal pressure reliability, NN is number of junctions in network, and $Q_{j,t}^{req}$ refers to water demand in junction j at time t. The following equations have also been used to calculate leakage of WDN and the amount of energy recovered by PATs [17]:

$$Q_l = cp^n \quad (3)$$

Where p is pressure head, Q is leakage flow rate, c refers to the coefficient of leakage, and n is leakage exponent. The n parameter can take values between 0.5 and 2.5, depending on WDN conditions such as leak hydraulics, soil properties, behavior of pipe material, and water demand. In the present paper, due to the conditions of the studied network, the n exponent has been considered equal 1.15. The turbine production power can be determined as following equation [18]:

$$P_{output} = \eta \rho g H Q \quad (4)$$

Where the flow rate Q and head H can be calculated from the site while density ρ, the turbine efficiency η and acceleration due to gravity g are constants.

4. Optimization Algorithm

In optimization problems, the Genetic Algorithm (GA) is one of the most popular optimization algorithms. It is a search heuristic algorithm which is inspired by the biological evolution process. the algorithm deals with the definition of problem variables as binary strings identified as genes. A set of genes forms a chromosome which can be considered as one of the possible solutions of the optimization problem. The process is continued until the search tends to an optimal solution. At first in the GA, randomly created primary populations of chromosomes are generated. Then the objective function is employed to find the fitness of each chromosome. The chromosomes with the better fitness amongst the population can be obtained by the selected operator. By use of mutation and crossover operators, a new population is generated. The iterative loops should be performed till the termination criterion is met [19]. The GA is being widely utilized to deal with WDN problems, including optimal network design pump scheduling and network calibration [20-23]. In this paper, the genetic algorithm is utilized for optimal setting of PRVs and PATs to maximize the network nodal pressure reliability index (NPRI), and minimize leakage in a WDN. It is to be mentioned that the pressure in each node should not overstep the corresponding standard pressure. In WaterGEMS, the Darwin Designer is applied for optimization purposes using the GA. It can enable designers to optimize either a whole WDN or a portion of it. The parameters of the GA are utilized to control the underlying algorithm used in the process of optimization [24].

5. Results and Discussion

The simplest, fastest, and most economical way to reduce leakage is to manage pressure value in water distribution networks. In the present study, the possibility of using pump as turbines (PATs) instead of pressure reducing valves (PRVs) has been investigated. For this purpose, the results of each scenario have been presented in low, medium and maximum consumption hours, and the results have been compared with each other. The results of each scenario have been presented in Table 1. Besides, figure 4 shows the nodal consumption discharge with and without PATs installation.

Table 1. Leakage and nodal reliability index (NPRI) for each scenario

	Scenario1		Scenario2		Scenario3	
Time	Leakage (L/s)	NPRI	Leakage (L/s)	NPRI	Leakage (L/s)	NPRI
4 A.M	56.64	0.28	39.42	0.7	35.22	0.67
10 A.M	56.22	0.28	40.68	0.67	37.59	0.71
8 P.M	55.32	0.3	44.07	0.67	41.22	0.69

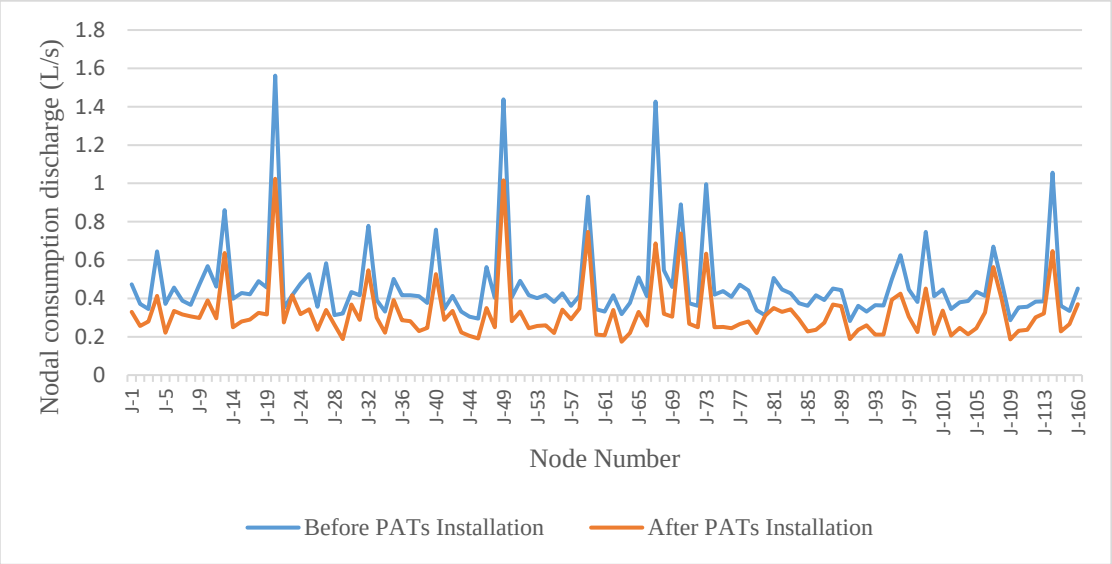


Figure 4. Nodal consumption discharge with and without PATs

According to Table 1, the amount of leakage in scenario 2 decreased by 26% compared to the scenario 1, and the NPRI increased by an average of 0.39. Moreover, in scenario 3, the leakage decreased by 32% compared to the first scenario and the NPRI value increased by 0.41. Figure 5 shows the amount of pressure in scenarios 1 to 3 at maximum consumption hours.

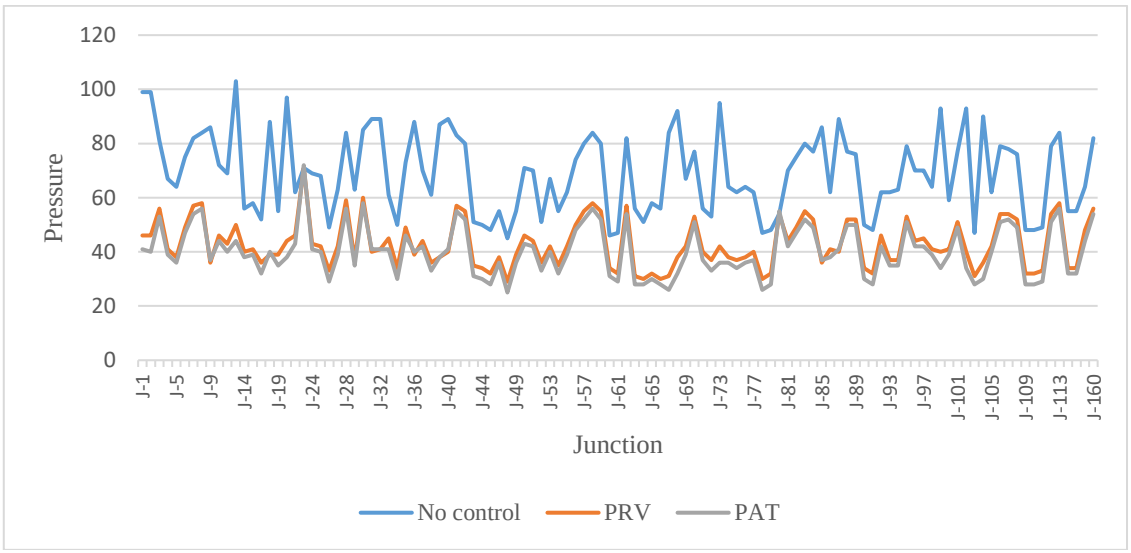


Figure 5. The junction pressure values at maximum consumption hours

According to the figure 5, the use of PATs instead of PRVs has a significant effect in controlling and reducing the pressure in the WDN. Figure 6 to 9 show the production power of the PATs in 24 hours. Moreover, the annual recovered energy of each PAT has been presented in table 2. As can be seen, the most energy produced in 24 hours belongs to peak consumption hours.

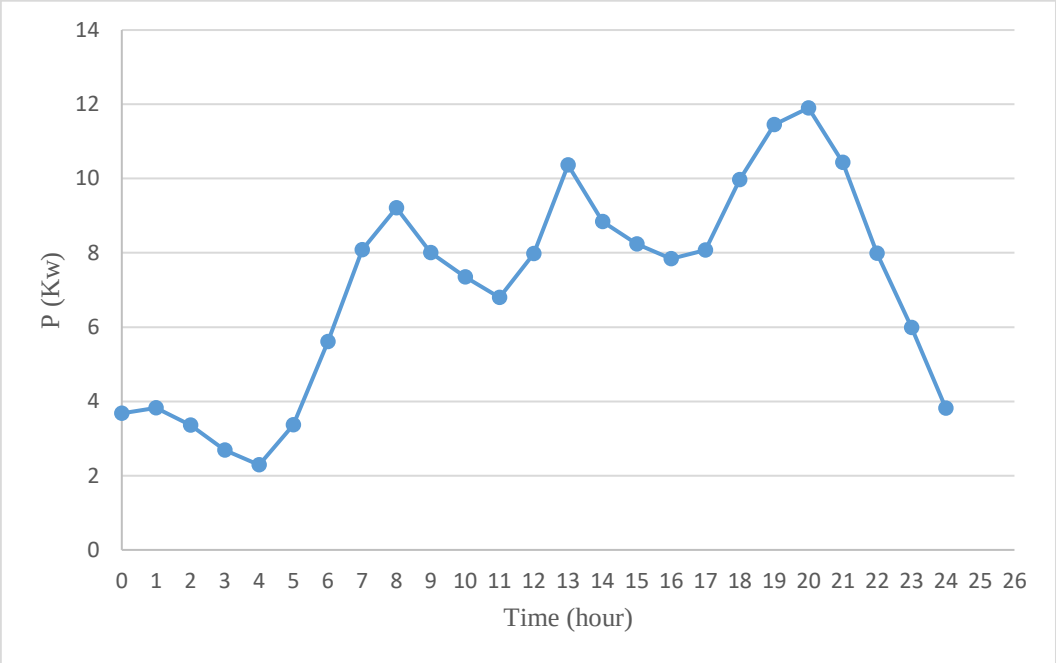


Figure 6. The production power of the PAT 1 in 24 hours

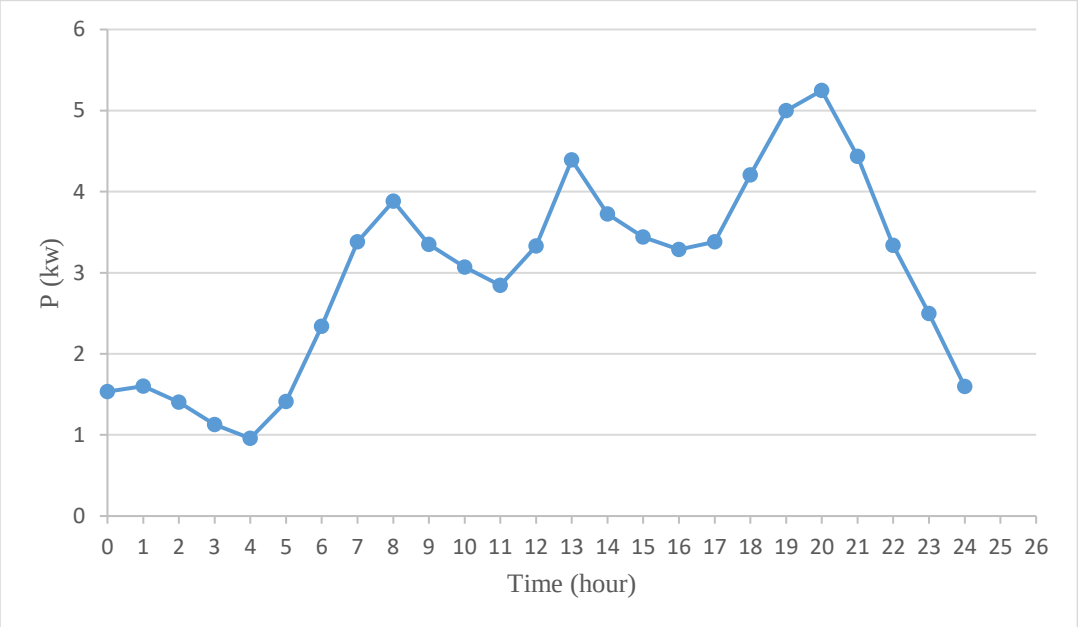


Figure 7. The production power of the PAT 2 in 24 hours

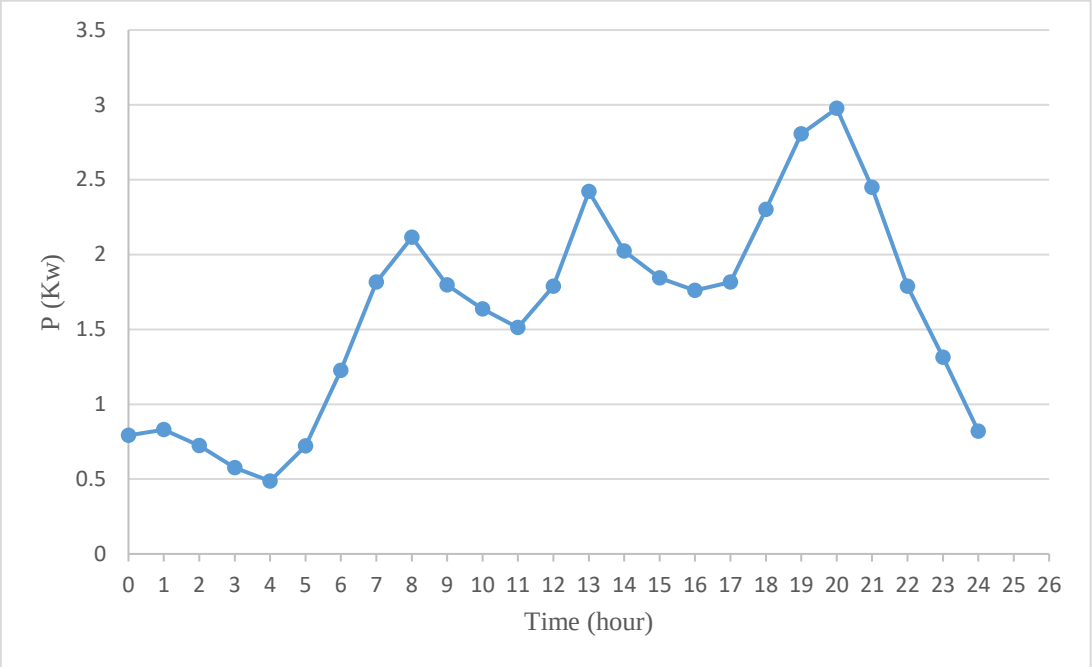


Figure 8. The production power of the PAT 3 in 24 hours

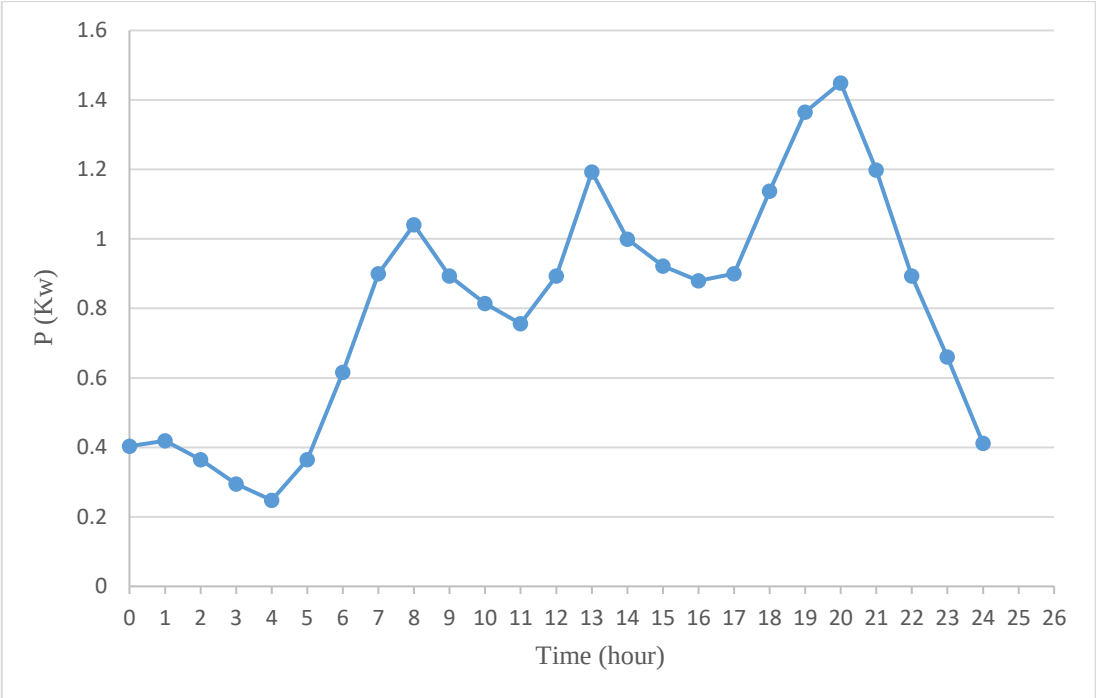


Figure 9. The production power of the PAT 4 in 24 hours

Table 2. The annual recovered energy of each PAT

PAT number	Annually recovered energy (Kwh)
1	87,472
2	78,951
3	70,882
4	35,071

A comparison of each scenario for leakage reduction and producing energy has been presented in table 3.

Table 3. The comparison of each scenario for annual saved water and energy

	Scenarios		
	No control	PRV	PAT
Annual saved water (m^3)	-	462,633.12	569,224.8
Total annually recovered energy (Kwh)	-	-	272,376

As can be seen in Table 3, despite the better control of leakage in scenario 3 than scenario 2, a significant amount of hydropower has been generated in scenario 3. In order to evaluate the economic feasibility of the project, the cost and benefit of the project can be considered. Eventually the economic feasibility demonstrates that pressure management by PATs is an effective method because while reducing leakage, considerable hydropower energy is also produced.

6. conclusions

Pressure management is one of the most efficient and cost-effective ways to reduce leakage in WDNs. Due to the direct relationship between leakage and pressure in WDNs, it is possible to control the amount of leakage in the network with proper pressure management. As a common approach, pressure reduction in water distribution networks is usually done using PRVs, while it can be beneficial that the energy dissipated from head loss is recovered to generate hydropower. In this paper, the feasibility of using PATs in pressure control for the Baharan network located in Sanandaj city in Iran, was investigated. For this purpose, three scenarios were defined to compare and evaluate the effect of PRVs and PATs on NPRI and the reduction in network leakage. At first in scenario 1, the model was evaluated without any PRV, and the pressure in the nodes was examined. Results showed that the pressure in the nodes was very high. In scenario 2, in order to control the additional pressure in the nodes, four PRVs were placed at the entrance of each pressure zone. Finally, in scenario 3, PATs were placed instead of the PRVs. Comparing the results in different scenarios showed that the pressure control by PATs while reducing the amount of leakage more than the PRVs, produces a significant amount of hydropower energy. The network's NPRI in scenario 3 compared to scenario 1 has increased by about 0.41, and the leakage rate has decreased by about 33 percent. By using PATs, the nodal pressures have been significantly reduced, and the average pressure of the network decreased by 58 percent that was within the allowed range. In addition, the amount of hydropower produced by PATs was about 272,376 (KWh/year). According to the results of this study, the use of PATs can be a good alternative in water distribution networks, especially in mountainous regions or areas with high altitude differences.

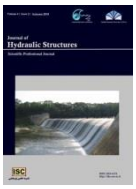
References

1. Corcoran, L., McNabola, A. and Coughlan, P., 2016. Optimization of water distribution networks for combined hydropower energy recovery and leakage reduction. Journal of Water Resources Planning and Management, 142(2), p.04015045.
2. Jones, F.T. and Barkdoll, B.D., 2022. Viability of Pressure-Reducing Valves for Leak Reduction in Water Distribution Systems. Water Conservation Science and Engineering, 7(4), pp.657-670.
3. Binama, M., Su, W.T., Li, X.B., Li, F.C., Wei, X.Z. and An, S., 2017. Investigation on pump as turbine (PAT) technical aspects for micro hydropower schemes: A state-of-the-art review. Renewable and Sustainable Energy Reviews, 79, pp.148-179.
4. Novara, D. and McNabola, A., 2021. Design and year-long performance evaluation of a pump as turbine (Pat) pico-hydropower energy recovery device in a water network. Water, 13(21), p.3014.
5. Lima, G.M., Junior, E.L. and Brentan, B.M., 2017. Selection of pumps as turbines substituting pressure reducing valves. Procedia Engineering, 186, pp.676-683.
6. Fecarotta, O., Aricò, C., Carravetta, A., Martino, R. and Ramos, H.M., 2015. Hydropower potential in water distribution networks: Pressure control by PATs. Water resources management, 29, pp.699-714.
7. Morani, M.C., Carravetta, A., D'Ambrosio, C. and Fecarotta, O., 2021. A new mixed integer non-linear programming model for optimal PAT and PRV location in water distribution networks. Urban Water Journal, 18(6), pp.394-409.
8. Fontana, N., Marini, G. and Creaco, E., 2021. Comparison of PAT installation layouts for energy recovery from water distribution networks. Journal of Water Resources Planning and Management, 147(12), p.04021083.
9. Pillay, E., Kumarasamy, M., Adu, J., Thirumuruganandham, S.P., Paruk, A. and Naidoo, M., 2022. Feasibility analysis of energy recovery using PATs in water distribution networks. Water, 14(7), p.1150.
10. Fernández García, I., Perea, R.G. and Rodríguez Díaz, J.A., 2022. New model for determining optimal PAT locations: maximizing energy recovery in irrigation networks. Journal of Water Resources Planning and Management, 148(11), p.04022054.
11. Stefanizzi, M., Filannino, D., Capurso, T., Camporeale, S.M. and Torresi, M., 2023. Optimal hydraulic energy harvesting strategy for PaT installation in Water Distribution Networks. Applied Energy, 344, p.121246.
12. Kowalska, B., Suchorab, P. and Kowalski, D., 2022. Division of district metered areas (DMAs) in a part of water supply network using WaterGEMS (Bentley) software: a case study. Applied Water Science, 12(7), p.166.
13. EKWULE, O. and UTSEV, J., 2019. Evaluation of a Municipal Water Distribution Network Using waterCAD and waterGEMS. Kastamonu University Journal of Engineering and Sciences, 5(2), pp.147-156.

14. Shang, F., Rossman, L.A. and Uber, J.G., 2023. EPANET-MSX 2.0 user manual. EPA/600/R-22/199. Cincinnati: USEPA.
15. Arandia, E. and Eck, B.J., 2018. An R package for EPANET simulations. Environmental modelling & software, 107, pp.59-63.
16. Dini, M., Mohammadikaleibar, A., Hashemi, S. and Nourani, V., 2022. Stochastic long-term reliability of water distribution networks using Monte Carlo simulation. Urban Water Journal, 19(2), pp.151-160.
17. Muranho, J., Ferreira, A., Sousa, J., Gomes, A. and Marques, A.S., 2014. Pressure-dependent demand and leakage modelling with an EPANET extension–WaterNetGen. Procedia Engineering, 89, pp.632-639.
18. Kaunda, C.S., Kimambo, C.Z. and Nielsen, T.K., 2014. A technical discussion on microhydropower technology and its turbines. Renewable and Sustainable Energy Reviews, 35, pp.445-459.
19. Mirjalili, S. and Mirjalili, S., 2019. Genetic algorithm. Evolutionary Algorithms and Neural Networks: Theory and Applications, pp.43-55.
20. Jafari, R., Khanjani, M.J. and Esmaeilian, H.R., 2015. Pressure management and electric power production using pumps as turbines. Journal-American Water Works Association, 107(7), pp.E351-E363.
21. Do, N.C., Simpson, A.R., Deuerlein, J.W. and Piller, O., 2016. Calibration of water demand multipliers in water distribution systems using genetic algorithms. Journal of water resources planning and management, 142(11), p.04016044.
22. Cimorelli, L., D'Aniello, A. and Cozzolino, L., 2020. Boosting genetic algorithm performance in pump scheduling problems with a novel decision-variable representation. Journal of Water Resources Planning and Management, 146(5), p.04020023.
23. Du, B., Zha, D., Guo, J. and Yu, X., 2023. Optimization of pump scheduling in waterworks considering load balancing using improved genetic algorithm. Journal of Intelligent & Fuzzy Systems, (Preprint), pp.1-19.
24. Świtnicka, K., Suchorab, P. and Kowalska, B., 2017. The optimisation of a water distribution system using Bentley WaterGEMS software. In ITM Web of Conferences (Vol. 15, p. 03009). EDP Sciences.

© 2024 by the authors. Licensee SCU, Ahvaz, Iran. This article is an open access article distributed under the terms and conditions of the Creative Commons Attribution 4.0 International (CC BY 4.0 license) (http://creativecommons.org/licenses/by/4.0/).

Journal of Hydraulic Structures
J. Hydraul. Struct., 2024; 10(1): 13-28
DOI: 10.22055/jhs.2024.45772.1281



OPEN ACCESS

Experimental evaluation of dune formation downstream of pier scour hole with upstream debris accumulation

Ali Mahdian Khalili [1]
Pouria Akbari Dadamahalleh [1]
Mehdi Hamidi[2]

Abstract

Debris upstream of the bridge pier and through the flow variations, changes scour hole and river morphology. Dune forms downstream of the pier as a result of sediment movement in the pier scour phenomenon. The present study investigates the dune characteristics and geometrical parameters in experimental models. Experimental models are categorized into four cases including the pier, pier with buried debris, pier with free debris, and pier with free debris which was protected by bed sill at four various distances from the pier downstream face. It was concluded that debris submergence, densimetric particle Froude number, flow intensity, and bed sill affect dune geometrical parameters such as dune height (h_d), dune crest position (x_d), and dune length (l_d). Results show dune height increases with debris accumulation up to almost 150% and its crest distance from the pier reduces up to approximately 100%. Also, in higher F_d, the dune height and its crest distance reduce with bed sill up to 50%, and in lower F_d, h_d, and x_d increase by up to 80% by using bed sill. Based on these effective parameters, three separate equations were proposed for h_d, x_d, and l_d in pier scour with debris accumulation protected by bed sill.

Keywords: Bed sill, Bridge scour, Debris, Dune, Experimental investigation.

Received: 06 January 2024; Accepted: 13 February 2024

1. Introduction

Debris including broken trees, large pieces of wood, and leaves can be transported in river flow as a result of natural hazards such as landslides and floods. These floated materials can accumulate upstream of the bridge pier and block and change the river flow pattern. This phenomenon increases the shear stress and generates a horseshoe vortex, and a wake vortex upstream and downstream of the pier, respectively. Thus, scour hole depth becomes greater and

[1] Faculty of Civil Engineering, Babol Noshirvani University of Technology, Babol, Mazandaran, Iran.
[2] Faculty of Civil Engineering, Babol Noshirvani University of Technology, Babol, Mazandaran, Iran. Email: hamidi@nit.ac.ir **(Corresponding author)**

CC BY

river morphology varies [1]. The effects of debris accumulation with different shapes were studied on pier scour depth [1-18].

Melville and Dangol (1992) [2] studied the maximum scour depth of the pier (d_s) with various debris blockage shapes resulting in the pier diameter being considered larger than the actual pier diameter. Their suggested equation for the effective pier diameter was corrected by Lagasse et al. [1, 3]. The accumulation of rectangular woody debris upstream of the cylindrical pier increased d_s by up to 30% compared to the accumulating middle of it [4]. Debris with different lengths, thicknesses, shapes, and positions were investigated and it was observed that d_s become larger by increasing the debris thickness, also rectangular debris creates larger ds than triangular, and cylindrical [6]. When the debris approaches the river bed, d_s reduces and the largest value is for the case that debris is exactly below the water elevation [9]. It was concluded that when debris was exactly on the channel bed, it conserved the river bed locally and decreased d_s [6, 9, 11]. The level of debris investigated on pier scour indicated that free debris (upper than the bed level) in all flow depths increases d_s and buried debris (exactly on the bed level) in shallow flow increases ds up to 10% and reduces d_s in partially deep flow [16]. Distances of the pier from the channel wall were studied with debris accumulation and d_s increases when the pier was near the channel wall [12]. Also, the scour hole length increases in cases with debris [12]. At flow with small depth, the location of debris accumulation influences the scour evolution and bed topography but at deep flow, its impact is few [13].

Oliveto and Hager (2014) investigated the dune characteristics generated immediately downstream of local scour piers experimentally [19]. They described dune evolution and its downstream migration by proposing equations as a function of the effective parameters. Pagliara and Carnacina (2010) studied the scour morphology and dune evolution on pier scour with debris accumulation [20]. They suggested a new equation to predict maximum scour depth and longitudinal and transversal lengths.

Many researchers studied scour hole depth and reduced it with some applicable countermeasures such as bed sill, collar, riprap, slot, and submerged vanes [20-35]. Utilizing a buried sill in the channel bed slows the scour rate and reduces d_s in debris accumulation conditions [5]. Slots on the pier reduced scour depth with debris accumulation, and the reduction efficiency in debris cases compared to cases without it did not have constant variations and changes due to different debris shapes [14]. Collar installation on the bridge pier with debris reduced d_s by about 40 percent compared to the case pier only, and also reduction efficiency became 25 percent more in debris accumulation conditions [15]. When riprap is used as a countermeasure, debris does not influence the performance of standard-size riprap [17]. But riprap stone median size is an effective parameter, and with debris accumulation when it was reduced by 25% riprap efficiency was decreased by 10% [17].

Former studies investigated the maximum depth of the pier scour hole in debris cases and suggested different analytical equations to predict it. Dune bed formation is inevitable in the pier scour phenomenon, generated through the deposition of sediment particles from around the pier upstream region of the pier and extending downstream during scour hole evolution and equilibrium times. Although dune evolution is dependent on the geometry of scour holes, a comprehensive study did not apply to investigate dune characteristics, especially in the case of debris blockage. On the other hand, debris increases the scour depth locally, so it is necessary to reduce it by applying some techniques. Since previous studies did not interpret dune formation downstream of the scour hole in local pier scour hole in the case of debris blockage sufficiently and comprehensively, the present study focused on dune formation downstream of the pier scour hole with debris blockage in shapes rectangular in two separate conditions with the sill protected

and without it. As it was reported that debris level is an effective parameter, debris was considered in two different levels including buried (exactly on the bed level) and free (upper than the bed level). Sills were installed at distances of 0D, 1D, 2D, 3D, and 4D downstream of the bridge pier. Finally, three separate equations were suggested based on obtained results for dune height, dune crest position, and dune length.

2. Materials and methods

2.1. Dimensional analysis

Dune height depends on various parameters including sediment parameters and hydraulic parameters. Oliveto and Hager (2014) proposed equation (1) for dune height (h_d) and its distance from pier (x_d) as follows [19]:

$$\frac{h_d}{y}.\frac{x_d}{y} = f(\frac{D}{y}.F_d.\sigma_g.\Delta F_d.\frac{y}{d_{50}}.T) \quad (1)$$

where D is the pier diameter in meter, y is approach flow depth in meters, F_d is densimetric particle Froude number, σ_g is sediment nonuniformity parameter=$(d_{84}/d_{16})^{0.5}$, $\Delta F_d = F_{di}-F_d$ (F_{di} is the inception densimetric Froude number, d_{50} is the median particle size in meter, and T is the dimensionless time= $([(\rho_s-\rho)/\rho]gd_{50})^{0.5}(t/y)$, ρ_s is sediment specific weight in kilogram per cube meter, ρ is water specific weight in kilogram per cube meter, g is gravitational acceleration in meter per square second, and t is time. In the case of debris accumulation with bed sill equation (2) suggested [16]:

$$\frac{h_d}{D}.\frac{x_d}{D}.\frac{l_d}{D} = f\left(\frac{H}{D}.F_d.\frac{u}{u_c}.\frac{L_b}{D}\right) \quad (2)$$

where H is the vertical gap between the debris top surface and sand's initial level in meter, u is the flow velocity depth at the pier upstream in meter per second, u_c is the critical velocity of bed particle in meter per second, and L_b is the bed sill downstream distance from the pier in meter.

2.2. Experimental model

An experimental model was made in a hydraulic laboratory of Noshirvani University of Technology, in Babol, and tests were performed at a sediment flume with length, width, and height of 4, 0.6, and 0.2 meters (Figure 1(a)). For adjusting the flow and tailwater depths, the flume has a tailgate that provides a defined water depth in the channel (Figure 1(b)). To avoid flow disturbance wire mesh plate was located after the upstream tank in the channel inlet and for having developed flow, a 0.5-meter-long rigid apron was installed at the channel beginning (Figure 1(c)) and a cylindrical pier was located 3 meters downstream of the inlet flow which provides a suitable symmetric flow pattern in the channel. A point gauge with an accuracy of 0.1 mm was utilized to measure water and sediment depths (Figure 1(d)).

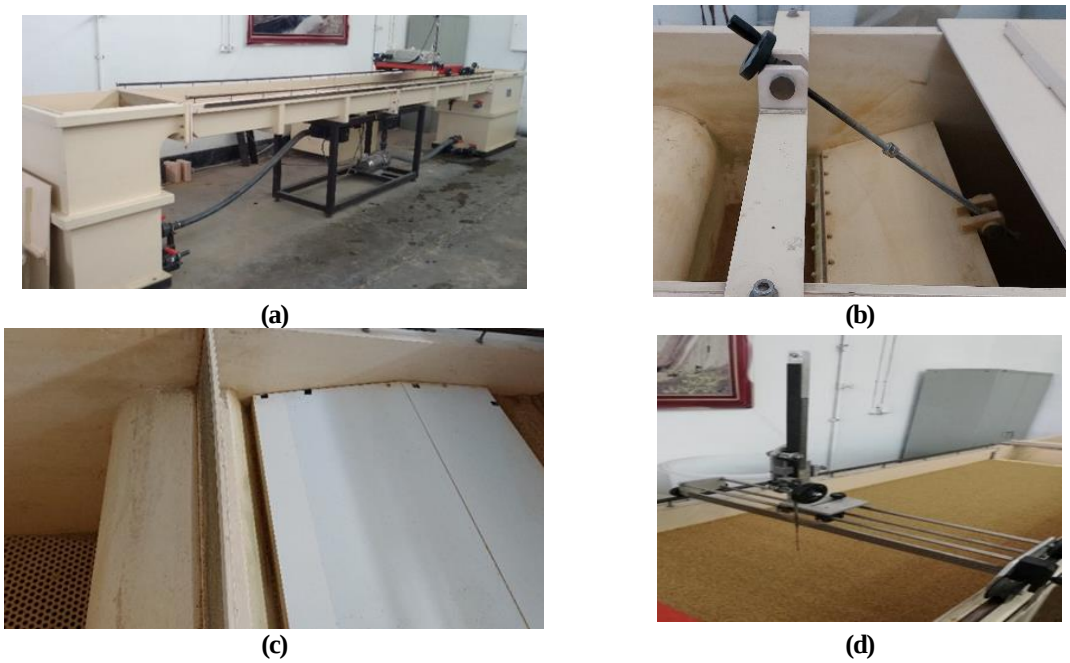


Figure 1. (a) Laboratory flume (b) Tailgate (c) Wire mesh plate and rigid apron (d) Point gauge

To avoid the formation of a ripple, the median particle size (d_{50}) should be smaller than 0.7 mm [36]. When the ratio between channel width to bridge pier diameter (B/D) is more than 6.25, channel walls do not affect scour hole geometry and morphology [36]. If D/d_{50}>20-25, sand size does not influence scour depth [36]. The physical model included bed sediment, a pier, a debris box, and a sill. Tests were applied on sand sediment with parameters according to Figure 2. For sample sediment d_{50}=0.82 mm and σ_g=1.26 (uniform sediment). The pier was made with a steel pipe with a 3 cm diameter welded on an iron plate (B/D=20, D/d_{50}=36.6). When Wooden debris is gathered upstream of the bridge pier, a more possible shape form is a rectangle, and rectangular wooden debris creates maximum scour depth around a pier [9-10]. Debris was modeled as a rectangular mesh wire box 0.05 m high, 0.10 m long, and 0.12 m wide poured with wood pieces with diameters of 0.1 to 0.5 cm and fixed on the pier by a screw. Sill was modeled with a PVC plate that was 0.10 m high, 3 mm thick, and 0.60 m wide located at five varied positions with distances 0D, 1D, 2D, 3D, and 4D, downstream of the pier.

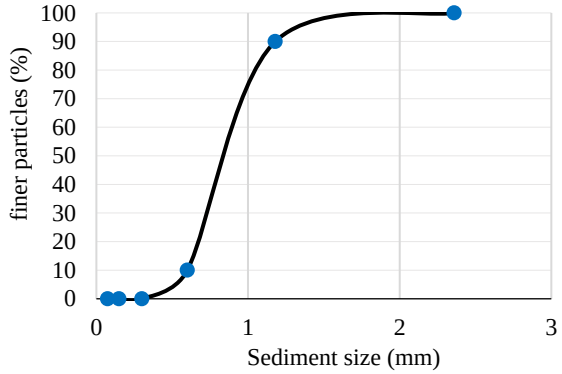


Figure 2. Sand sediment granulation

Table 1 indicates the experimental setup and hydraulic parameters of the model considered in four cases (A, B, C, and D). Case A included a pier, Case B is a pier with buried debris (exactly on the bed level), Case C included a pier with free debris (with a distance of D upper than the bed level), and Case D which bed sill is added to case C with downstream distance of 0D, 1D, 2D, 3D, and 4D. In Table 1, y is the approach flow depth in meters, H is the vertical gap between the debris top surface and the sand's initial level in meters, u is the flow velocity depth at the pier upstream in meters per second, u_c is the critical velocity of bed particle in meter per second, F_d is particle densimetric Froude number, D is the pier diameter in meter, and L_b is the bed sill downstream distance from the pier in meter.

Table 1. Experimental Setup

Case	Model	Test	y (m)	H (m)	y/H	u/uc	F_d	y/D	L_b/D
A	Pier	A1	0.03	NA*	NA	0.838	3.688	1.000	NA
		A2	0.04	NA	NA	0.599	2.398	1.333	NA
		A3	0.05	NA	NA	0.462	1.719	1.667	NA
		A4	0.06	NA	NA	0.370	1.289	2.000	NA
		A5	0.07	NA	NA	0.311	1.032	2.333	NA
		A6	0.08	NA	NA	0.265	0.842	2.667	NA
		A7	0.09	NA	NA	0.230	0.705	3.000	NA
B	Pier + Buried Debris	B1	0.03	0.05	0.600	0.838	3.688	1.000	NA
		B2	0.04	0.05	0.800	0.599	2.398	1.333	NA
		B3	0.05	0.05	1.000	0.462	1.719	1.667	NA
		B4	0.06	0.05	1.200	0.370	1.289	2.000	NA
		B5	0.07	0.05	1.400	0.311	1.032	2.333	NA
		B6	0.08	0.05	1.600	0.265	0.842	2.667	NA
		B7	0.09	0.05	1.800	0.230	0.705	3.000	NA
C	Pier + Free Debris	C1	0.04	0.08	0.500	0.599	2.398	1.333	NA
		C2	0.05	0.08	0.625	0.462	1.719	1.667	NA
		C3	0.06	0.08	0.750	0.370	1.289	2.000	NA
		C4	0.07	0.08	0.875	0.311	1.032	2.333	NA
		C5	0.08	0.08	1.000	0.265	0.842	2.667	NA
		C6	0.09	0.08	1.125	0.230	0.705	3.000	NA
D	Pier + Free Debris + Sill	D1	0.04	0.08	0.500	0.599	2.398	1.333	0
		D2	0.06	0.08	0.750	0.370	1.289	2.000	0
		D3	0.08	0.08	1.000	0.265	0.842	2.667	0
		D4	0.04	0.08	0.500	0.599	2.398	1.333	1
		D5	0.06	0.08	0.750	0.370	1.289	2.000	1
		D6	0.08	0.08	1.000	0.265	0.842	2.667	1
		D7	0.04	0.08	0.500	0.599	2.398	1.333	2
		D8	0.06	0.08	0.750	0.370	1.289	2.000	2
		D9	0.08	0.08	1.000	0.265	0.842	2.667	2
		D10	0.04	0.08	0.500	0.599	2.398	1.333	3
		D11	0.06	0.08	0.750	0.370	1.289	2.000	3
		D12	0.08	0.08	1.000	0.265	0.842	2.667	3
		D13	0.04	0.08	0.500	0.599	2.398	1.333	4
		D14	0.06	0.08	0.750	0.370	1.289	2.000	4
		D15	0.08	0.08	1.000	0.265	0.842	2.667	4

* Not Available

2.3. Equilibrium scour time

Three tests (A2, B2, and C1) were performed over 8 hours to achieve scour equilibrium time. Figure 3 shows that after 5 hours, scour hole depth remains almost constant for up to 8 hours, thus this time can be considered an equilibrium scour time.

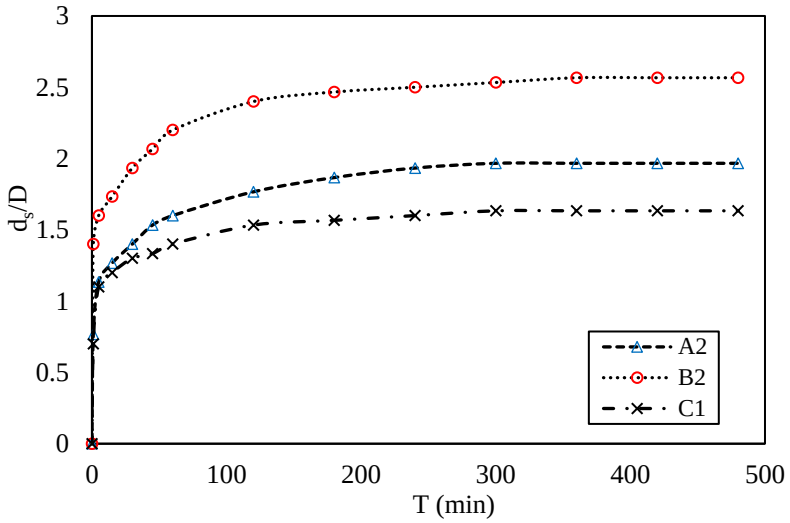
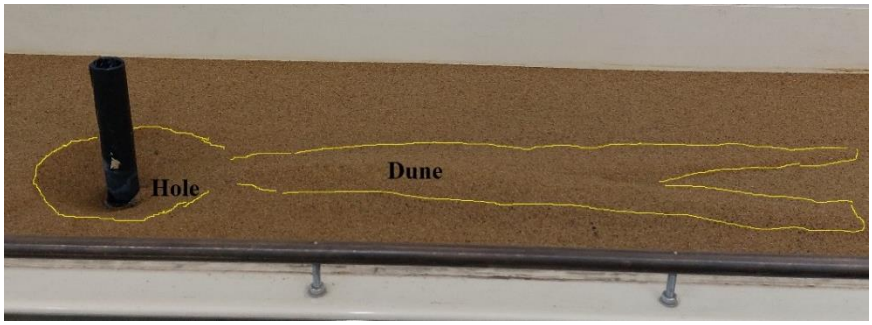


Figure 3. Time evolution of scour hole depth

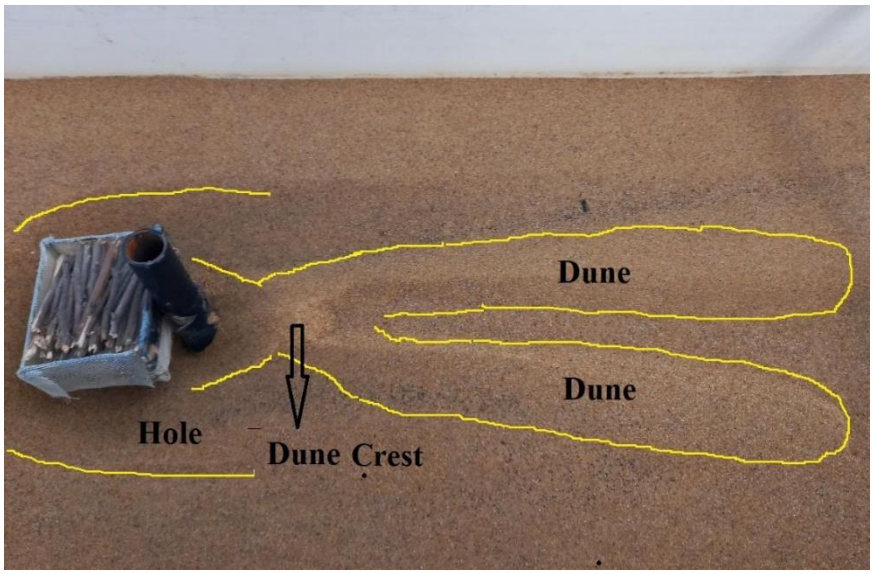
3. Results and discussion

3.1. Experimental results

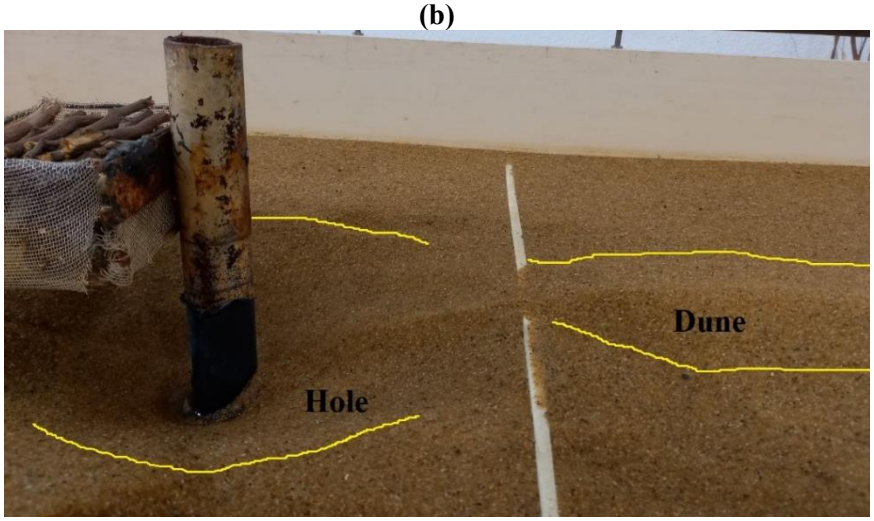
In all tests dunes formed downstream of the scour hole of the pier. It occurred through the sand removal around the upstream region of the pier as a result of vortexes and deposition downstream during the scour process. Figure 4 indicates dune formation following a scour hole in the same hydraulic conditions (F_d=2.398) in different cases (test A2, test B2, and Test D10). As can be observed in all conditions including pier (case A), pier with debris (case B and C), and pier with debris protected by sill (case D) dune geometry changes. The dune structure has two wings that develop until reaches the initial bed level, also it has one crest area where dune height is the maximum value.



(a)



(b)



(c)

Figure 4. Dune Formation downstream of scour hole (a) Test A2 (b) Test B2 (c) Test D10

Table 2 presents the results of each test for dune characteristics. h_d is the maximum height of the dune crest in meters (dune height). x_d is the longitudinal distance between the location of the maximum height of the dune crest and the pier downstream face (dune crest position) in meters. l_d is the longitudinal distance between the pier's downstream face and the location where the dune reaches the bed's initial level (dune length) in meters.

Table 2. Dune characteristics

Case	Model	Test	y/H	u/uc	F_d	L_b/D	h_d/D	x_d/D	l_d/D
A	Pier	A1	NA*	0.838	3.688	NA	0.433	15.833	NM**
		A2	NA	0.599	2.398	NA	0.167	5.833	NM
		A3	NA	0.462	1.719	NA	0.300	5.833	NM
		A4	NA	0.370	1.289	NA	0.567	4.167	NM
		A5	NA	0.311	1.032	NA	0.600	3.500	NM
		A6	NA	0.265	0.842	NA	0.333	3.000	NM
		A7	NA	0.230	0.705	NA	0.033	1.167	NM
B	Pier + Buried Debris	B1	0.600	0.838	3.688	NA	0.467	4.167	NM
		B2	0.800	0.599	2.398	NA	0.800	5.833	NM
		B3	1.000	0.462	1.719	NA	0.767	3.500	NM
		B4	1.200	0.370	1.289	NA	0.300	1.500	NM
		B5	1.400	0.311	1.032	NA	0.467	0.500	NM
		B6	1.600	0.265	0.842	NA	0.433	0.500	NM
		B7	1.800	0.230	0.705	NA	0.033	0.033	NM
C	Pier + Free Debris	C1	0.500	0.599	2.398	NA	0.067	5.833	NM
		C2	0.625	0.462	1.719	NA	0.767	9.167	NM
		C3	0.750	0.370	1.289	NA	1.167	4.500	NM
		C4	0.875	0.311	1.032	NA	0.667	2.833	NM
		C5	1.000	0.265	0.842	NA	0.333	1.500	NM
		C6	1.125	0.230	0.705	NA	0.233	2.833	NM
D	Pier + Free Debris + Sill	D1	0.500	0.599	2.398	0	NM	NM	NM
		D2	0.750	0.370	1.289	0	0.367	3.000	4.333
		D3	1.000	0.265	0.842	0	0.333	0.667	5.000
		D4	0.500	0.599	2.398	1	0.700	11.000	25.000
		D5	0.750	0.370	1.289	1	0.967	3.333	4.000
		D6	1.000	0.265	0.842	1	0.600	2.000	5.000
		D7	0.500	0.599	2.398	2	0.767	9.000	20.000
		D8	0.750	0.370	1.289	2	0.800	2.500	3.333
		D9	1.000	0.265	0.842	2	0.400	1.667	5.000
		D10	0.500	0.599	2.398	3	0.967	10.333	26.667
		D11	0.750	0.370	1.289	3	0.833	2.333	4.000
		D12	1.000	0.265	0.842	3	0.433	1.000	5.333
		D13	0.500	0.599	2.398	4	0.800	9.667	30.000
		D14	0.750	0.370	1.289	4	0.600	2.000	4.667
		D15	1.000	0.265	0.842	4	0.400	2.667	5.000

* Not Available

** Not Measured

3.2. Effect of debris on dune characteristics

As can be observed from Table 2, debris submergence, densimetric particle Froude number, flow intensity, and bed sill position can affect dune geometrical parameters. Figures 5 and 6 present debris submergence (y/H) and densimetric particle Froude number on dune height and its position, respectively. It concluded that the variations of dune height and its position did not have a constant relation with debris submergence and densimetric particle Froude number, at first, they increased and then reduced. In cases without debris, x_d/D reduced with increasing F_d, in which means the dune crest is closer to the pier downstream.

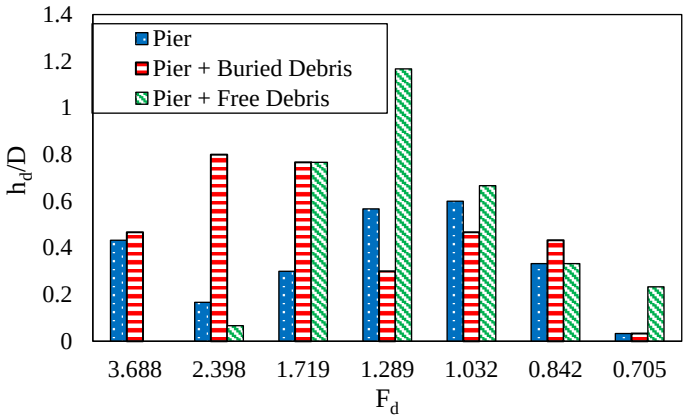


Figure 5. Effect of debris submergence and densimetric particle Froude number on dune height

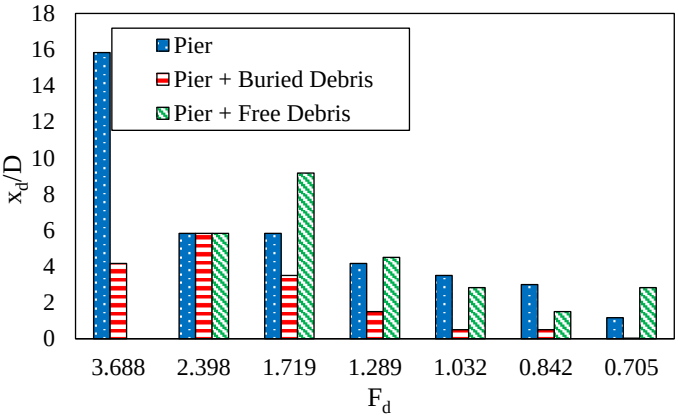


Figure 6. Effect of debris submergence and densimetric particle Froude number on dune position

Figure 7 presents the percentage variations of dune parameters in cases with debris accumulation compared with the cases without it in the same hydraulic parameters. It can be concluded that dune height increases in both buried and free debris and in all hydraulic conditions buried debris reduces x_d which means the dune crest is located closer to the pier.

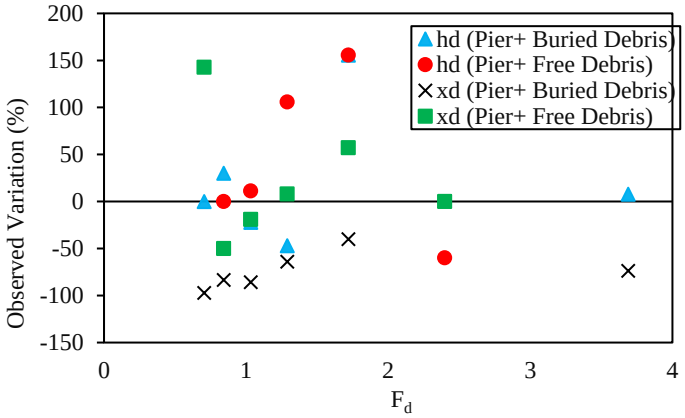


Figure 7. Variations of dune characteristics with debris accumulation compared to cases without it

3.3. Effect of bed sill on dune characteristics

Figures 8, 9, and 10 show the influence of bed sill position with varied densimetric particle Froude numbers on dune height, its position, and dune height respectively. It concluded that the variations of dune height, pick position, and dune length did not have a linear relation with bed sill gap with pier downstream pier and densimetric particle Froude numbers.

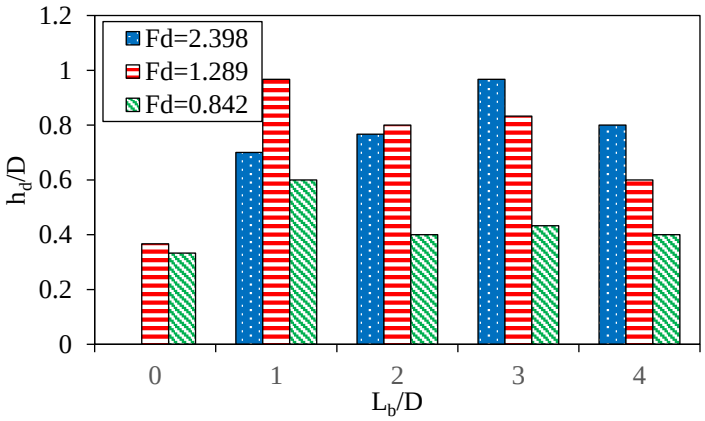


Figure 8. Effect of bed sill position and densimetric particle Froude number on dune height

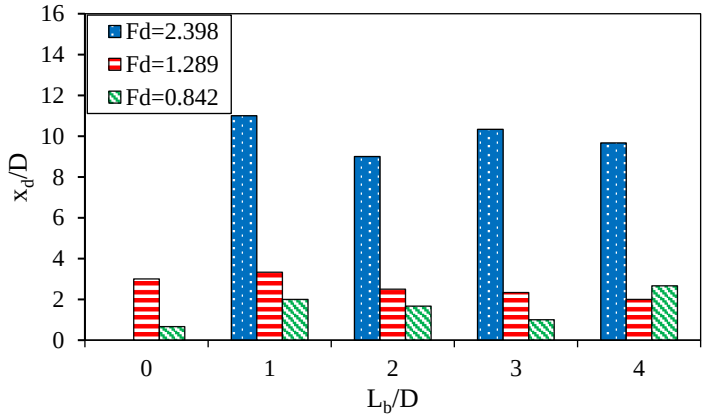


Figure 9. Effect of bed sill position and densimetric particle Froude number on dune position

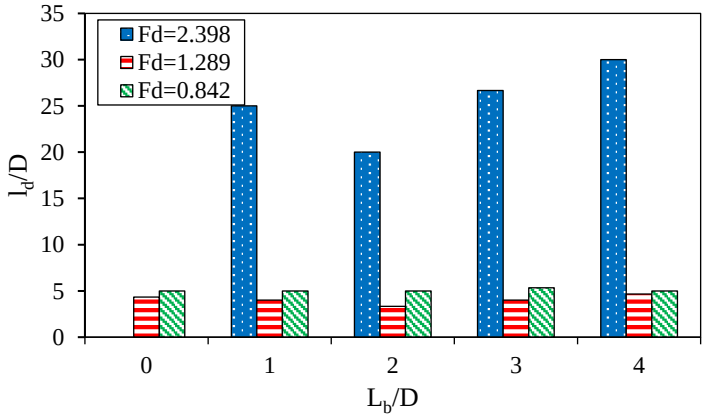


Figure 10. Effect of bed sill position and densimetric particle Froude number on dune length

Figure 11 illustrates the variations of dune parameters when a bed sill is used with free debris in comparison with cases without utilizing bed sill protection. It is observed that hydraulic condition and densimetric particle Froude number affect the influence of bed sill. In higher F_d, the dune height and its crest distance reduce with bed sill but in lower F_d, h_d, and x_d decrease by using bed sill.

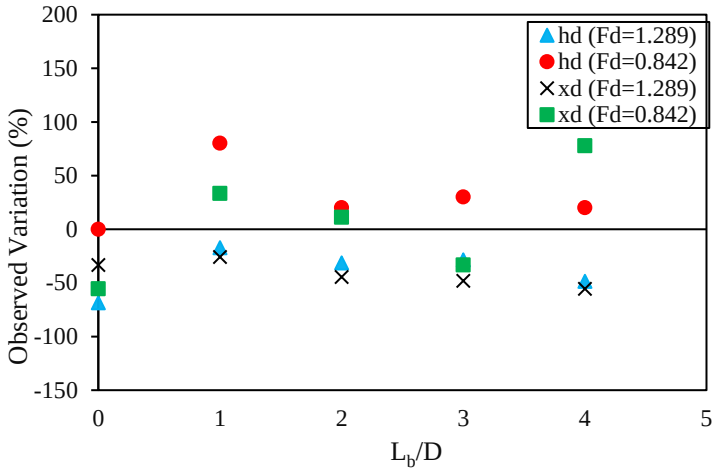


Figure 11. Variations of dune characteristics in debris accumulation with bed sill protection compared to case without sill

3.4. Comparison of obtained dune height with previous results

The obtained results of dimensionless dune height to approach flow depth (h_d/y) were compared to Oliveto and Hager (2014) in Figure 12. This result is for pier scour without debris and bed sill which presents good compatibility with the computed RMSE=0.0421.

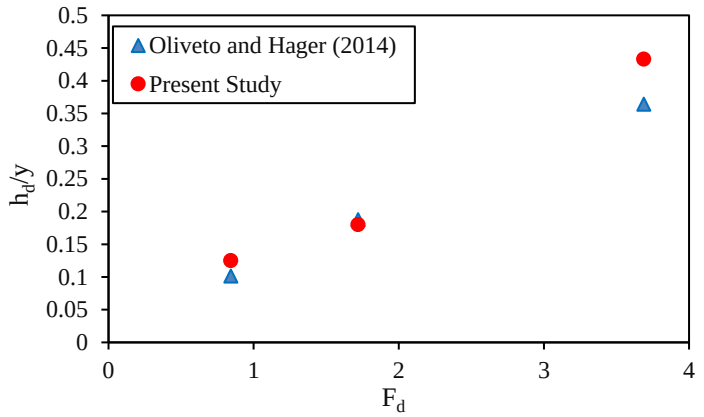


Figure 12. Comparison of obtained dune height in the case without debris and bed sill to the previous study

3.5. Prediction equations for dune characteristics

Based on effective parameters, prediction equations can be proposed by nonlinear regression to analyze extracted data and predict the dune geometry characteristics [37]. Equations (3), (4),

and (5) suggested dune maximum height, dune crest position, and dune maximum length, respectively. These equations were extracted from the Case D model.

$$\frac{h_d}{D} = 1{,}123\left(\frac{y}{H}\right)^{-0{,}132}(F_d)^{0{,}127}\left(\frac{u}{u_c}\right)^{0{,}532}\left(\frac{L_b}{D}\right)^{-0{,}24} \quad (3)$$

$$\frac{x_d}{D} = 14{,}718\left(\frac{y}{H}\right)^{-0{,}147}(F_d)^{0{,}564}\left(\frac{u}{u_c}\right)^{1{,}755}\left(\frac{L_b}{D}\right)^{-0{,}098} \quad (4)$$

$$\frac{l_d}{D} = 2{,}115\left(\frac{y}{H}\right)^{-1{,}307}(F_d)^{1{,}716}\left(\frac{u}{u_c}\right)^{0{,}412}\left(\frac{L_b}{D}\right)^{-0{,}314} \quad (5)$$

Table 3 proposed the parameter ranges and correlation ratio (R^2) for the suggested equations and RMSE as equation (6). In this equation x_p is the predicted values, x_o is the observed values, and n is the data number [38-39].

$$RMSE = \sqrt{\frac{\sum_1^n (x_p - x_o)^2}{n}} \quad (6)$$

Table 3. Effective parameters range for proposed equations

Equation	Parameter	y/H	F_d	u/u_c	L_b/D	RMSE	R^2
1	h_d	0.5-1	0.842-2.398	0.265-0.599	1-4	0.175	0.629
2	x_d	0.5-1	0.842-2.398	0.265-0.599	1-4	0.688	0.984
3	l_d	0.5-1	0.842-2.398	0.265-0.599	1-4	3.052	0.969

Figures 13, 14, and 15 present predictions of dune maximum height, dune crest position, and dune maximum height according to Equations (3), (4), and (5), respectively.

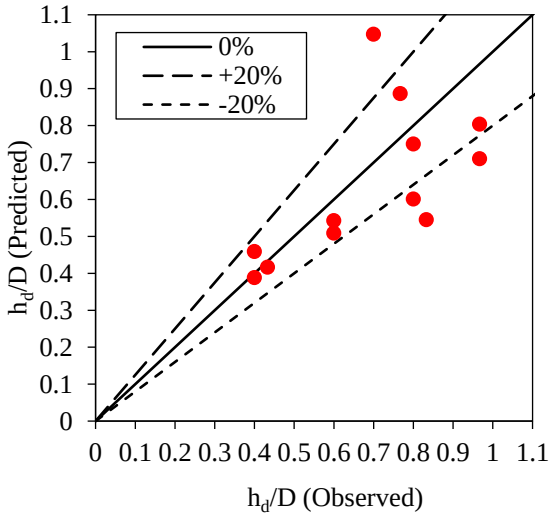


Figure 13. Prediction of dune maximum height

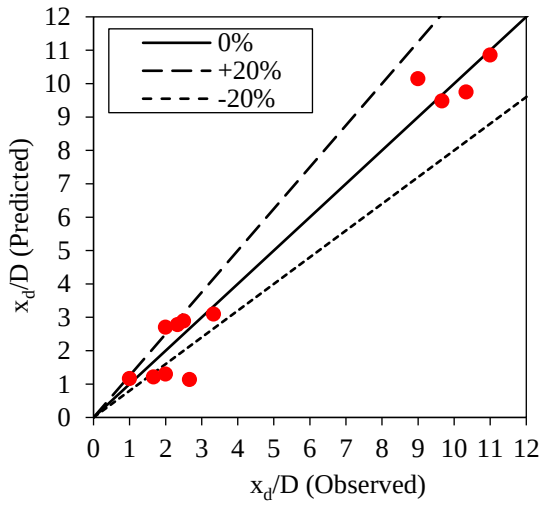


Figure 14. Prediction of dune crest position

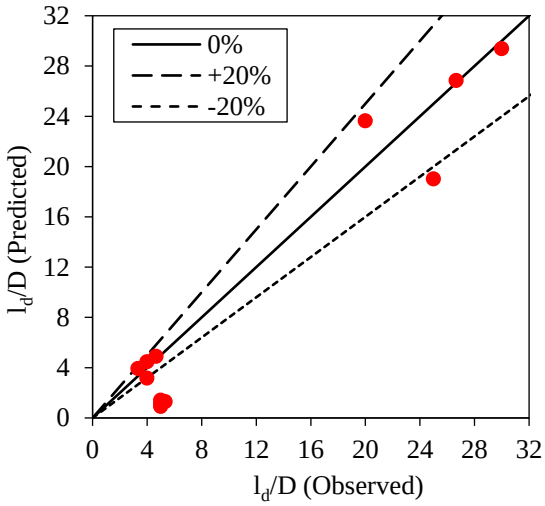


Figure 15. Prediction of dune maximum length

4. Conclusion

The present paper studied the laboratory model for the investigation of scour around the bridge pier with a rectangular upstream block with and without protection of sill. Four cases consist of A (pier), B (pier + buried debris), C (pier + free debris), and D (pier + free debris + bed sill). Dune geometrical parameters such as dune maximum height (h_d), dune crest position (x_d), and dune maximum length (l_d) were measured and compared in each test. It was observed that debris submergence (y/H), densimetric Froude number (F_d), flow intensity (u/u_c), and bed sill position (L_b/D) affect dune geometrical parameters. Results indicated that changes in h_d and x_d did not have a fixed relation with y/H and F_d, at first, they increased and then reduced. When debris did not appear x_d reduced with increasing F_d, it means the dune crest approached the pier downstream. Based on experimental data, equations were achieved on nonlinear regression for debris accumulation with bed sill protected for h_d, x_d, and l_d with a correlation ratio (R^2) equal to

0.629, 0.984, and 0.969, respectively. Used effective parameters in prediction equations have limited ranges which were presented in the results.

References

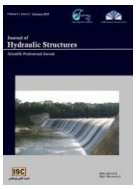
1. Lagasse PF, Clopper PE, Zevenbergen LW, (2010). Effects of debris on bridge pier scour. NCHRP Report 653, Transportation Research Board, National Academies of Science, Washington, D.C.
2. Melville BW, Dongol DM, (1992). Bridge pier scour with debris accumulation. Journal of Hydraulic Engineering, 118, pp: 1306–1310. https://doi.org/10.1061/(ASCE)0733-9429(1992)118:9(1306).
3. Lagasse PF, Zevenbergen LW, Clopper PE, (2010). Impacts of debris on bridge pier scour. Scour and Erosion. American Society of Civil Engineers, Reston, VA, pp: 854–863.
4. Pagliara S, Carnacina I, (2010). Temporal scour evolution at bridge piers: effect of wood debris roughness and porosity. Journal of Hydraulic Research, 48(1), pp: 3-13. https://doi.org/10.1080/00221680903568592.
5. Pagliara S, Carnacina I, Cigni F, (2010). Sills and gabions as countermeasures at bridge pier in presence of debris accumulations. Journal of Hydraulic Research, 48(6), pp: 764-774. https://doi.org/10.1080/00221686.2010.528184.
6. Pagliara S, Carnacina I, (2011). Influence of wood debris accumulation on bridge pier scour. Journal of Hydraulic Engineering, 137, pp: 254–261. https://doi.org/10.1061/(ASCE)HY.1943-7900.000028.
7. Pagliara S, Carnacina I, (2011). Influence of large woody debris on sediment scour at bridge pier. International Journal of Sediment Research, 26, pp: 121-136. https://doi.org/10.1016/S1001-6279(11)60081-4.
8. Park JH, Sok C, Park CK, Do KY, (2016). A study on the effects of debris accumulation at sacrificial piles on bridge pier scour: I. Experimental Results. KSCE Journal of Civil Engineering, 20, pp: 1546–1551. https://doi.org/10.1007/s12205-015-0207-5.
9. Rahimi E, Qaderi K, Rahimpour M, Ahmadi, MM, (2018). Effect of debris on piers group scour: an experimental study. KSCE Journal of Civil Engineering, 22, pp: 1496–1505. https://doi.org/10.1007/s12205-017-2002-y.
10. Abousaeidi Z, Ghaderi K, Rahimpour M, Ahmadi MM, (2018). Experimental investigation of the effect of debris accumulation on the local scour at bridge pier and abutment. Journal of Water and Soil Conservation, 25(2), pp: 267-282. 10.22069/JWSC.2018.12472.2714.
11. Ebrahimi M, Kripakaran P, Prodanović DM, et al., (2018). Experimental study on scour at a sharp-nose bridge pier with debris blockage. Journal of Hydraulic Engineering, 144:04018071. https://doi.org/10.1061/(ASCE)HY.1943-7900.0001516.
12. Pagliara S, Palermo M, (2020). Effects of bridge pier location and debris accumulation on equilibrium morphology. World Environmental and Water Resources Congress.
13. Palermo M, Pagliara S, Roy D, (2021). Effect of debris accumulation on scour evolution at bridge pier in bank proximity. Journal of Hydrology and Hydromechanics, 61, pp: 1-11. https://doi.org/10.2478/johh-2020-0041.

14. Hamidifar H, Mohammad Ali Nezhadian D, Carnacina I, (2022). Experimental study of debris-induced scour around a slotted bridge pier. Acta Geophysica, 70, pp: 2325–2339. https://doi.org/10.1007/s11600-021-00722-2.
15. Hamidifar H, Shahabi-Haghighi SMB, Chiew YM, (2022). Collar performance in bridge pier scour with debris accumulation. International Journal of Sediment Research, 37, pp: 328-334. https://doi.org/10.1016/j.ijsrc.2021.10.002.
16. Akbari Dadamahalleh P, Hamidi M, Mahdian Khalili A, (2022). Experimental Prediction of the Bed Profile with the Full-submerged and Semi-submerged Debris Accumulation Upstream of the Cylindrical Bridge Pier. Journal of Water and Soil Conservation, 29(4), pp: 95-114. 10.22069/JWSC.2023.20642.3582.
17. Zanganeh-Inaloo F, Hamidifar H, Oliveto G, (2023). Local scour around riprap-protected bridge piers with debris accumulation. Iran. J. Sci. Technol. Trans. Civ. Eng., 47(4), pp: 2393-2408. https://doi.org/10.1007/s40996-023-01034-9.
18. Mahdian Khalili A, Hamidi M, Akbari Dadamahalleh P, (2023). Scour Morphology around the Bridge Pier with Upstream Rectangular Debris. 22nd Iranian Conference on Hydraulics, 8-9 November 2023, University of Maragheh.
19. Oliveto G, Hager WH, (2014). Morphological evolution of dune-like bed forms generated by bridge scour. Journal of Hydraulic Engineering, 140(5), 06014009. https://doi.org/10.1061/(ASCE)HY.1943-7900.0000853.
20. Pagliara S, Carnacina I, (2010). Scour and dune morphology in presence of large wood debris accumulation at bridge pier. In River Flow (Vol. 2, pp. 1223-1230).
21. Chiew YM, (1992). Scour protection at bridge piers. Journal of Hydraulic Engineering, 118, pp: 1260–1269. https://doi.org/10.1061/(ASCE)0733-9429(1992)118:9(1260).
22. Zarrati AR, Chamani MR, Shafaie A, Latifi M, (2010). Scour countermeasures for cylindrical piers using riprap and combination of collar and riprap. International Journal of Sediment Research, 25, pp: 313-322. https://doi.org/10.1016/S1001-6279(10)60048-0.
23. Grimaldi C, Gaudio R, Calomino F, Cardoso AH, (2009). Control of scour at bridge piers by a downstream bed sill. Journal of Hydraulic Engineering, 135, pp: 13–21. https://doi.org/10.1061/(ASCE)0733-9429(2009)135:1(13).
24. Grimaldi C, Gaudio R, Calomino F, Cardoso, AH, (2009). Countermeasures against local scouring at bridge piers: slot and combined system of slot and bed sill. Journal of Hydraulic Engineering, 135, pp: 425–431. https://doi.org/10.1061/(ASCE)HY.1943-7900.0000035.
25. Tafarojnoruz A, Gaudio R, Calomino F, (2012). Bridge pier scour mitigation under steady and unsteady flow conditions. Acta Geophysica, 60, pp: 1076-1097. https://doi.org/10.2478/s11600-012-0040-x.
26. Khaple S, Hanmaiahgari PR, Gaudio R, Dey S, (2017). Splitter plate as a flow-altering pier scour countermeasure. Acta Geophysica, 65, pp: 957–975. https://doi.org/10.1007/s11600-017-0084-z.
27. Pandey M, Azamathulla HM, Chaudhuri S, Pu JH, Pourshahbaz H, (2020). Reduction of time-dependent scour around piers using collars. Ocean Engineering, 213, 107692. https://doi.org/10.1016/j.oceaneng.2020.107692.

28. Raeisi N, Ghomeshi M, (2021). A laboratory study of the effect of asymmetric-lattice collar shape and placement on scour depth and flow pattern around the bridge pier. Water Supply 22, pp: 734-748. https://doi.org/10.2166/ws.2021.239.
29. Saad NY, Fattouh EM, Mokhtar M, (2021). Effect of L-shaped slots on scour around a bridge abutment. Water Practice & Technology, 16(3), pp: 935-945. https://doi.org/10.2166/wpt.2021.037.
30. Koohsari A, Hamidi M, (2021). Experimental study of the effect of mining materials downstream of bridge pier on scour profile with optimizing distance approach. Journal of Water and Soil Conservations, 28(3), pp: 1-26. 10.22069/JWSC.2022.19400.3490.
31. Ebrahimi T, Hamidi M, Rahmani Firoozjaiee A, Khavasi E, (2021). Numerical investigation of scour around a cylindrical pier in laboratory scale using Euler-Lagrange approach. Amirkabir Journal of Mechanical Engineering, 53(1 (Special Issue)), pp: 411-426. 10.22060/MEJ.2019.16679.6418.
32. Sadeqlu M, Hamidi M, (2022). Numerical investigation of the cylindrical bridge pier scour reduction by installing a group of two submerged vanes. Irrigation and Drainage Structures Engineering Research, 22(85), pp: 91-114. https://doi.org/10.22092/idser.2022.357739.1502.
33. Valela, C, Rennie CD, Nistor I, (2022). Improved bridge pier collar for reducing scour. International Journal of Sediment Research, 37(1), pp: 37-46. https://doi.org/10.1016/j.ijsrc.2021.04.004.
34. Khalili AM, Hamidi M, Dadamahalleh PA, (2023). Introducing Countermeasures for Reducing Bed Scour of Mountainous Rivers, 1st International Conference on Sustainable Mountain, 11&12 December 2023, University of Mohaghegh Ardabili.
35. Khalili AM, Hamidi M, Dadamahalleh PA, (2023). Reviewing Ice Covering Effect on Bridge Pier Scour Morphology at Cold Climate, 1st International Conference on Sustainable Mountain, 11&12 December 2023, University of Mohaghegh Ardabili.
36. Raudkivi AJ, Ettema R, (1983). Clear water scour at cylindrical piers. Journal of Hydraulic Engineering, 109(3), 338-350. https://doi.org/10.1061/(ASCE)0733-9429(1983)109:3(338).
37. Mahdian Khalili A, Hamidi M, (2023). Time evolution effect on the scour characteristics downstream of the sluice gate with the submerged hydraulic jump in a laboratory model. Journal of Hydraulic Structures 9(2), pp: 32-47. 10.22055/JHS.2023.43499.1249.
38. Hamidi M, Mohammadhoseyni F, (2020). Numerical Investigation of the Effect of Stilling Basin Length on Flow Energy Dissipation (Case Study of the Chaili Dam Spillway). Irrigation and Water Engineering, 11(1), pp: 66-86. 10.22125/IWE.2020.114954.
39. Biabani S, Hamidi M, Navayi Neya B, (2019). Numerical simulation of the chute convergence effects on forming the transverse wave in flood evacuation systems. Journal of Hydraulics, 14(3), pp: 67-84. 10.30482/JHYD.2019.174636.1373.

© 2024 by the authors. Licensee SCU, Ahvaz, Iran. This article is an open access article distributed under the terms and conditions of the Creative Commons Attribution 4.0 International (CC BY 4.0 license) (http://creativecommons.org/licenses/by/4.0/).

Journal of Hydraulic Structures
J. Hydraul. Struct., 2024;10(1):29-45
DOI: 10.22055/jhs.2024.46145.1288



OPEN ACCESS

Investigating the settlement of the stone boulders breakwater located on the marine soft fine-grained soil

Amin Falamaki [*1]
Amir Hossein Shafiee [2]
Jamal al-Din Iranmahboob [1]
Farzad Arjmand [1]

Abstract

Stone boulders breakwaters are the most widespread and widely used type of breakwaters. if the foundations of these structures do not have sufficient bearing capacity, large settlements will await the structure. Since the construction of these projects is expensive, and the supply of suitable stone resources are essential for the construction of these projects, a relatively good prediction of the stone materials volume used in the project is important. Therefore, a research project was carried out at Siyadi Port breakwater, (Iran) utilizing geotechnical data and construction observations. The objective was to create a computer model to understand the response of the clay bed to the weight of the rocks. This analysis was done by Lagrangian equations and using FLAC software and led to the selection of characteristic of soil parameters that simulated the subsidence of materials on an elasto-plastic bed. Soil resistance parameters that could not be determined through standard tests were derived through a process of back analysis. The study also investigated the effects of the thickness of the loose layer, variations in sea water levels, and the use of geotextile in the project. A large rise in settling is anticipated as the muddy soil's depth increases. Results also confirms the effectiveness of using geotextiles for settlement management. Moreover, updated characteristics of soil from the previous step in order to comprehend the construction of an entire breakwater section on muddy soil seems crucial. With this method, long-term settlements and the stability of the breakwater section may be reliably predicted.

Keywords: Settlement; Breakwater; Stone Boulders Breakwater; Soft Soil.

Received: 14 February 2024; Accepted: 30 March 2024

[*] Corresponding Author: a_falamaki@pnu.ac.ir
[1] Department of Civil Engineering, Payame Noor University, P.O. Box 19395-3697, Tehran, Iran.
[2] Department of Civil Engineering, Faculty of Civil Engineering and Architecture, Shahid Chamran University of Ahvaz, Ahvaz, Iran.

1. Introduction

Marine constructions like breakwaters and coastal walls are crucial human-made structures, particularly in areas with extensive soft and unconsolidated soils along coastlines [1]. An important issue in breakwaters design is the stability [2]. Many researchers have studied behavior of breakwaters like stability and erosion using numerical analysis or experimental studies in laboratory or field [3-10]. The use of stone materials on soft land leads to significant settlements due to the absence of a solid foundation [11]. The soil's shear resistance and its ability to support structures, as well as its settlement capacity, impact the quantity of stones required for breakwaters. This can lead to increased costs, material depletion, and environmental damage. Ghaderi and Rahbani [12] believed that the accretion problem is due to the poor design of the breakwaters' layout.

This matter relates to value engineering, so if suitable geotechnical conditions are not present in non-strategic projects, it may be necessary to consider relocating ports or exploring alternative options. Therefore, it is important to comprehend the response of fine-grained bed materials, typically made up of river or sea sediments, to the loading from the construction of breakwaters. It is crucial to accurately determine the behavior of the soil against the predicted loading of the rock mass and implement appropriate solutions. The presence of rivers and channels that flow into the sea is the primary factor in the formation of fine-grained sediments along the coasts and the seabed adjacent to the coast. Mobarrez et al. [11] conducted an experiment to study the settlement of a breakwater situated on silty soil. They created a simulated sample containing silt with a moisture level exceeding the liquid limit and applied various sizes of aggregates to it. The findings revealed that smaller aggregates resulted in less subsidence, and using smaller aggregates in a thicker layer reduced the overall settlement of the aggregates. Essentially, the infiltration of aggregate material into the soil foundation is directly influenced by the diameter and thickness of the aggregates. In this study, the researchers measured the settlement of soil samples with varying moisture levels and flow limits. The findings indicated that settlement is influenced by soil moisture, with higher levels of moisture leading to greater settlement compared to liquid limit. Nagaraj et al. [13] explained as the liquid limit increases, the shear resistance decreases, and the soil moisture content also plays a role in the penetration of stone materials. According to a study by Fan [14], material subsidence increases as soil moisture reaches three times the liquid limit, leading to an increase in settlement. Beyond that point, the settlement remains constant. In addition, researchers have simulated the breakwater wall using numerical method [15].

The use of geosynthetics to manage the settling of structures has been extensively studied [16]. Many practical experiments and theoretical investigations have explored the impact of geotextiles, leading to the finding that they can reduce settlement in sludgy soil. Numerical simulations of rock penetration in muds have also demonstrated the effectiveness of geotextiles in minimizing settlement.

Additional research has indicated that when sand is poured onto mud, the mud soil acts as a non-Newtonian viscous fluid with shear strength dependent on fluid viscosity. In this scenario, the fluid infiltrates between the sand grains, altering the texture and behavior of the mixture to gradually increase its shear resistance. The extent to which mud particles penetrate the aggregate structure is influenced by particle density, stone aggregate size, and the quantity and size of voids between them [17].

Hence, according to the given information, the stone boulder breakwaters located on unstable, waterlogged clay beds experience significant settling of materials. Consequently, a research project was carried out at Siyadi Port breakwater, in Iran utilizing geotechnical research data and construction observations. The objective was to create a computer model using specialized software to understand the response of the clay bed to the weight of the rocks. Soil resistance parameters that could not be determined through standard tests were derived through a process of back analysis. The study also investigated the effects of the thickness of the loose layer, variations in sea water levels, and the use of geotextile in the project. Additionally, the research explored the behavior of the soil when the soft soil properties during construction is modified due to penetration of the rock through mud soil.

2. Method Analysis

2.1. Project description

This study is based on the ongoing project of constructing a breakwater at the Delwar fishing port on the coast of Delwar city, located on the Persian Gulf. The project involves building a stone boulders breakwater, which has been completed along 60 meters of the total 1300 meters length. Geotechnical studies included drilling three sea boreholes to depths of 30 meters and conducting in situ standard penetration tests and vane shear tests. However, due to the loose upper layer of soil, it was not possible to carry out in-situ or reconstructed tests to measure the soil's resistance parameters. The upper layer of the boreholes, excavated to a depth of 4 to 7 meters, consists of a very soft, gray-colored clay resembling mud. The SPT hammer easily penetrates this layer due to its weight. The gray-colored soft clay layer, containing approximately 50% carbonate, falls under the category of calcareous mud and calcareous, and is classified as lean clay (CL) according to the Unified classification standard. From a depth of 7 meters to the bottom of the borehole, loose to semi-dense silt and sand in a light brown color were observed, becoming very dense beyond 9 meters. These layers are categorized as unified SM and ML. In the BH-3 borehole, a layer of gray SP-SM sand was observed at a depth of 7.5 to 9 meters. Generally, granular layers of suitable density were observed from 8 to 9 meters deep. Crushed shell fragments were observed in the upper layers up to a depth of 7 to 7.5 meters. Table 1 shows the soil characteristics in BH-1 borehole, the closest borehole to the research site.

Table 1. Soil profile sample in BH-1 borehole, the closest borehole to the research site

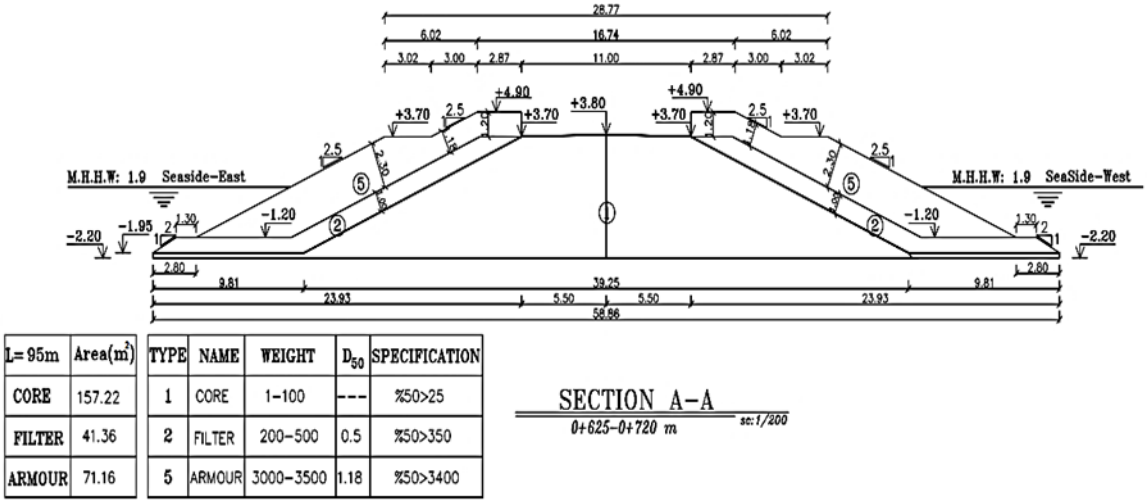
No	Depth(m)	Unified Classification	LL	PI	Cc	Cu	D_{100} mm	D_{60} mm	D_{30} mm	D_{10} mm
Bh-1	2.2-2.5	CL	32	11	-	-	9.51	0.006	-	-
Bh-1	6.7-7.0	CL	35	13	-	-	0.15	0.005	-	-
Bh-1	8.7-9.0	ML	NLL	NPI	-	-	2	0.008	0.001	-

Table 2 displays the properties of the soil in the top two layers of the bed. The extreme softness of the clay made it impractical to conduct in-situ tests or laboratory remolding, so the figures provided are estimates from the consulting company.

Table 2. Consultant's recommended parameters for soil type

Soil properties	Classified soil		
	Very soft clay	Soft clay	Unit
Depth	0-4	4-7	m
Interior friction angle (ϕ)	15-20	20-22	Degree
Cohesion (C_u)	0.07	0.2	kg/cm^2
Elasticity modulus (E)	10-20	30-40	kg/cm^2
Poisson's ratio (μ)	0.45	0.45	-
Density (γ)	1.75-1.85	1.8-1.9	gr/cm^3
OCR	1	1	

The breakwater (Figure 1) being constructed on the seabed close to the shore is made of locally sourced stone materials and is comprised of three layers: core, filter, and armor. The core layer consists of stones weighing between 1 and 100 kg each, the filter layer contains aggregates weighing between 200 and 500 kg, and the armor layer consists of stones weighing between 1500 and 3500 kg. The maximum void space between the stones in the armor layer is 37%, while the other layers have approximately 30% void space between the stone aggregates.



L= 95m	Area(m^2)
CORE	157.22
FILTER	41.36
ARMOUR	71.16

TYPE	NAME	WEIGHT	D_{50}	SPECIFICATION
1	CORE	1-100	---	%50>25
2	FILTER	200-500	0.5	%50>350
5	ARMOUR	3000-3500	1.18	%50>3400

Figure 1. Breakwater section

There is no update on the project's progress along the coast up to a distance of 560 meters from the project's starting point. Between this point and a distance of 620 meters, it is evident that the quantity of stone materials utilized in the project exceeded the originally estimated amount outlined in the project plans. Consequently, the contractor raised concerns about significant settling of the bed during execution, prompting the use of settlement measuring devices to verify the bed's settlement. The device, depicted in Figure 2, comprises a 100 x 100 cm metal plate with a perpendicular index rod welded to it. These plates are positioned at various locations on the bed, and the height of each point is measured and recorded at regular intervals using a leveling instrument.



Figure 2. Index of settlement plates and erection at sea

Table 3 and Figure 3 display the longitudinal and transverse placement of the settlement measurement tools, while the transverse arrangement of settlement plates is depicted in Figure 3(a). The outcome of multiple measurements taken at various times is illustrated in Figure 3.

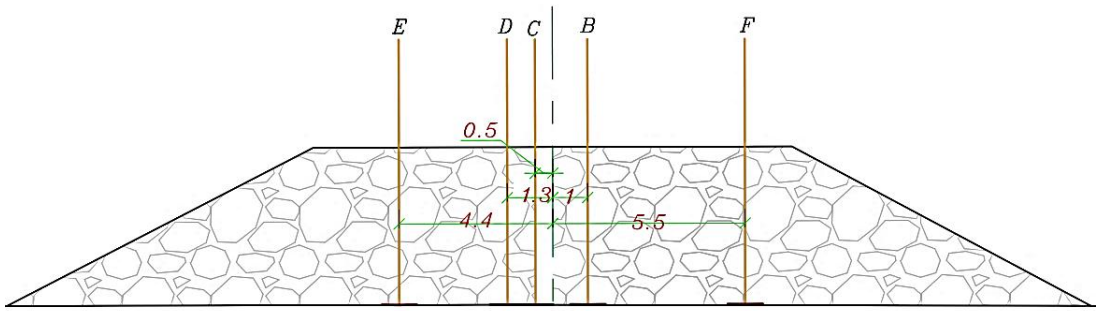
Table 3. The longitudinal and transverse placement of the settlement measurement tools

Gauge	Distance from symmetry axis	Distance from project starting point
B	1	586
C	0.5	597
D	2.3	605
E	4.4	620
F	6.2	622

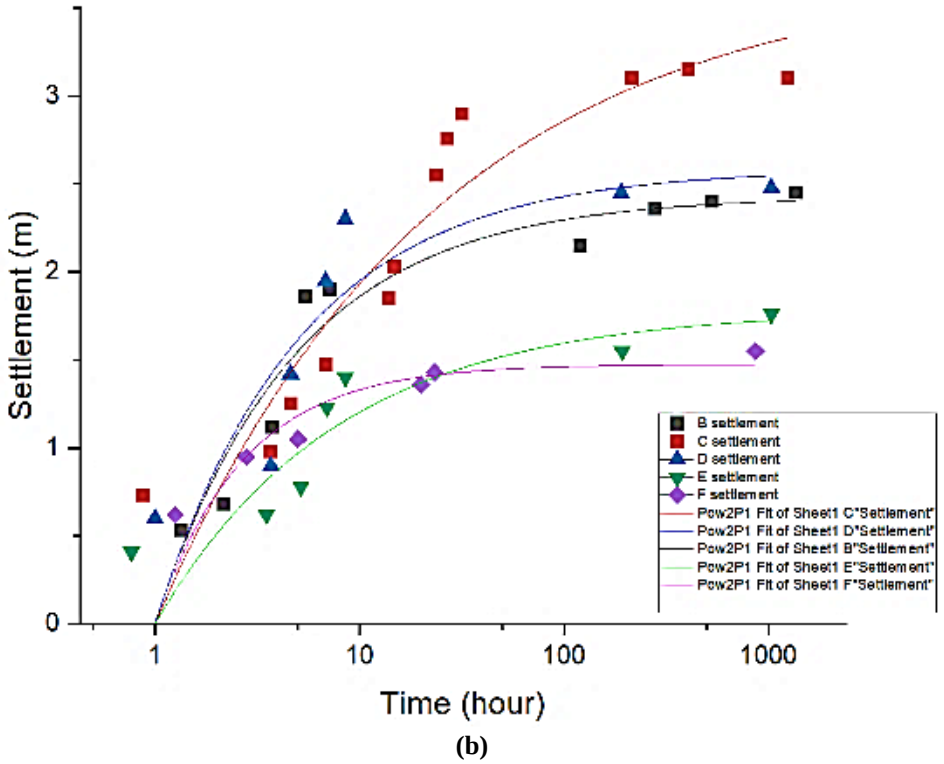
2.2. Preliminary modeling and back analysis to determine parameters of soft clay layer

The consulting engineers' predicted results were significantly different from the actual observations. As a result, it was determined that the research would involve using the FLAC 2D program to model and assess material settlement, investigate soil behavior under loading, and derive the influential parameters in soil resistance through a back analysis. The Mohr-Coulomb model was employed for this modeling. The settlement measured by settlement plates and the quantity of materials utilized in the project were used as criteria to attain the desired outcomes.

In this simulation, a layer of loose clay measuring 4 meters was placed on top of the soft clay model, with the water level set at mean sea level (M.S.L.). Loading was then gradually and stepwise applied to the soil. The core layer's load was incrementally applied to the soil, and after analyzing and determining the mechanical characteristics of the modeled soil through practical observations, the filter layer was loaded. Following analysis, the armor layer was then applied to the soil. Due to the significant strains experienced by very soft clay elements, when modeling a rock mass embankment on such soil, the software encountered embankment failure and was unable to provide a final answer. Consequently, it was decided to apply loads in the form of uniform and strip loads based on the breakwater's geometry. In this scenario, the soil behaves like a completely viscous substance, and the foundation, which is considered practically flexible with no rigidity, contributes to the deformation of the soil elements independently of the structural deformation above it. The load of the rock mass was calculated considering the porosity of the stone materials, and the specific mass of the pile was determined to be 1700 kg/m^3, accounting for the empty space between the aggregate pieces.



(a)



(b)

Figure 3. (a) The position of settlement plates (b) comparison of measured settlement vs time

The graphic representation of the model generated by the software is depicted in Figure 4. To align the software-generated model settlements with the actual measured settlements, the trial-and-error method was employed by adjusting the soil parameters. The initial parameters suggested by the consultant for the very soft clay were the internal friction angle of 15° to 20°, cohesion (c) of 7KN/m^2, and elasticity modulus (E) of 1.0MN/m^2. The investigation involved keeping the cohesion and elasticity modulus constant while varying the internal friction angle parameter to observe the settlement amount.

This process continues until the model fails. At the failure threshold, the settlement value is assessed. When this value does not match the measured settlement on the site, the internal friction angle and modulus of elasticity are kept constant while the cohesion value is adjusted. These adjustments are made until the model reaches the failure threshold, but the threshold does not accurately predict the settlement. Consequently, the modulus of elasticity is reduced until the model reaches the failure threshold, resulting in increased settlement values and ultimately model failure. However, the settlement value is still less than the average observed at the site. The cohesion parameter is then reduced again to match the average observed value. To validate the results, the horizontal and vertical settlements from the analysis are compared with the recorded settlement volume at the construction site.

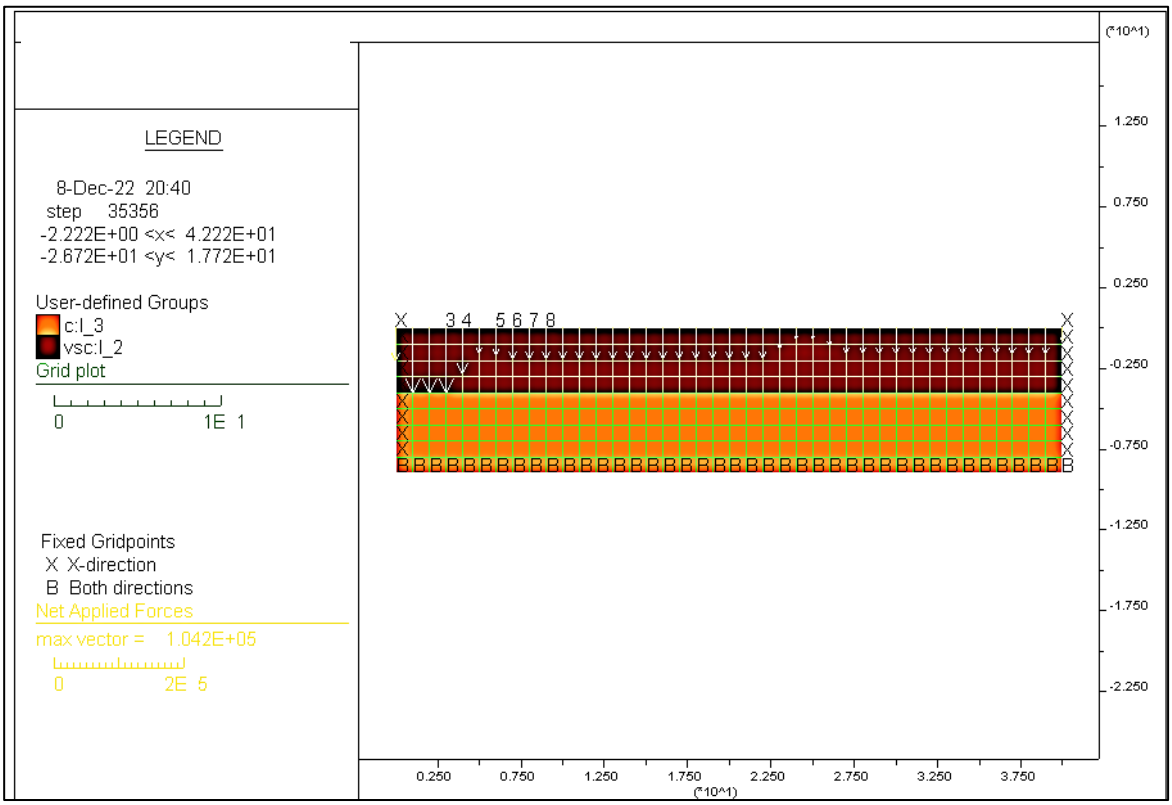


Figure 4. The model designed to apply the primary load during the initial phase of construction.

2.3. Other modeling methods

The question at hand is the potential range for adjusting the parameters selected in the previous step. To address this, a sensitivity analysis was conducted on the parameters obtained from the back analysis to determine the extent of possible changes. This involved keeping two parameters constant, such as the cohesion and the angle of internal friction, while varying the third parameter, modulus of elasticity, until the model reached the breaking threshold. Similarly, the initial parameters were adjusted again by keeping two other parameters constant, such as the modulus of elasticity and cohesion, and varying another parameter, the internal friction angle, to reach the rupture threshold. The potential for adjusting the cohesion was also explored in a similar manner.

To examine the impact of tidal changes in water levels on the breakwater settlement, the modeling process was repeated with adjustments made to the water level and soil pore pressure. Based on findings from geotechnical studies, which identified a sludge layer depth ranging from 4 to 6 meters across the project site, the modeling was updated to account for varying thicknesses of loose soil, and the resulting material subsidence was re-evaluated. The study maintained consistent core uniform load and other parameters. To assess the influence of geotextile on material subsidence, a model was created with the application of a geotextile layer using a cable that lacks bending resistance and only withstands tensile force [18]. The model includes following specifications for these materials: modulus of elasticity: 550 MPa, ultimate tensile strength: 125kPa, ultimate compressive strength: 0 MPa, cross section: $2x10^{-3}$ m^2, visible perimeter: 2m, internal friction angle: 30°. During the construction, one of the leveling plates experienced stage loadings, causing a 3.75-meter subsidence of the material.

2.4. Complete breakwater modeling

In all the situations mentioned above, the authors of this research attempted to simulate real model conditions. However, the loading has only been carried out with the final height of the dike cross-section during coring and with the upper width of the trapezoidal cross-section of coring. This resulted in settlement, causing a significant portion of the material to sink into the bed soil. When the loading of the final cross-section is added to the same modeling, the modeled environment does not converge, and the amount of deformation becomes infinite, making it impossible for the software to balance the forces.

In many previous studies, the entire cross-section of the breakwater has typically been initially modeled and the displacement of the elements/nodes has been calculated. However, in practical scenarios, the sinking of materials into the mud bed results in the bed reaching a certain level of relative strength, serving as a foundation for the breakwater structure. This means that material subsidence slows down to some extent, and the behavior of the mixed stone and mud materials becomes more akin to the elasto-plastic environment of traditional soils. As a result, a new model was developed, and based on the findings from the previous analysis, a bed with updated properties was defined (Figure 5).

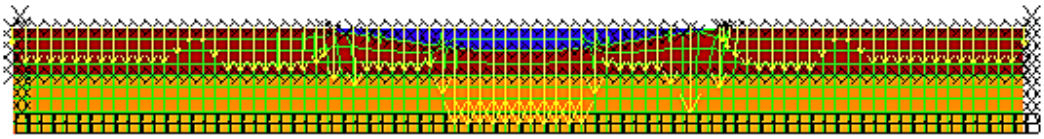


Figure 5. Simulating the impact of a complete breakwater load and updating the mechanical requirements for the settled area in the nearby community.

3. Analysis of the results

When stone materials are poured onto silty soil, the soil breaks up and the materials sink into it, behaving similarly to the suspension of solids in high viscosity fluids [13]. The behavior cannot be accurately represented in the modeling carried out in FLAC software, but a continuous environment with plastic soil flexibility properties is modeled. This study is a case study and cannot be universally applied to all regions. To create a comprehensive model, it is necessary to gather information from similar projects and estimate the mechanical characteristics of their materials so that this type of modeling can be generalized for similar soils.

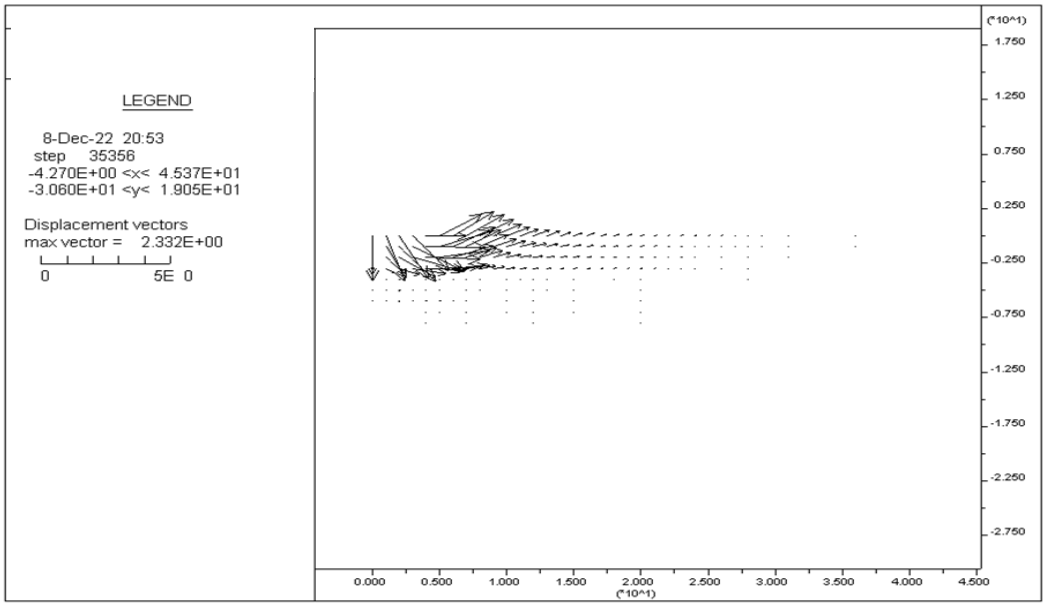
3.1. Comparing the results of the analysis and the actual reports of the site

The findings from the construction of the primary section of the breakwater suggest that settlement increases during the loading of this section. Once the core is finished, the rate of settlement decreases over time and approaches a horizontal line, referring to Figure 3(b). However, the measuring instrument has limitations as it only indicates settlement at one point in the cross-section, and this measurement cannot be extrapolated to the entire loaded cross-section. Furthermore, due to the limited number of measurement plates, comprehensive information about all parts is not available. Therefore, it is essential to integrate the monitoring of the materials used with the measured point settlements to achieve a more precise modeling. To reach such significant deformation, the soil being modeled must have a low modulus of elasticity, as well as low cohesion parameters and internal friction angle to produce the best results. Based on this, the soil resistance parameters were determined as follows: $\phi'=5$, $c=0.11$ kN/m^2, $E=1$ kN/m^2.

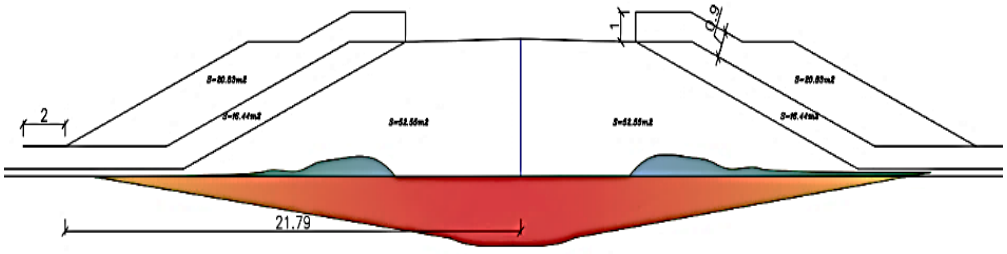
Table 4. Comparison of settlement from site measurement and analysis

Length of project	65	m
Average of designed Section	152	m^2
Designed volume	9880	m^3
Built volume from base level	9679	m^3
The volume of materials used according to the site report	13840	m^3
The volume of material settlement according to the site report	4161	m^3
The volume of material settlement according to the analysis report	3533	m^3
Settlement percentage in site	43	%
Settlement percentage by analysis	35.7	%

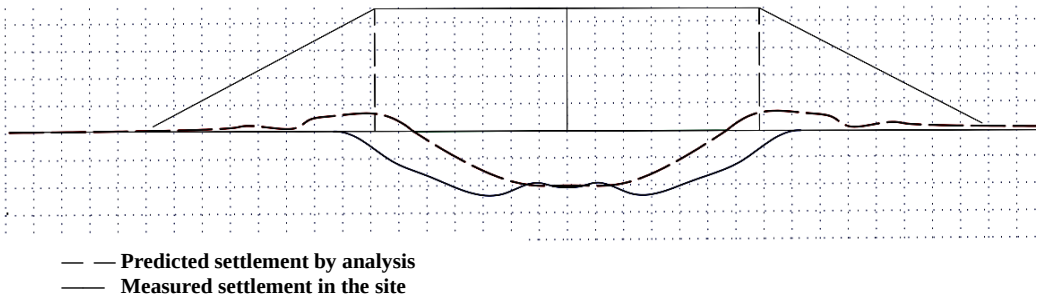
In Figure 6 and Table 4, the vertical settlement in the coring section during breakwater construction are compared to the settlement obtained from the analysis results. It is hard to say that the settlement curve that was produced by software analysis accurately reflects what actually occurred in practice because of the discontinuity of the data derived from the settlement plates. Based on the results of modeling, the materials are moved horizontally in addition to vertical movement. This can be seen in Figure 6(b). In Table 4, the volume of materials immersed in the sludge from the measurements at the site and the results of the analysis are compared.



(a)



(b)



(c)

Figure 6. Measurement of breakwater settlements in modeling (a) displacement of the nodes in the model after completing the core construction phase (b) profile of vertical and horizontal settlement in core with respect to the whole section of the breakwater(c) comparison of vertical settlement measured by settlement plates and settlement obtained from analysis

3.2. Sensitivity analysis

The results of the sensitivity study indicate that the c and φ parameters have a narrow sensitivity range, with just a 2% variation. The modulus of elasticity falls within this sensitivity range of 20%. The coefficient of variation of the modulus of elasticity and the coefficient of variation for the internal friction in this study are in agreement with the findings of [19]. The sensitivity analysis shows that the coefficient of variations of these parameters are as follows: COV(ϕ') = 2˚, COV(c) = 2 kN/m^2, COV(E) = 20 kN/m^2.

3.3. Settlement variation with water surface level variation

During the construction of the project, the difference between the settlement at the time of the tide was not measured because it could not be measured. The results of the analysis show that during the shortest tide (the water level is 2 meters above the bed level), the settlement is a maximum of 2.5 meters. During the highest tide (water height compared to the bed level is 3.8 meters), the settlement is estimated to be 1.4 meters. Such measurement requires the use of specific and accurate tools. But the effect of water level on the amount of settlement was included in the modeling. The findings show that during the shortest tide, the settlement increases. This issue can be explained due to the lower pore water pressure. For this reason, at the time of the highest tide where the water level on the surface of the bed is higher, the settlement decreases. Figure 7 shows the difference in bed level changes. Mud wave tops are getting shorter as a result of the rising water level.

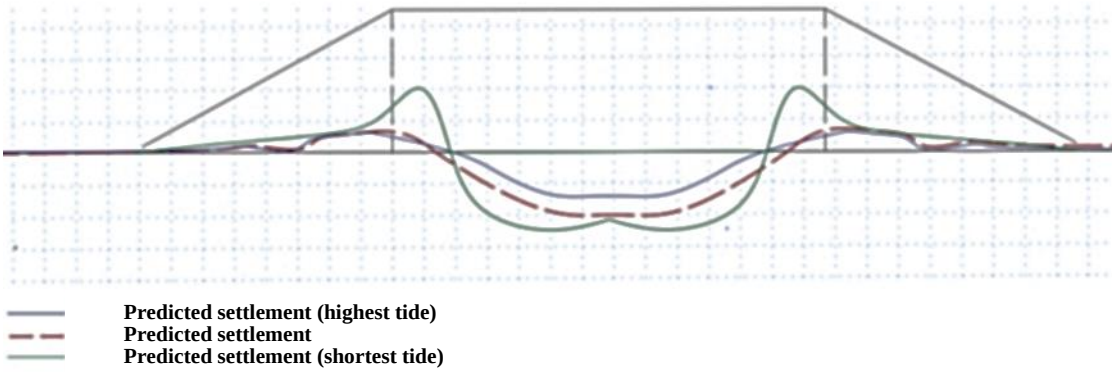


Figure 7. Comparison of bed level changes against water level changes

3.4. Settlement against thickness of loose soil

Measuring the settlement is crucial because the thickness of loose clay fluctuates along the project's longitude profile. The quantity of settlement varies with changes in the loose soil's thickness. Figure 8 demonstrates how the loose layer's thickness increases the settlement. Thus, it can be argued that stone material essentially penetrates to the surface of the second clay layer especially when the thickness of the loose layer exceeds 6 meters. Table 5 displays the settlement figures in this case.

Table 5. Settlement vs the thickness of weak layer

Mud depth(m)	Max settlement(m)
4	2.0
5	4.0
6	5.5

The findings of other studies [20] demonstrate that the bearing capacity of the soil is a function of the thickness of the loose layer, the ratio of the depth of the layer to the width of the foundation and the cohesion ratio of the two consecutive soil layers. By increasing the ratio of the depth of the loose layer to the width of the foundation, the bearing capacity decreases.

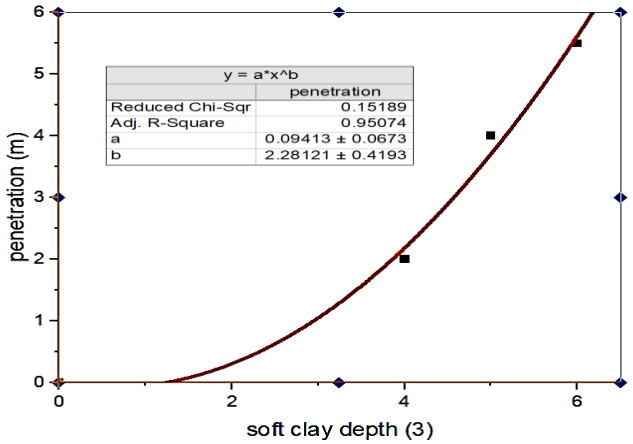


Figure 8. The diagram of settlement variation vs the thickness of the loose layer

3.5. The effect of using geotextile on the settlement

Geotextile is a commonly utilized material in practical works that is approved for its ability to reduce settlement [21]. By applying a sample of geotextile to the model in this study, the quantity of settlement was greatly decreased. Figure 9 illustrates that the maximum settlement is limited to a maximum of 70 cm. In actuality, geotextile is a fabric that, because of its high tensile strength, can withstand the tension in its cross section caused by vertical stress from loading without collapsing the materials.

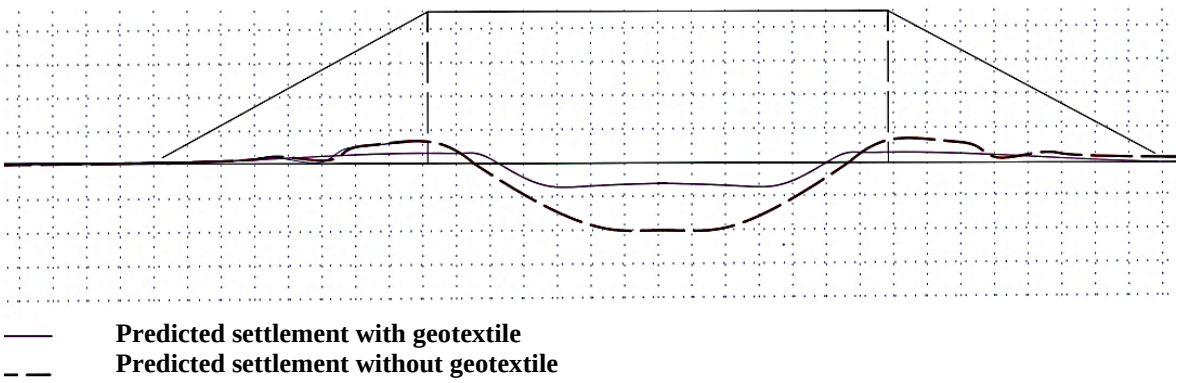


Figure 9. Comparison of settlement with and without geotextile application

3.6. Stage loading

As seen in Figure 3.1, the loading in the present modeling is based on the full height of the breakwater core up to the top of the breakwater and with full width.. There are two methods used to pour stone materials in place during construction: using a truck to pour the materials directly, or using an excavator to move the stone materials from the depot to the construction site. If the materials are poured gradually across the width, we will witness less settlement than if they are poured locally and in a huge volume all at once, as the former scenario causes large settlements. One explanation for this could be that the lateral resistance of the soil increases as the material sinks into the loose layer of mud because the properties of the newly formed material, which is made of both stone and mud, change. Additionally, the loading in the subsequent stages is comparable to the placement of aggregates on a wide flexible foundation. Therefore, a stage loading was modeled according to the data presented in Table 6. The settlement variation diagram measured at the site due to stage loading is depicted in Figure 10(a), while Figure 10(b) displays the analysis conclusion. The final settlement in these figures is comparable and have few differences.

Table 6. Stage settlement recorded in the site

Time	Load step	Sea Level	Water Depth	Gauge	Net Settlement
11:20	0	1.1	3.1	4.51	-0.49
14:05	1	0.54	2.54	4.25	-0.75
15:10	0	0.48	2.48	3.97	-1.03
15:20	2	0.45	2.45	3.65	-1.35
16:45	0	0.6	2.6	3.7	-1.3
17:00	3	0.63	2.63	3.53	-1.47
17:05	0	0.65	2.65	3.45	-1.55
17:30	4	0.72	2.72	3.42	-1.58
10:05	0	1.2	3.2	3	-2
10:30	5	1.15	3.15	2.45	-2.55
17:05	0	0.5	2.5	2.2	-2.8
17:30	6	0.6	2.6	1.8	-3.2
10:03	0	1	3	1.8	-3.2
10:27	7	1.1	3.1	1.5	-3.5
08:03	0	0.7	2.7	1.4	-3.6
08:23	8	0.75	2.75	1.25	-3.75

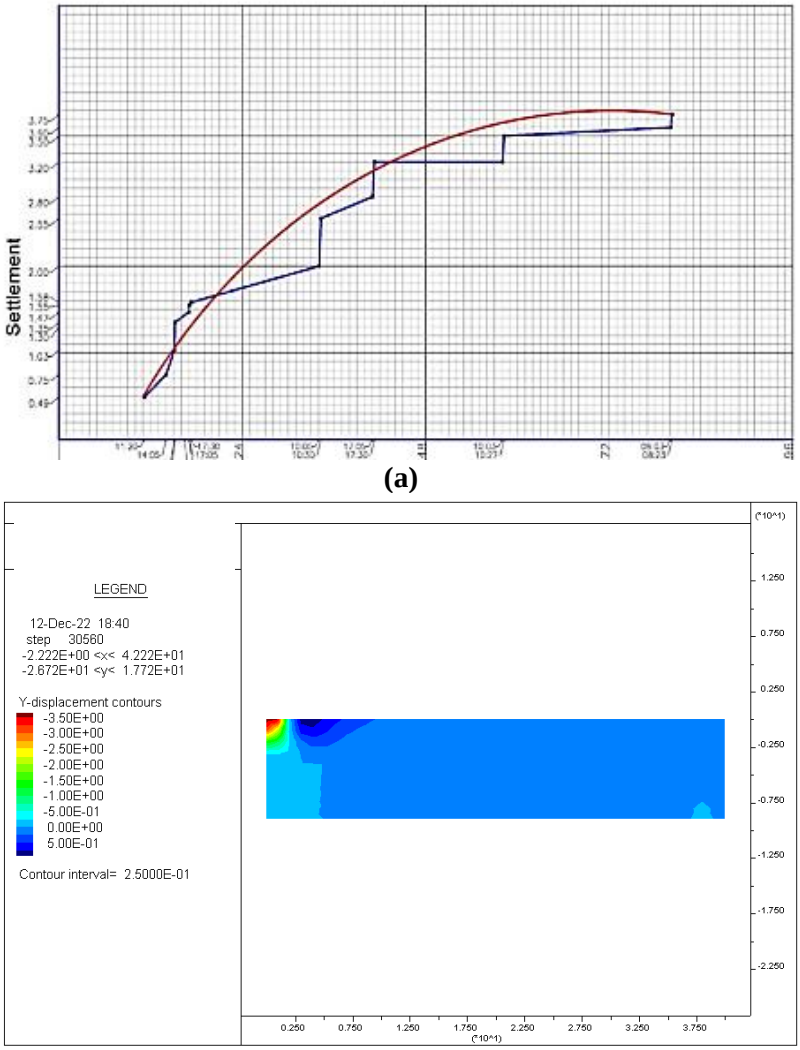


Figure 10. Settlement diagrams under stage loading (a) Recorded diagram of settlement caused by stage loading in the construction site (b) Settlement diagram resulting from modeling under stage loading

3.7. Modeling using the modification of the soft soil properties during construction

In Figure 6(c), the predicted and measure settlement does nnot coincide except in the middle of the section. In addition, during modeling, if the full load of the breakwater section is applied to the model, the soil will break and the equilibrium equations will not converge. This divergent contradicts what happens in practice. Basically, after the settlement caused by core loading was reduced, the section of the breakwater can be built based on the executive plans and all the stone layers can be implemented in place. This means that the rock material embedded in the mud creates new material that acts as a flexible foundation. During the completing of the work, the changes of the finished surfaces have been taken at different times that the modeling is made separately for this purpose, finding new parameters for the combination of mud and stone soil shows that the resistance parameters of the soil are improved.

With the method of back analysis and trial and error, the main soil parameters were estimated, which are: C=0.4 kPa, φ=30 and E=25 kPa. As shown in Figure 11, based on these parameters, settlement values can be seen in the breakwater, which are consistent with the observations of the breakwater settlement at the time of construction. In this case, the maximum settlement in the toe of the breakwater reaches about 50 cm and in the middle parts it is about 30 cm.

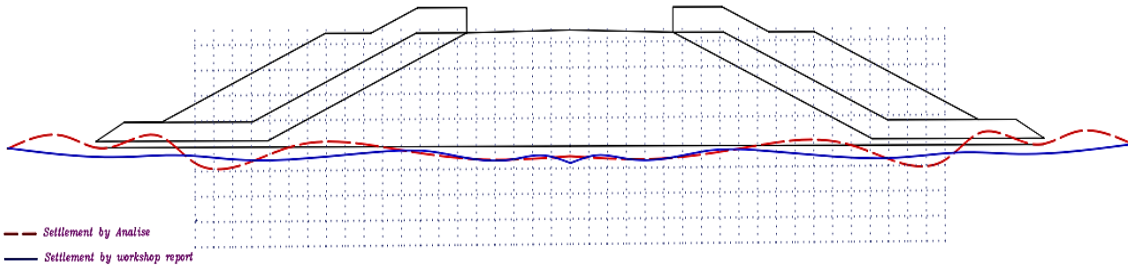


Figure 12. Modeling using the modification of the soft soil properties during construction

4. Conclusions

Installed on loose mud beds, stone boulder breakwaters sink deeply into the mud. Practical, laboratory, and numerical modeling research must be done in order to ascertain the relationship between the mechanical qualities of muddy soil and the quantity of rock material that penetrates it during construction. This must be followed by theoretical relationships. Calculating soil characteristics utilizing experimental data (during project building or laboratory models) and back analysis is required in order to use a more accurate model. Therefore, utilizing information from geotechnical investigations and construction inspections, a research project was conducted on the breakwater at Bandar Siyadi in Iran. The idea was to use specialist software to build a computer model that would show how the clay bed would react to the weight of stones. Through a back-analysis procedure, soil resistance values that are not determinable by normal tests were acquired. The impacts of variations in sea level, the thickness of loose layers, and the project's use of geotextile were also examined in this study. This study also looked at how soil behaves when mud soil infiltration causes rock to seep through soft soil during construction. The modeled soil should have a low modulus of elasticity, low adhesion characteristics, and a low internal friction angle in order to achieve such substantial deformation. According to the sensitivity analysis, these parameters' coefficients of variation are as follows:

$COV(\phi') = 2^{\circ}$, $COV(c) = 2\ kN/m^2$, $COV(E) = 20\ kN/m^2$.

The modeling results also indicate that a large rise in settling is anticipated as the muddy soil's depth increases. Additionally, it is crucial to re-model the settled materials with updated attributes from the previous step in order to comprehend the construction of an entire breakwater section on muddy soil. With this method, long-term settlements and the stability of the breakwater section may be reliably predicted. This study also confirms earlier findings about the effectiveness of using geotextiles for settlement management. Instead of dumping the materials all into one place during building, it is recommended to spread them equally and gradually around the bed using modeling stage construction.

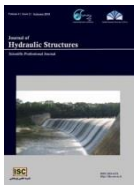
References

1. Emmanuel E, Lau CC, Anggraini V, Pasbakhsh P (2019) Stabilization of a soft marine clay using halloysite nanotubes: A multi-scale approach. Applied Clay Science 173:65-78
2. Vafaeipour Sorkhabi R, Naseri A, Alami MT, Mojtahedi A (2022) Experimental study of an innovative method to reduce the damage of reshaping rubble mound breakwaters. Innovative Infrastructure Solutions 7 (6):353
3. Kurihara O, Takahashi H (2023) Backfilling configuration to improve tenacity of composite-type breakwaters. Coastal Engineering Journal 65 (2):217-233
4. Zhou B, Zheng Z, Zhang Q, Jin P, Wang L, Ning D (2023) Wave attenuation and amplification by an abreast pair of floating parabolic breakwaters. Energy 271:127077
5. Habib M, O'Sullivan J, Abolfathi S, Salauddin M (2023) Enhanced wave overtopping simulation at vertical breakwaters using machine learning algorithms. Plos one 18 (8):e0289318
6. Zhou J, Zhao X, Zang J, Geng J, Sun S (2023) Wave power extraction by an oscillating water column array embedded in comb-type breakwaters: Performance analysis and hydrodynamic mechanism. Physics of Fluids 35 (7)
7. Mata MI, van Gent MR (2023) Numerical modelling of wave overtopping discharges at rubble mound breakwaters using OpenFOAM®. Coastal Engineering 181:104274
8. Chen Y-k, Liu Y, Meringolo DD, Hu J-m (2023) Study on the hydrodynamics of a twin floating breakwater by using SPH method. Coastal Engineering 179:104230
9. Hassanpour N, Vicinanza D, Contestabile P (2023) Determining Wave Transmission over Rubble-Mound Breakwaters: Assessment of Existing Formulae through Benchmark Testing. Water 15 (6):1111
10. Falamaki A, Eskandari M, Baghlani A, Ahmadi SA (2013) Modeling total sediment load in rivers using artificial neural networks. Journal of Water and Soil Resources Conservation 2 (3):13-26
11. Mobarrez R, Ahmadi-Tafri H, Fakher A An essential foundation control for the design of rubble mound breakwaters on soft soil. In: International Conference on Geotechnical Engineering, 2004. pp 3-6
12. Ghaderi D, Rahbani M (2023) Simultaneous employment of hydrodynamical simulation and RS imageries for analyzing the influence of an anthropogenic construction on shoreline transformation. Journal of Hydraulic Structures 9 (3):14-31. doi:10.22055/jhs.2023.44699.1262
13. Nagaraj H, Sravan M, Deepa B (2021) Factors influencing undrained strength of fine-grained soils at high water contents. Geomechanics and Geoengineering 16 (4):325-329
14. Fan N, Nian T-K, Guo X-S, Jiao H-B, Lu S (2020) Piecewise strength model for three types of ultra-soft fine-grained soils. Soils and Foundations 60 (4):778-790
15. Abdolmaleki M, Kamalan H (2019) Modeling of Vertical Breakwater Wall under Bilateral Seawater Load. Journal of Hydraulic Structures 5 (1):89-97. doi:10.22055/jhs.2019.30747.1120

16. Noori MS, Dehghanian K (2021) Settlement Analysis of Geosynthetics Reinforced Embankments. Dicle Üniversitesi Mühendislik Fakültesi Mühendislik Dergisi 12 (4):699-709
17. Feng W-Q, Li C, Yin J-H, Chen J, Liu K (2019) Physical model study on the clay–sand interface without and with geotextile separator. Acta Geotechnica 14:2065-2081
18. Alfaro M, Blatz J, Graham J (2006) GEOSYNTHETIC REINFORCEMENT FOR EMBANKMENTS OVER DEGRADING DISCONTINUOUS PERMAFROST SUBJECTED TO PRESSTRESSING. Lowland Technology International 8 (1, June):47-54
19. Uzielli M, Lacasse S, Nadim F, Phoon KK (2006) Soil variability analysis for geotechnical practice. Characterization and engineering properties of natural soils 3:1653-1752
20. Lotfizadeh MR, Kamalian M (2017) EVALUATION OF BEARING CAPACITY OF STRIP FOUNDATION BASED ON CONSECUTIVE LAYERS OF WEAK AND STRONG CLAYS BY CHARACTERISTIC LINES METHOD. Sharif Journal of Civil Engineering 33.2 (3.1):31-38. doi:10.24200/j30.2017.20063
21. Holmes D, Horrocks A (2016) Technical textiles for survival. In: Handbook of Technical Textiles. Elsevier, pp 287-323

© 2024 by the authors. Licensee SCU, Ahvaz, Iran. This article is an open access article distributed under the terms and conditions of the Creative Commons Attribution 4.0 International (CC BY 4.0 license) (http://creativecommons.org/licenses/by/4.0/).

Journal of Hydraulic Structures
J. Hydraul. Struct., 2024; 10(1): 46-65
DOI: 10.22055/jhs.2024.45673.1278



OPEN ACCESS

Investigation of the Performance of Soft Computing Methods in the Hydraulic Evaluation of the Slot Fishway on the Inclined Drop

Ehsan Aminvash [1]
Farhoud Kalateh [2]
Rasoul Daneshfaraz[3]
John Abraham[4]

Abstract

The present research investigates K-Nearest Neighbor (K-NN) and Support Vector Machine (SVM) algorithms for evaluating hydraulic parameters of inclined drops equipped with fishway elements. 395 measurements were analyzed using these two algorithms with a focus on $\Delta E/E$ and y_d/H. To evaluate algorithm effectiveness, three accuracy measures: R^2, RMSE, and the KGE are used for a number of different scenarios. The SVM results show that in the first and second scenarios, respectively, model number 13 yielded RMSE=0.0156, R^2=0.973, and KGE=0.961 for the training mode and RMSE=0.0241, R^2=0.962, and KGE=0.952 for the testing mode. The K-NN algorithm with 75% of the total data employed for the initial sample size gave the best results with RMSE=0.0121, R^2=0.986, and KGE=0.975 for the first scenario and RMSE= 0.0123, R^2= 0.986, and KGE= 0.975 for the second scenario. Also, the results stated that the RBF kernel function is superior among the kernel functions of the SVM algorithm and the Cityblock distance measurement method among other methods of the K-NN algorithm. On the other hand, the K-NN method was superior to the SVM method.

Keywords: Fishway elements, Inclined drop, K-NN algorithm, SVM algorithm.

Received: 29 December 2023; Accepted: 18 March 2024

1. Introduction

One of the most essential things that must be paid attention to in the design of hydraulic structures is in terms of stability management. It is very important to keep the fish healthy and not lose them in the fishway structures. In the present research, we decided to investigate the flow on inclined drops by considering environmental considerations. The goals of the design are to

[1]Faculty of Civil Engineering, University of Tabriz, Tabriz, Iran, Email: Ehsan.aminvash1994@gmail.com **(Corresponding author)**
[2] Faculty of Civil Engineering, University of Tabriz, Tabriz, Iran.
[3] Faculty of Engineering, University of Maragheh, Maragheh, Iran.
[4] University of St. Thomas, School of Engineering, St Paul, USA.

simultaneously provide energy dissipation, protect downstream structures, increase aeration of the flow, improve water quality, and allow the migration of fish. Creating turbulence and mixing water and air is one of the most effective methods to increase energy losses downstream of an inclined drop. These structures are built for environmental and economic considerations. The design of these structures is such that it allows the fish to enter and exit easily without incurring injury and without unnecessary delay for spawning. The aim of the present research is to investigate the performance of neural network methods for evaluating the hydraulic parameters of inclined drops equipped with fishway elements.

Zhang et al. [1] designed a new multi-slot and pool-overflow combined fishway channel based on hydraulic property analysis and fish-passage test. Zhong et al. [2] numerically and experimentally evaluated the hydraulic parameters of the new semi-frustum in the pool-overflow fishway path and showed that the fish path with bed slope and inverse radius ratio, but with a longer pool distance, performs better. Zheng et al. [3] conducted a comparative study of the hydraulic characteristics of natural fish tracks and showed that a weak circulation zone is formed in the low-velocity region, which makes swimming easier for migratory fish. Baki and Azimi [4] studied the hydraulic design of slot and rock fishways in a review study. The results of their review and research showed that the long-term progress in the fishway lanes combines with vertical cracks and stone overflow, which finally helps the engineers in designing these instruments. Harris et al. [5] experimentally presented an innovation for tubular fishways and stated that the tubular fishways route has the potential to effectively pass fish upstream in new barriers of more than 5 inches with low construction and operating costs in the regime. Cea et al. [6] numerically investigated the average depth of turbulence for flow in vertical fishways. The results showed the importance of the turbulence model in numerical simulations of this nature.

Rodriguez et al. [7] evaluated the designs of fish passages with vertical slots and their effect on fish mobility. They showed that the amount of energy consumption per unit volume of the pool should not be more than 200 W/m^3 for large anadromous species and 150 W/m^3 for smaller species such as trout. Yagci [8] discussed fishways as eco-friendly structures. In addition to the speed and depth of the flow, which affects the ability of fish to swim, the intensity of turbulence is also important. The patterns of flow and turbulence can be controlled to provide suitable conditions for swimming.

Due to the interaction of the flow structure and the fishway elements, studies on specific laboratory conditions are generally limited in their applicability. Currently, artificial intelligence methods are taking on a larger role as investigation tools for these problems. Among the methods are: data mining methods that are used to model non-linear systems, Artificial Neural Networks (ANN), Gene Expression Programming (GEP), SVM, and K-NN as examples.

Arffin [9] used an ANN model and a linear regression model to predict sedimentation. Alp and Cigizoglu [10] compared the results of RBF and FFBP methods with linear regression and stated that the mentioned methods have provided better results. Using field and laboratory data, Goel and Pal [11] investigated the support vector machine for predicting scour depth and showed that changes in flow conditions, geometry, and bed materials have an effect on scour depth. Roshangar et al. [12] evaluated the efficiency of support vector machine in predicting hydraulic jump in contractions. The results showed that the relative energy consumption and downstream water depth varied with Froude number.

Sadeghfam et al. [13] studied the scrubbing of supercritical upstream of screens in a laboratory and used artificial intelligence methods (SFL, NF, and SVM methods). Daneshfaraz et al. [14] predicted hydraulic parameters of a drop by double screens using support vector machine. The results showed that the experimental hydraulic parameters are in good agreement with the output

results from the support vector machine. Francisco Fuentes-Perez et al. [15] conducted to an autonomous obstruction detection system using hydraulic modeling and sensor networks in a step toward smart fishways with Paython. Results showed that the proposed system allows monitoring of the hydraulic performance of the fishway. Seifollahi et al. [16] estimated local scouring of cylindrical bridge piers using hybrid neural wavelets and artificial neural network methods. The results of their research showed that the neural wavelet method provided superior results than the ANN method. Daneshfaraz et al. [17, 18] have also conducted research in the field of vertical drops with screens and a blocky bed using the artificial network method.

Kalathil and Chandra [19] experimentally and numerically examined the hydraulic design of a step-pool fishway. The results showed that the velocity and the averaged velocity over the crest at 0.10 and 0.25 are considerably lower than at 0.25. Also, the maximum TKE and energy dissipation factors were within recommended limits for 0.10 and 0.25. Baharvand and Lashkar-Ara [20] investigated the hydrodynamic and biological characteristics of a modified meander C-type fishway to pass rainbow trout. The results showed that the TKE distribution graphs for different discharge and geometry scenarios through the longest path in the pools of the MMCF were investigated using the line probe technique for an average depth of 0.5d.

Mirkhorli et al. [21] examined hydraulic aspects of a rectangular labyrinth pool and weir fishway using FLOW-3D; they showed that a conventional weir has less energy dissipation than a rectangular labyrinth weir. Lower TKE and TI values were observed at the top of the labyrinth weir, at the corner of the wall downstream of the weir, and between the side walls of the weir and the channel wall. Baharvand et al. [22] conducted a comparative study using machine learning and regression-based approaches for predicting the hydraulic jump depth ratio. The results of their study show that the proposed model increases the correlation between observed and predicted values up to 0.987 and decreases the RMSE to 0.324. Cassan et al. [23] investigated the hydraulics of rock-ramp fishways with lateral slopes. The results of their research revealed that the method for assessing the stage-discharge relationship and maximum velocities is related to the lateral slope.

According to the research related to the prediction of hydraulic parameters in hydraulic structures, it was observed that the input parameters are very important for the evaluation of independent parameters. Therefore, in the present research, the prediction and evaluation of energy dissipation parameters and downstream depth of inclined structures equipped with fishway elements was performed using K-Nearest Neighbor (K-NN) and Support Vector Machine (SVM) methods. To the best knowledge of the authors, the nearest neighbor method (K-NN) has not been used in this type of study. Consequently, here, for the first time, the evaluation of the hydraulic parameters with K-NN and SVM methods have been performed.

2. Methodology

2.1. Laboratory equipment and fishway elements

In order to check the performance of data mining methods for predicting relative energy losses and downstream depth parameters of the inclined drop; a total of 395 measurements are used. Experiments have been conducted in a hydraulic laboratory in a flume with length, width, and height of 5 meters, 30 cm, and 50 cm, respectively. The ranges of measured parameters are presented in Table 1. For fishway elements, glass plates with length, height, and thickness of 15, 10, and 6 cm respectively; with and without holes; and with angles of 45, 60, and 90 degrees to the horizon are used. The angle of the breakwater structure is 26.56 degrees with respect to the channel floor. The dimensions of the holes in the hollow elements are 5×5 cm. Figure 1 shows a model of the experimental channel and theequipment [24].

Table 1. Range of measured parameters and characteristics of fishway elements

Model Name	α (Degree of fishway elements)	Q (Lit/sec)	y_d (cm)	Fr_d (-)	Reynolds No.	Type of fishway element	
						with hole	without hole
Simple drop	-----	3.33~10	0.6~1.67	4.94~6.93	38986~582857	-----	-----
FW1	90		2.57~14.2	0.19~0.86			*
FW2	60		2.21~10	0.3~0.98			*
FW3	45		2.03~11.25	0.28~1.22			*
FW4	90		4.9~8.21	0.33~0.45		*	
FW5	60		4.46~8.73	0.37~0.42		*	
FW6	45		4.37~8.85	0.38~0.44		*	

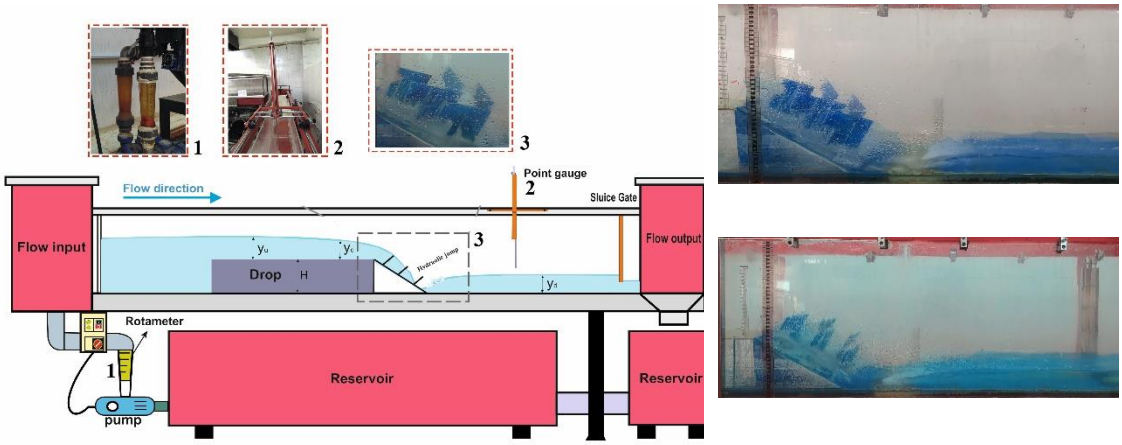


Figure 1. Experimental flume and equipment

2.2. Algorithm of SVM

SVM is a data-mining and machine-learning algorithm. It is divided into two modes (testing and training) and is applied for prediction and data classification. Machine learning requires input data; a portion of the data is used as training data and the remaining data is reserved for testing. The software calculates the dependent parameter based on independent parameter values. The SVM algorithm has various parameters, the most important of which is the kernel parameter or γ, the setting of which is important for the solution of the problem.

2.3. SVM theory

The SVM method entails classification and linear separation of data. If the data is linear, an attempt is made to separate them and maximum margins are calculated (shown graphically in Fig. 2); the size of the separating plate can be calculated from Eq. (1).

$$\text{Margin}=\frac{2}{\|w\|}=\frac{2}{w^T w} \quad (1)$$

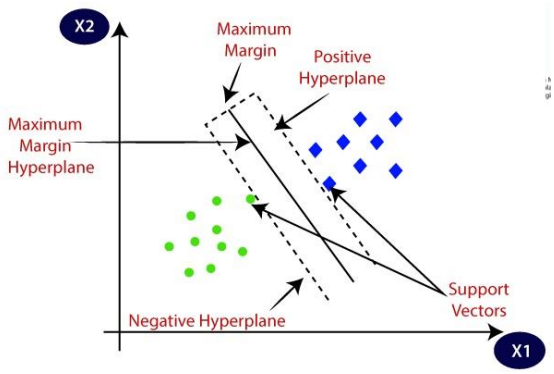


Figure 2. Data classification and support vector [17]

The best separating page is the page with the largest distance between two classes. In this case, the absolute value of *w* should be assigned the lowest value. The kernel function is defined as φ; it transfers data from the *x* space to the *z* space [17, 18].

$$\varphi : x \to z \qquad z=\varphi(x)$$

As a result, the separator equation is written as Eq. (2):

$$w^T z + b = f(x) = 0 \to w^T \varphi(x) + b = 0 \tag{2}$$

In Eq. (2), which is the relationship between the target variable and the input variables, φ(x) is the kernel, $f(x)$ is the target function, w is the vector coefficient, and b is a constant value. The objective function, which is a convex function, has an optimal solution. Equation (3) is used to find the optimal page [12].

$$\min \frac{1}{2} \sum_{i=1}^{n} \sum_{i=1}^{n} \alpha_i \alpha_j y_i y_j \varphi(x_i)^T \varphi(x_j) - \sum_{i=1}^{n} \alpha_i \qquad 0 \le \alpha_i \le c \tag{3}$$

Instead of the expression $\varphi(x_j)\varphi(x_i)T$, a more general state can be defined as $k(x_i,x_j)$, which can be used to enter more complex spaces. The process is often called a kernel trick. As a result, Eq. (3) can be presented as Eqs. (4) and (5).

$$y = sign(\sum_{i=1}^{n} \alpha_i y_i k(x_i, x) + b) \tag{4}$$

$$b = \frac{1}{|s|} \sum_{i=1}^{n} [y_i - \sum_{j=1}^{n} \alpha_j y_j k(x_j, x)] \tag{5}$$

2.4. Algorithm of K-NN

The K-NN method is a non-stationary statistical method that is used for classification and regression. In both of the above cases, K-NN includes the closest training sample in the data space and its output varies depending on the type used in classification and regression. In the

classification mode, it calculates the distance of a point marked by a label with the nearest points. Since the calculations of this algorithm are based on distance, data normalization can help improve its performance (Figure 3).

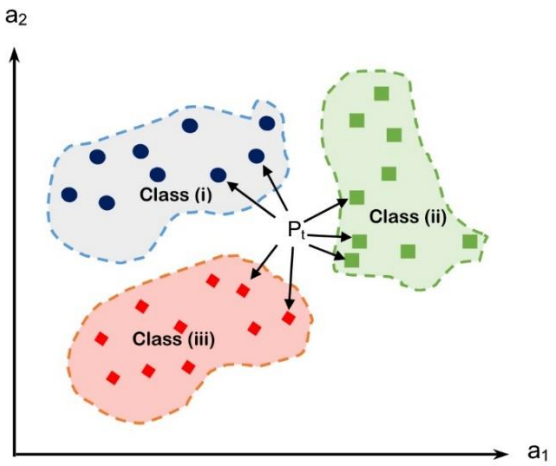


Figure 3. K-NN classification

The primary data are vectors in a multidimensional space, each of which contains a label called a category. The learning mode or training mode of the algorithm includes the storage of the feature vectors and the class label of the prototype. In the classification phase, K is a constant defined by the operator and the unlabeled vector is has the largest number in K-NN for that point. Distance measurements for continuous variables are usually a Euclidean distance. The K-NN algorithm includes the following steps:

Step 1: Load data

Step 2: Select K as the nearest neighbor number

Step 3: For each of the primary datapoints:

- The distance between the data in question and each of the primary data is calculated.
- Add the distance and index of the prototype.
- Sort the collection based on distance from small to large.
- Select K points of the first member of the sorted set.
- Output results.

There are a number of advantages with the K-NN method. First, there is no presupposition about the data. Second, it has a simple algorithm but yields relatively high accuracy. Third, it is a multipurpose method (classification and regression). Among its disadvantages, since the algorithm stores all the previous data, it requires a lot of memory. The prediction stage with a large K may be slow. The flowchart of data evaluation steps from start to finish is shown in Figure 4.

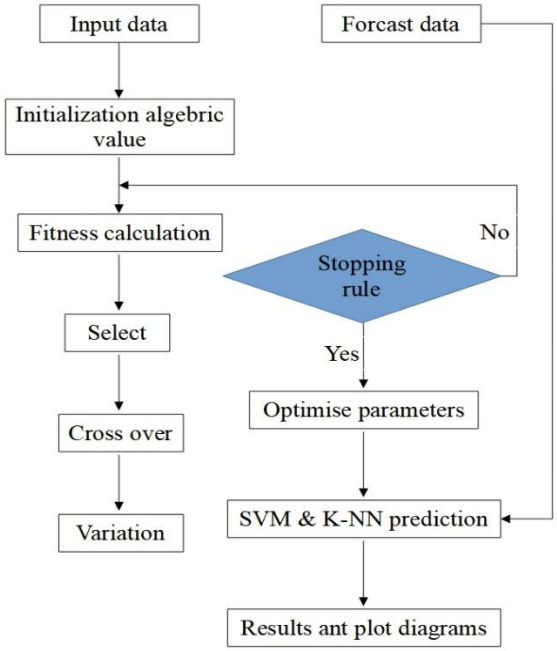


Figure 4. SVM and K-NN modelling and configuration flowchart

2.5. Dimensional analysis

Taking into account the geometric and hydraulic characteristics of the flow research models according to the research of [18], the effective parameters for the inclined drop along with the fishway elements are presented in the form of Eq. (6).

$$f_1(q, H, \theta, y_u, y_c, y_d, \mu, \rho, g, \alpha, a, b, x, L_{air}, L_j, E_u, E_d) = 0 \tag{6}$$

Dimensional analysis was performed by using the Buckingham-Π method, Eq. (7) was obtained.

$$f_2(\frac{y_u}{H}, \frac{y_c}{H}, \frac{y_d}{H}, \theta, \alpha, \frac{a}{H}, \frac{b}{H}, \frac{x}{H}, \frac{L_{air}}{H}, \frac{L_j}{H}, \frac{q}{H\sqrt{gH}} = Fr, \frac{q\rho}{\mu} = \mathrm{Re}, E_u, E_d) = 0 \tag{7}$$

Then we have:

$$\frac{\Delta E}{E_u} = f_3(\frac{y_c}{H}, \frac{y_d}{H}, \theta, \alpha, \frac{a}{b}, \frac{x}{H}, \frac{L_{air}}{H}, \frac{L_j}{H}, \frac{q}{H\sqrt{gH}} = Fr_{0,d}, \frac{q\rho}{\mu} = \mathrm{Re}_u) \tag{8}$$

Since the range of Reynolds number in this research is between 39000 and 58000, which represents the turbulent flow regime, the Reynolds number can be ignored. Also, parameters x/H and θ were omitted because they have fixed values. Thus, we have:

$$\frac{\Delta E}{E_u}, \frac{y_d}{H_d} = f_4(Fr_0, \frac{y_c}{H}, \alpha) \quad (9)$$

$$\frac{\Delta E}{E_u}, \frac{y_d}{H} = f_4(Fr_0, \frac{y_c}{H}, \frac{a}{b}, \alpha) \quad (10)$$

2.6. Evaluation parameters

Three statistical parameters are used to predict the relative energy consumption and the relative downstream depth using SVM and K-NN algorithms. RMSE, R^2, and the Kling-Gupta coefficient (KGE) are presented in the Eqs. (11) to (13), respectively. The index *E* is related to the experimental values, *P* is related to the evaluated values, and *n* is the numbers of data.

$$RMSE = \sqrt{\frac{1}{n}\sum_{i=1}^{n}(S_E - S_P)^2} \qquad \text{if RMSE} \rightarrow 0\text{: best answer} \quad (11)$$

$$R^2 = \left[\frac{\left(n\sum S_E.S_P\right) - (\sum S_E).(\sum S_P)}{\sqrt{n(\sum S_E^2) - (\sum S_E)^2}.\sqrt{n(\sum S_P^2) - (\sum S_P)^2}}\right]^2 \qquad \text{if: } R^2 \rightarrow 1\text{: best answer} \quad (12)$$

$$KGE = 1 - \sqrt{(R-1)^2 + (\beta-1)^2 + (\gamma-1)^2}, \beta = \frac{\overline{Pre}}{\overline{Obs}}; \gamma = \frac{\sigma_{Pre} / \overline{Pre}}{\sigma_{Obs} / \overline{Obs}} \qquad \text{if: KGE} \rightarrow 1\text{: best answer} \quad (13)$$

3. Results and Discussion

In this study, two scenarios have been designated; the first scenario is the evaluation of relative energy dissipation and the second scenario is related to the evaluation of the relative downstream depth of the drop. In SVM, there are different kernels, among which RBF, linear and polynomial functions are used. For the K-NN algorithm, there are three methods to measure the distance between neighbors: Euclidean, Cityblock (Manhattan) and Chebychen. In order to estimate the relative energy dissipation from an inclined drop equipped with fishway elements, different data sets were allocated to training and testing. The results of the analysis are presented in Table 2 for both methods, 75% of the data was allocated to training and the remaining 25% for testing.

Table 2. Evaluation criteria of different percentages of training and testing in the best models in SVM

Scenario no.	Criteria evaluation	60-40%	65-35%	70-30%	75-25%	80-20%
1st scenario:	RMSE	0.0765	0.0739	0.0749	0.0241	0.0788
Energy	R^2	0.767	0.799	0.821	0.962	0.737
dissipation	KGE	0.796	0.782	0.864	0.952	0.765
2nd scenario:	RMSE	0.0523	0.0511	0.0518	0.022	0.044
Downstream	R^2	0.705	0.739	0.763	0.923	0.741
depth	KGE	0.743	0.741	0.751	0.941	0.758

In the first scenario ($\Delta E/E_0$) and the second scenario (y_d/H), 13 combinations have been used to evaluate the parameters using the K-NN and SVM methods. In these combinations, $\Delta E/E_0$ and y_d/H parameters are dependent parameters and Fr_0, y_c/H, and α are independent parameters.

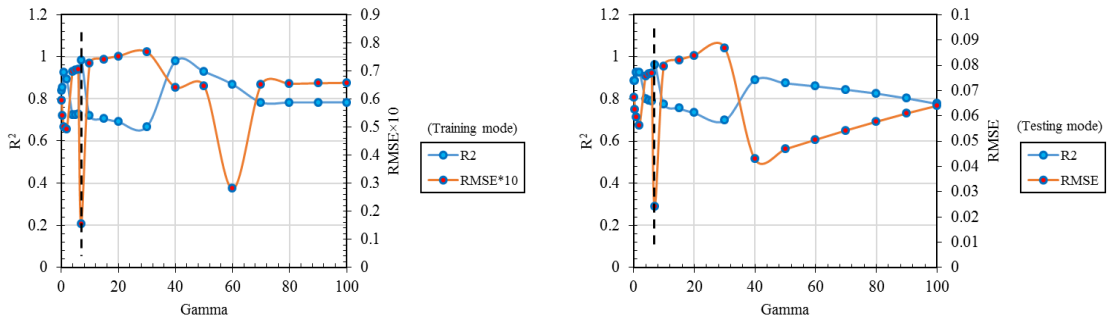
Table 3. Different input combinations in K-NN and SVM algorithms in the present study

Model no.	Input parameters	Model no.	Input parameters
First and second scenario: $\Delta E/E_0$ and y_d/H			
Model 1	α	Model 8	Fr_0, y_C/H
Model 2	a/b	Model 9	y_C/H, a/b, α
Model 3	Fr_0	Model 10	Fr_0, a/b, α
Model 4	y_C/H	Model 11	Fr_0, y_C/H, a/b
Model 5	y_C/H, α	Model 12	Fr_0, y_C/H, α
Model 6	Fr_0, α	Model 13	Fr_0, y_C/H, a/b, α
Model 7	Fr_0, a/b		

3.1. Results obtained from the SVM method

Three kernel functions, Radial Basic Function (RBF), Linear, and Polynomial, have been used in the SVM method for both scenarios. Each of the combinations presented in Table 3 is entered into the machine and the results of the best model are presented in Table 4. By analyzing the data, it was determined that the model that includes all the input parameters (model 13) has the best answer, the highest values of R^2 and KGE and the lowest value of RMSE. The value of RMSE motivates selection of this as the best model. Also, the RBF kernel function yields the best results among other kernel functions and the best model is related to the output of the RBF kernel function.

The results of the SVM method show that for the first and second scenarios, combination number 13 with inputs Fr_0, y_C/H, a/b and α has the lowest error (RMSE=0.0156), the highest correlation coefficient (R^2=0.984), and the highest Kling-Gupta coefficient (KGE= 0.961) for the first-scenario training mode. The corresponding values are RMSE= 0.0241, R^2= 0.962 and KGE= 0.952 for the first scenario testing mode. For the second scenario, the training mode has values of RMSE= 0.0212, R^2= 0.973, and KGE = 0.916; values from the testing mode are: RMSE= 0.0291, R^2= 0.971, and KGE= 0.939 and with an evaluation percentage of 75-25%. Values γ=7 and γ=10 are used, respectively for the first and second scenario (Figure 5).



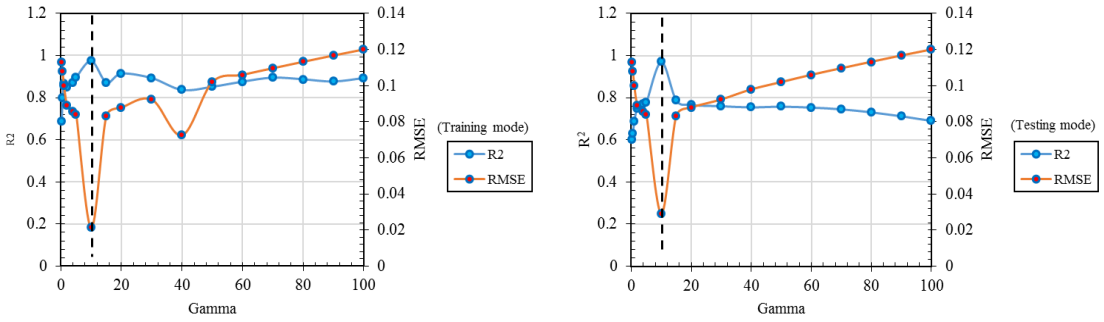
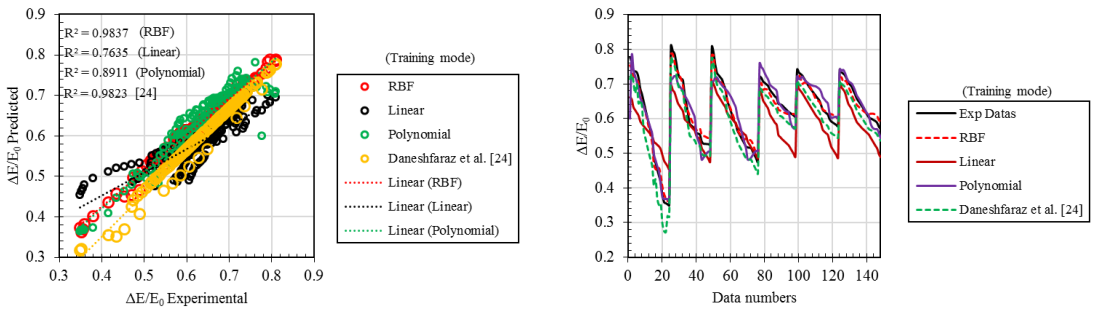


Figure 5. R^2 and RMSE Vs. γvalues for the SVM algorithm for RBF: a, b) First scenario c, d) Second scenario

Table 4. Evaluation parameters of the best combination for scenario 1 and 2 for all SVM kernels

Kernel type	Training mode			Testing mode				
	Best combination: Combination of number 13 (in table 3)							
	RMSE	R^2	KGE	RMSE	R^2	KGE	γ	Scenario
RBF	0.0156	0.984	0.961	0.0241	0.962	0.952	7	First: $\Delta E/E_0$
Linear	0.0676	0.873	0.852	0.08	0.836	0.842	---	
Polynomial	0.0888	0.956	0.946	0.0938	0.945	0.955	1	
RBF	0.0212	0.973	0.916	0.0291	0.971	0.0939	10	Second: y_d/H
Linear	0.0689	0.818	0.871	0.0817	0.761	0.859	---	
Polynomial	0.109	0.581	0.549	0.112	0.551	0.485	10	

Figures (6a, c, e, g) show the distribution curves of the predicted data for the best combination of hydraulic parameters (combination no. 13) for the first and second scenarios for both the training and testing modes. These data have less dispersion than other kernel functions and are placed on a bisector. Also, Figures (6-b, d, f, h) compare the experimental and predicted data of the superior model and show a good correlation in these two scenarios for the distribution of the RBF kernel with respect to the linear and polynomial functions. On the other hand, Comparing the data of this research with the data of research [24] for different methods of SVM algorithm shows that they match very well. So that the data of research [24] with the present research has R^2 parameter equal to 0.9823 and 0.9752 for the training and testing mode, respectively in the parameter of relative energy dissipation, and for the relative depth of downstream parameter R^2 is equal to 0.9958 and 0.982 for the training and testing mode, respectively.



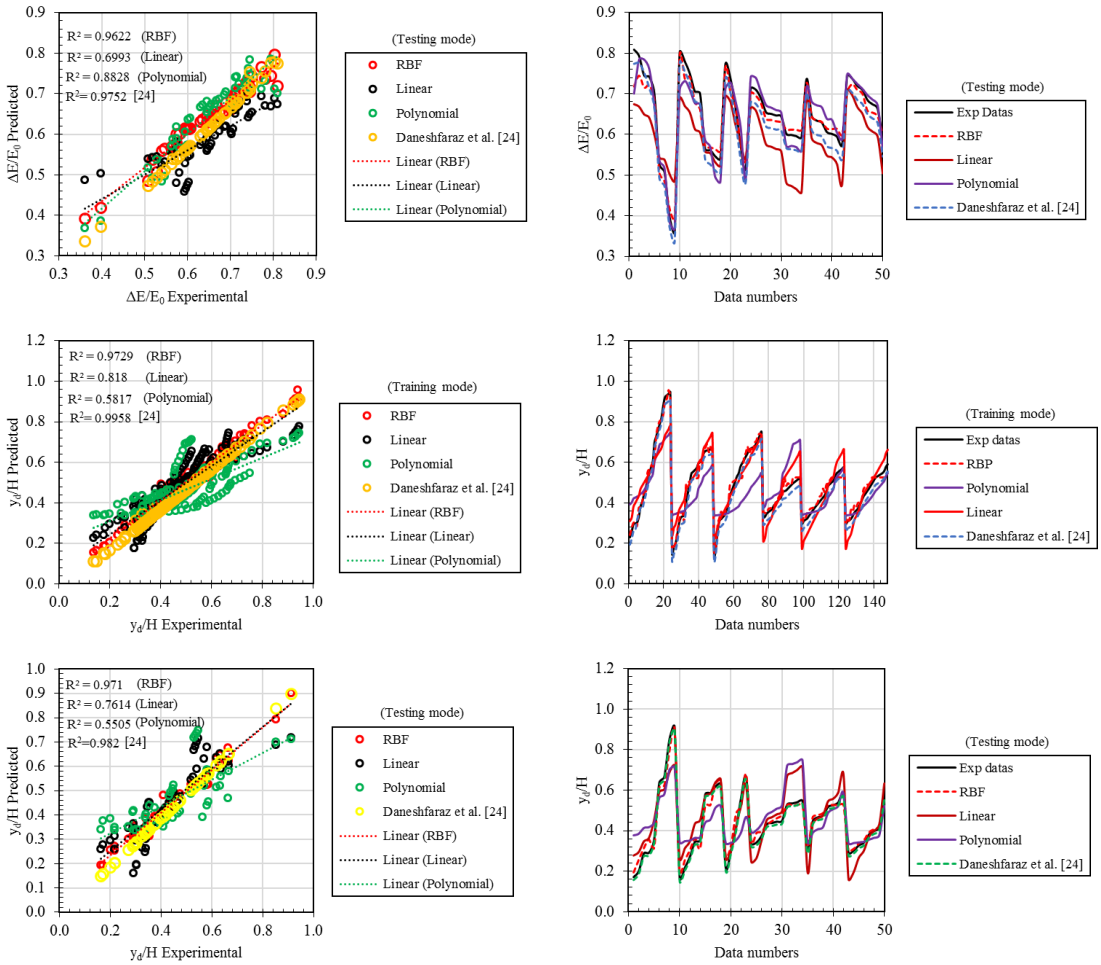


Figure 6. a, c, e, g) Distribution curve of experimental and predicted data in the training and testing modes for the best model (a, c: first scenario; e, g: second scenario)
b, d, f, h) Comparison of experimental and predicted data in the training and testing modes for the best model in the SVM algorithm (b, d: first scenario; f, h: second scenario)

3.2. K-NN Results

The K-NN pattern method is a machine learning method that is classified as a non-stationary statistical method used for regression and classification. The distance criterion for continuous variables in this algorithm is usually the Euclidean distance. Euclidean distance is the distance between two points which is obtained by using the Pythagorean theory. In the K-NN algorithm, there are three methods for distance measurement, which are Euclidean, Cityblock (Manhattan) and Chebychev methods. As with the earlier SVM results, statistical metrics for K-NN are listed in Table 3 are entered in order and the results of the best models are provided in Table 5. It was determined that combination 13, which includes all the input parameters, has the best response and has thus been selected as the best model. The working method of this algorithm is such that after selecting the distance measurement methods, a percentage is selected for the initial sample size, the number of neighbors is determined, and the correct setting of this value for the number of neighbors helps to improve the results as much as possible.

Table 5. Results of evaluation parameters of the best combination for scenario 1 and 2 for K-NN algorithm

Distance measure	RMSE	R^2	KGE	Number of Nearest Neighbors	Scenario	Size of prototype sample
	Best combination: Combination of number 13 (in table 3)					
Euclidean	0.0123	0.984	0.966	12	First: $\Delta E/E_0$	75%
Cityblock	0.0121	0.986	0.975			
Chebychev	0.0157	0.980	0.968			
Euclidean	0.0225	0.985	0.956	12	Second: y_d/H	75%
Cityblock	0.0123	0.986	0.967			
Chebychev	0.0157	0.980	0.973			

Up to a total of 100 neighbors were examined. It is clear in Figure 7 that for all distance measurement methods, 12 neighbors have been chosen as the optimal number of neighbors. Figures (7a and b) shows the changes of RMSE and R^2 against the number of nearest neighbors for the first scenario and Figures (7c and d) show the parameters for the second scenario. The expression indicates that 12 neighbors is optimal.

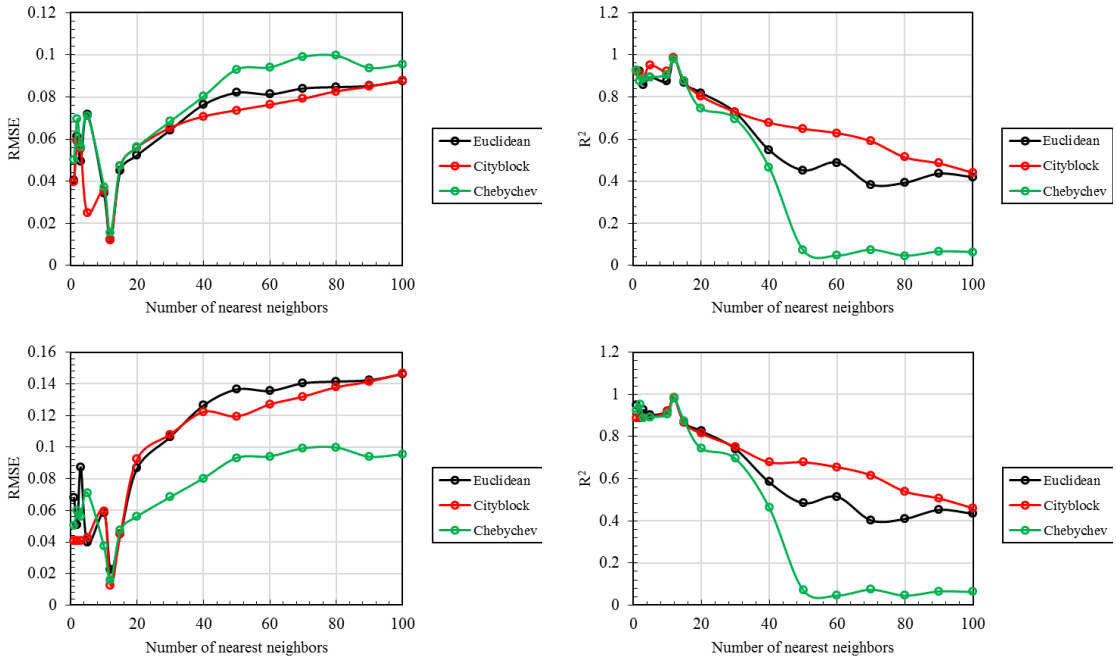


Figure 7. R^2 and RMSE Vs. number of nearest neighbors in K-NN algorithm: a, b) First scenario c, d) Second scenario

The results of the K-NN method shows that in the first and second scenarios, combination number 13 with inputs Fr_0, y_C/H, a/b and α yields RMSE = 0.0123, the highest R^2 (R^2= 0.984), and the highest Kling-Gupta coefficient (KGE= 0.966) for the Euclidean method; RMSE= 0.0121, R^2= 0.986 and KGE= 0.975 for the Cityblock method; and RMSE= 0.0157, R^2= 0.980 and KGE=

0.968 for the Chebychev method in the first scenario. For the second scenario, RMSE= 0.0225, R^2= 0.985 and KGE= 0.956 for the Euclidean method, RMSE= 0.0123, R^2 = 0.985 and KGE = 0.967 for the Cityblock method, and RMSE= 0.0157, R^2= 0.980 and KGE= 0.973 for the Chebychev method.

Figures (8a and c) show the distribution curves of the experimentally predicted data of the best combination of hydraulic parameters (combination no. 13) in the first and second scenarios using 75% of the data. The data related to this combination in the K-NN algorithm and in all three methods for distance measurement have less dispersion than the SVM kernel functions and all these methods are placed on the same median. Also, Figures (8-b and d) compare the experimental and predicted data of the superior model and show a good correlation in these two scenarios for Euclidean, Cityblock and Chebychev methods. It can be seen in these figures that the K-NN algorithm provides better results compared to those obtained from the SVM algorithm. On the other hand, with a more detailed investigation, it can be seen that by increasing the number of nearest neighbors, unfavorable results are obtained.

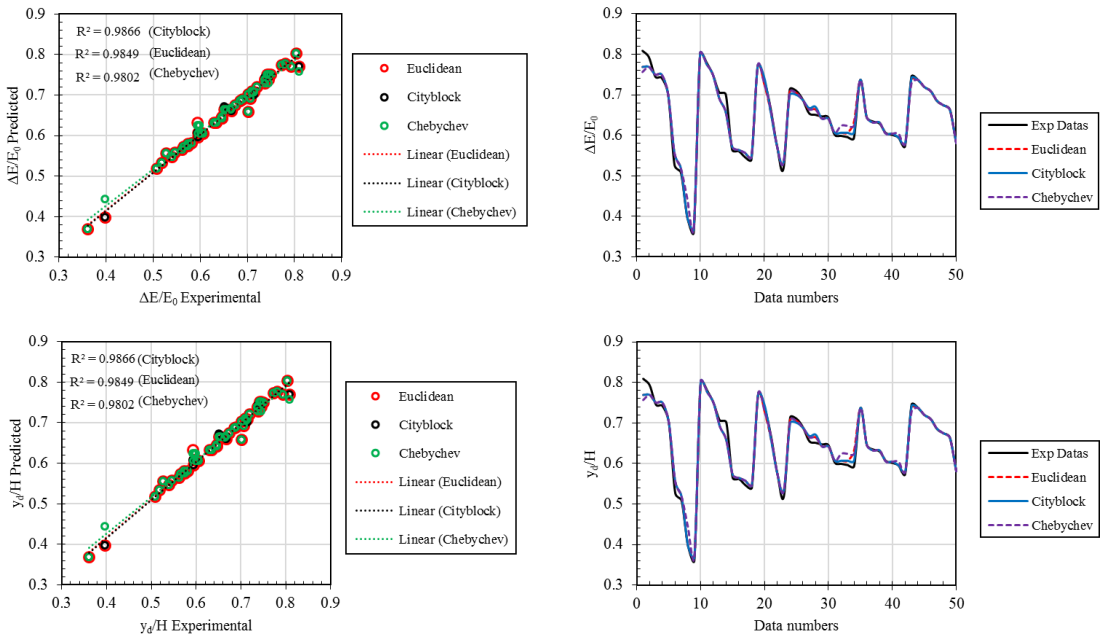


Figure 8. a, c) Distribution curves of experimental and predicted results for the best model in the K-NN algorithm (a: first scenario; c: second scenario)
(b, d, f, h) Comparison of experimental and predicted data for the best model in the K-NN algorithm (b: first scenario; d: second scenario)

Figure 9 shows the violin plot of the basic distribution of the data. From this figure, it can be concluded that the best SVM match of the evaluated data with the experimental data is related to the RBF kernel function, but the best match of the data occurs with the K-NN algorithm. Among the distance measurement methods in the K-NN method, all three methods have more accuracy and better results and compared to each other. Compared to the SVM algorithm, the results of the K-NN method are in good agreement with the experimental data.

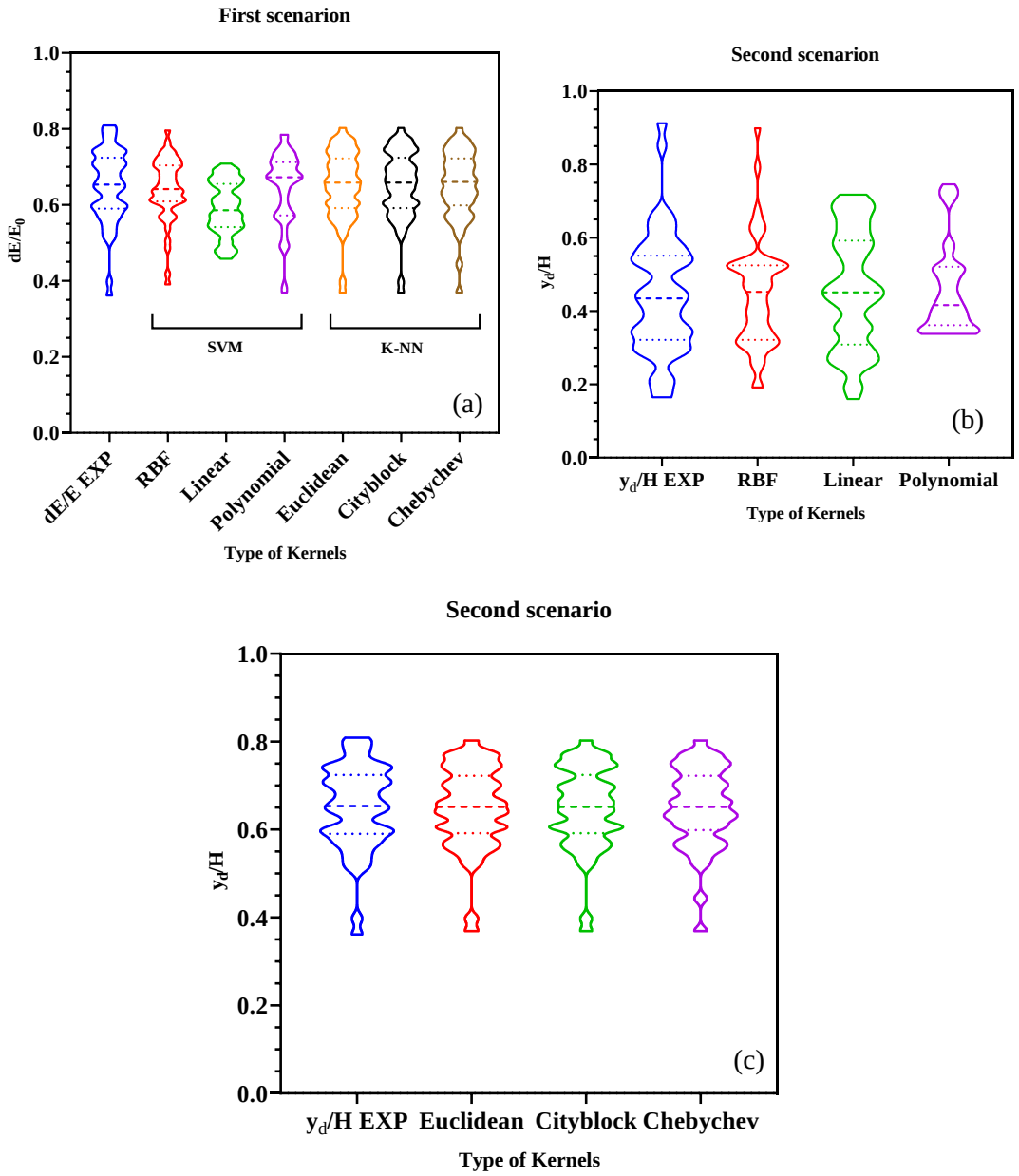


Figure 9. Violin plot for predicted and experimental data: a) First scenario, b) Second scenario, in SVM c) Second scenario in K-NN

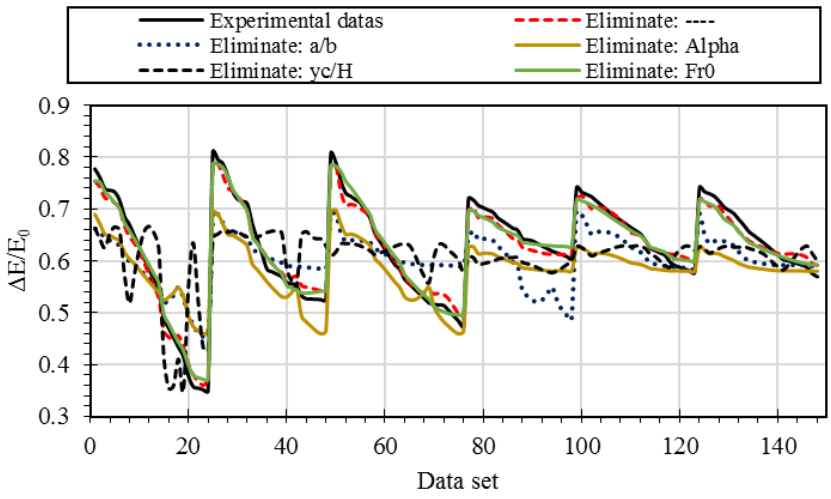
3.3. Sensitivity Analysis

Sensitivity analysis examines the important of the input variables of a statistical model at affecting the output results. By removing the input parameters one by one in both scenarios, and by using dimensional analysis, the parameter that had the most impact in predicting the relative energy dissipation and the relative depth of the downstream can be identified. Results of this sensitivity analysis are listed in Table 6.

÷

Input parameters	Eliminate parameter	Training		Testing	
		R^2	RMSE	R^2	RMSE
First scenario ($\Delta E/E_0$)					
Fr_0, y_C/H, a/b, α	----	0.984	0.0156	0.962	0.0241
Fr_0, y_C/H, α	a/b	0.656	0.0676	0.568	0.0806
Fr_0, y_C/H, a/b	α	0.846	0.0673	0.892	0.0739
Fr_0, a/b, α	y_C/H	0.281	0. 1039	0.0963	0.1024
y_C/H, a/b, α	Fr_0	0.985	0.0138	0.966	0.02
Second scenario (y_d/H)					
Fr_0, y_C/H, a/b, α	----	0.0156	0.984	0.0241	0.962
Fr_0, y_C/H, α	a/b	0.073	0.802	0.0832	0.605
Fr_0, y_C/H, a/b	α	0.0502	0.905	0.0478	0.912
Fr_0, a/b, α	y_C/H	0.138	0.267	0.154	0.127
y_C/H, a/b, α	Fr_0	0.0302	0.966	0.0328	0.959

Based on the sensitivity analysis carried out in the present research, it was found that for both the first and second scenarios, the independent parameter of the relative critical depth (y_c/H) has the greatest effect on the relative energy dissipation and the relative depth of the downstream according to Table 5 and Figure 10. According to Figure 10, in both scenarios, it is clear that the models in which the relative critical depth parameter is removed from the input parameters have a very bad match with the experimental data.



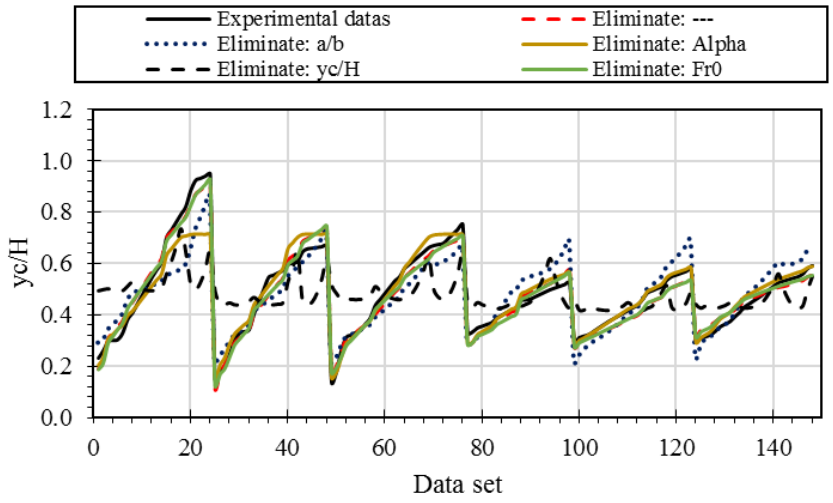
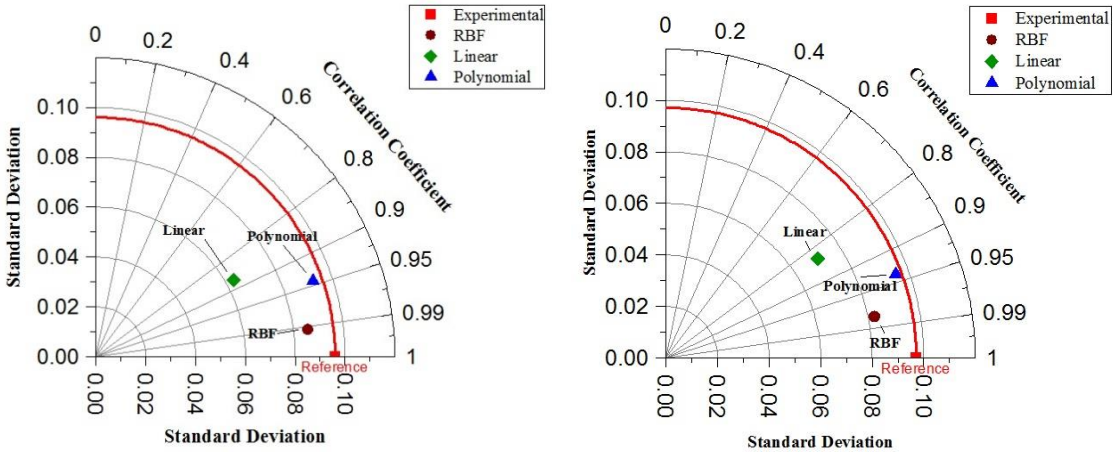


Figure 10. Comparison of laboratory data with results evaluated in sensitivity analysis: a) Relative energy dissipation, b) Relative downstream depth

In order to analyze and evaluate the models used in this research, according to Figure 11, Taylor diagram was used. As shown in Figure 11, one of the advantages of the Taylor diagram is that it uses two statistical indicators, correlation coefficient and standard deviation. Based on the Taylor diagram, the closer the predicted value is to the observed value in terms of correlation coefficient and standard deviation, the better the assessment and prediction has been made. The Taylor diagram in Figure 11 shows that the performance of the K-NN algorithm in all the investigated models, which includes models Eucliden, Chebichev, and Cityblock, has the highest performance and efficiency compared to the SVM model. Because the predicted standard deviation has the closest distance to the standard deviation of the observed data and shows the highest correlation coefficient. Based on all evaluation criteria, it can be stated that the models investigated in the present research have a good performance in estimating the parameters of relative energy dissipation and relative depth downstream. But among the reviewed models, the K-NN algorithm is more accurate than the SVM algorithm. Of course, this point should also be kept in mind that in the SVM algorithm, the linear model is the most consistent in observational data with prediction.



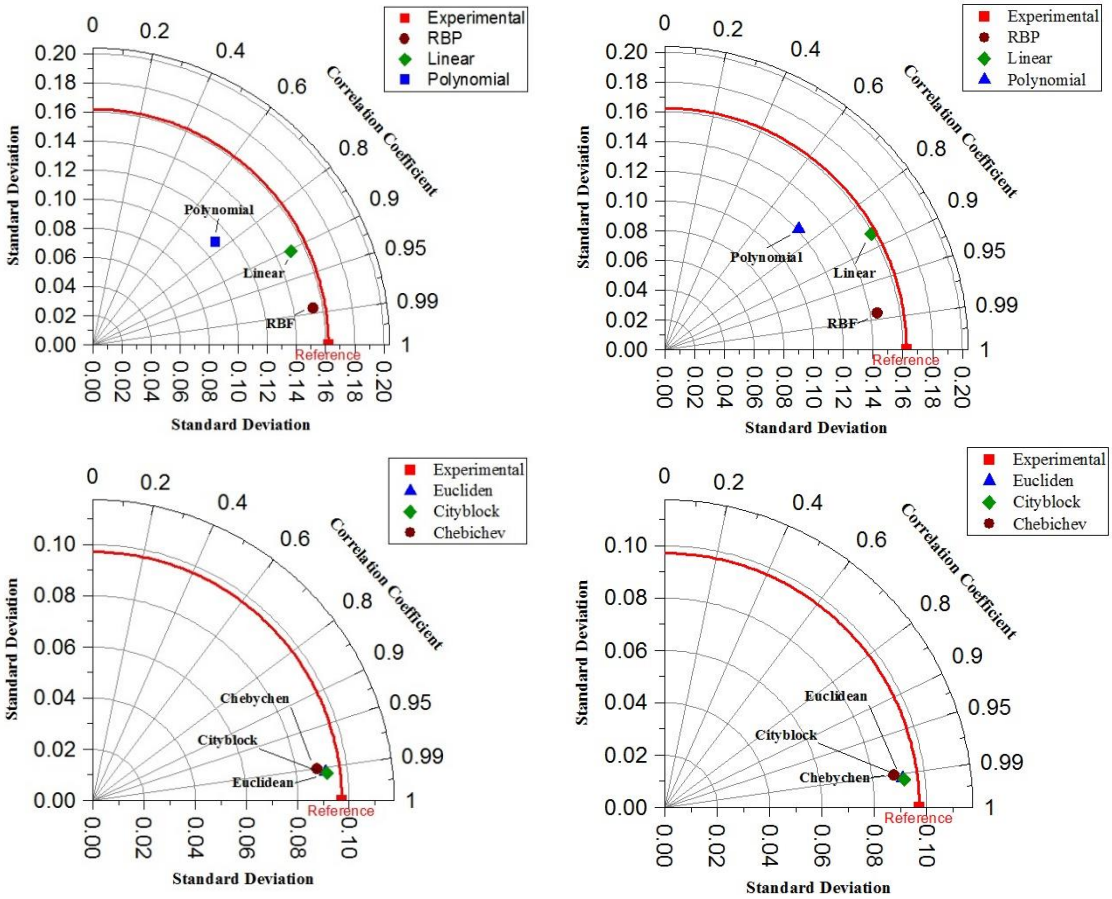


Figure 11. Taylor diagram in the investigated models of present research

4. Conclusion

In the present study, the parameters of relative energy dissipation and relative downstream depth in an inclined drop equipped with fishway elements have been evaluated using K-NN and SVM algorithms. A total of 395 data points with the same experimental conditions were used. It was shown that the prediction of these two parameters in both scenarios, a combination that included all independent input parameters, provided the best combination. In both scenarios, combination number 13 with independent input parameters Fr_0, y_C/H, a/b and α was superior and its results are as follows:

In the SVM algorithm, the Radial Basic Function (RBF) kernel type provides the best result among the kernel functions investigated in this research. In the K-NN algorithm, the Euclidean, Cityblock and Chebychev distance measurement methods have provided results that are in good agreement with the experimental data. The first scenario ($\Delta E/E_0$), in the SVM algorithm results were quantified with R^2, RMSE and KGE evaluation values equal to 0.984, 0.0156 and 0.961 respectively for the training mode and 0.962, 0.0248 and 0.952 for testing mode.

The second scenario (y_d/H), in the SVM algorithm resulted in R^2, RMSE and KGE values equal to 0.973, 0.0212, and 0.916, respectively, for training mode and 0.971 and 0.0291 and 0.931 for the testing mode and RBF kernel function. In the first and second scenarios with the

K-NN algorithm, the evaluation values in all three distance measurement methods are in the range of $0.98 \leq R^2 \leq 0.986$, $0.0123 \leq$ RMSE ≤ 0.0225 and $0.956 \leq$ KGE ≤ 0.973. By examining the results, it was found that the K-NN algorithm provides better results compared to the SVM algorithm.

The sensitivity analysis showed that the relative critical depth parameter has the greatest effect in predicting energy dissipation and downstream relative depth. In the first scenario, by removing the desired parameter, the evaluation parameters RMSE and R^2 are respectively equal to 0.1039 and 0.281 in the training mode and 0.1024 and 0.0963 in the testing mode. For the second scenario these quantities are, respectively, equal to 0.267 and 0.138 in the training mode and 0.127 and 0.154 in the testing mode.

Notation

q: The flow rate per unit width
H: The height of the drop
θ: The angle of the drop with the horizon
y_u: The upstream depth of the drop
y_c: The critical depth
y_d: The downstream depth of the drop
μ: Dynamic viscosity
ρ: Density
g: The acceleration of gravity
α: The placement angle of the fishway elements,
a and b: The length and height of the opening of the elements,
x: The distance between the elements,
L_{air}: The length of the aeration,
L_j: The length of the hydraulic jump,
E_u: The upstream energy of the drop,
E_d: The specific energy downstream of the drop.

References

1. Zhang D, Qu Y, Shi X, Liu Y, Jiang, C, (2024). Design of a Novel Multislot and Pool‐Weir Combined Fishway Based on Hydraulic Properties Analysis and Fish-Passage Experiments. Journal of Hydraulic Engineering, 150(3), 04024004.
2. Zhong Z, Ruan T, Hu Y, Liu J, Liu B, Xu, W, (2021). Experimental and numerical assessment of hydraulic characteristic of a new semi-frustum weir in the pool-weir fishway. Ecological Engineering, 170, 106362.
3. Zheng T, Niu Z, Sun S, Shi J, Liu H, Li G, (2020). Comparative Study on the Hydraulic Characteristics of Nature-Like Fishways. Water, 12(4), 955.
4. Baki A.B.M, Azimi A.H, (2021). Hydraulics and design of fishways II: vertical-slot and rock-weir fishways. Journal of Ecohydraulics, 1-13.
5. Harris J.H, Peirson W.L, Mefford B, Kingsford R.T, Felder S, (2020). Laboratory testing of an innovative tube fishway concept. Journal of Ecohydraulics, 5(1), 84-93.
6. Cea L, Pena L, Puertas J, Vázquez-Cendón ME, Peña E, (2007). Application of several depth-averaged turbulence models to simulate flow in vertical slot fishways. Journal of Hydraulic Engineering, 133(2), 160-172.

7. Rodríguez TT, Agudo JP, Mosquera LP, González EP, (2006). Evaluating vertical-slot fishway designs in terms of fish swimming capabilities. Ecol. Eng, 27(1), 37–48.
8. Yagci O, (2010). Hydraulic aspects of pool-weir fishways as ecologically friendly structure, Elsevier, Ecological Engineering, 36(1), 36-46.
9. Ariffin J, Ghani AA, Zakaria NA, Yahya AS, (2004). Sediment prediction using ANN and regression approach. 1st International Conference on Managing Rivers in the 21st Century.
10. Alp M, Cigizoglu K, (2007). Suspended sediment load simulated by two artificial neural network methods using hydrometeorological data. Environmental Modeling and Software, 22(1), 2-13.
11. Goel A, Pal M, (2009). Application of support vector machines in scour prediction on grade-control structures. Engineering Applications of Artificial Intelligence, 22(2), 216-223.
12. Roushangar K, Valizadeh R, Ghasempour R, (2017). Estimation of hydraulic jumps characteristics of channels with sudden diverging side walls via SVM. Water Science and Technology, 76(7), 1614-1628.
13. Sadeghfam S, Daneshfaraz R, Khatibi R, Minaei O, (2019). Experimental studies on scour of supercritical flow jets in upstream of screens and modelling scouring dimensions using artificial intelligence to combine multiple models (AIMM). Journal of Hydroinformatics 21(5), 893-907.
14. Daneshfaraz R, Bagherzadeh M, Esmaeeli R, Norouzi R, Abraham J, (2021a). Study of the performance of support vector machine for predicting vertical drop hydraulic parameters in the presence of dual horizontal screens. Water supply 21(1), 217-231.
15. Fuentes-Pérez J.F, García-Vega A, Bravo-Córdoba F.J, Sanz-Ronda, F.J, (2021). A step to smart fishways: an autonomous obstruction detection system using hydraulic modeling and sensor networks. Sensors, 21(20), 6909.
16. Seifollahi M, Lotfollahi-Yaghin MA, Kalateh F, Daneshfaraz R, Abbasi S, Abraham J, (2021). Estimation of the local scour from a cylindrical bridge Pier using a compilation wavelet model and artificial neural network. Journal of Hydraulic Structures, 7(3), 1-22.
17. Daneshfaraz R, Aminvash E, Mirzaei R, Abraham J, (2021b). Predicting the energy dissipation of a rough sudden expansion rectangular stilling basins using the SVM algorithm. Journal of Applied Research in Water and Wastewater 8(2), 98-106.
18. Daneshfaraz R, Aminvash E, Ghaderi A, Abraham J, Bagherzadeh M, (2021c). SVM performance for predicting the effect of horizontal screen diameters on the hydraulic parameters of a vertical drop. Applied Sciences 11(9), 4238.
19. Kalathil S.T, Chandra V, (2023). Experimental and numerical investigation on the hydraulic design criteria for a step-pool nature-like fishway. Progress in Physical Geography: Earth and Environment, 47(6), 831-851.
20. Baharvand S, Lashkar-Ara B, (2023). Hydrodynamic and Biological Assessment of Modified Meander C-type Fishway to pass Rainbow Trout (Oncorhynchus mykiss) Fish Species. Scientia Iranica.
21. Mirkhorli P, Ghaderi A, Alizadeh Sanami F, Mohammadi M, Kuriqi A, Kisi O, (2024). An Investigation on Hydraulic Aspects of Rectangular Labyrinth Pool and Weir Fishway Using FLOW-3D. Arabian Journal for Science and Engineering, 1-27.
22. Baharvand S, Jozaghi A, Fatahi-Alkouhi R, Karimzadeh S, Nasiri R, Lashkar-Ara B, (2021). Comparative study on the machine learning and regression-based approaches to predict the hydraulic jump sequent depth ratio. Iranian Journal of Science and Technology, Transactions of Civil Engineering, 45(4), 2719-2732.

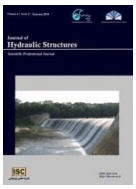
23. Cassan L, Miranda F.C, Laurens P, Courret D, (2023). Hydraulic of rock-ramp fishway with lateral slope. Environmental Fluid Mechanics, 23, 1-18.
24. Daneshfaraz R, Aminvash E, Bagherzadeh M, Ghaderi A, Kuriqi A, Najibi A, Ricardo A.M, (2021d). Laboratory investigation of hydraulic parameters on inclined drop equipped with fishway elements. Symmetry, 13(9),1643.



© 2024 by the authors. Licensee SCU, Ahvaz, Iran. This article is an open access article distributed under the terms and conditions of the Creative Commons Attribution 4.0 International (CC BY 4.0 license) (http://creativecommons.org/licenses/by/4.0/).



Journal of Hydraulic Structures
J. Hydraul. Struct., 2024;10(1):66-79
DOI: 10.22055/jhs.2024.46164.1289



OPEN ACCESS

Hydraulic Response to Geometry: Finite Element Modeling of Underground Spaces in Saturated Environments

Hadi Farhadian [*1]
Zahra Gholami [1]

Abstract

Tunneling operations face a significant challenge in managing water inflow into excavated underground spaces, primarily initial or excavating caused discontinuities in tunnel walls. The water flow rate is intricately linked to the geometric shape of the tunnel, making it a crucial consideration during infrastructure design and construction to mitigate the risks associated with water infiltration. This study employs the finite element numerical method to explore how different geometric shapes (circular, D-shaped, rectangular, and irregular hexagon tunnels), along with parameters like excavated space area, excavated space perimeter, water head, and permeability coefficient anisotropy, influence steady-state water inflow into tunnel as saturated environments. Results demonstrate that the geometric shape of underground spaces has a substantial impact on water ingress, with circular tunnels exhibiting notably lower inflow rates compared to other shapes under similar conditions. However, the overall dimensions of the simulation model may also influence the observed impact. The research underscores the necessity of considering both geometric shape and overall dimensions for effective drainage in tunnel design. While circular tunnels generally prove to be a safe choice, further project-specific analysis may be warranted. It is crucial to acknowledge that accurately predicting the influence radius requires intricate numerical modeling or physical experiments accounting for all relevant factors, as the impact of shape is just one facet, with other design and geological factors playing equally crucial roles.

Keywords: Water Inflow, Tunnel, Numerical Modeling, Geometric Shape.

Received: 17 February 2024; Accepted: 02 April 2024

[*] E-mail: farhadian@birjand.ac.ir **(Corresponding Author)**
[1] Department of Mining Engineering, Faculty of Engineering, University of Birjand, Birjand, Iran

CC BY

1. Introduction

The utilization of underground spaces is becoming increasingly widespread and diverse. One prevalent type of underground space is tunnels, constructed for various purposes. Among the primary challenges encountered in tunnel excavation is the infiltration of water into the tunnels. Issues arising from water leakage into the tunnel environment include a decrease in the stability of the surrounding rock mass, the imposition of excess pressure on both permanent and temporary support systems, and detrimental effects on the geomechanical condition of the rock, subsequently posing potential hazards to both life and finances [1-4].

One crucial factor influencing the water flow rate is the geometric shape of the tunnel. Considering the tunnel shape during the design and construction of infrastructure is essential for minimizing the risk of water infiltration and associated damages. Despite previous studies, limited attention has been given to the examination of this factor. Notable among these studies is the investigation of the impact of tunnel geometry on water leakage, exemplified by the study conducted on the Dorud-Khorramabad railway tunnel using analytical and numerical methods for estimation [5].

Due to the inherent difficulty in identifying and precisely determining all factors affecting water flow into the tunnel, especially during the excavation process, accurate prediction of water infiltration into the drilled tunnels within the rock environment is challenging. Various analytical methods and equations, based on simplifications and practical assumptions, are widely employed for calculating the water leakage into tunnels [6,7].

In addition to analytical methods providing a general estimate of leakage, considering the fundamental equations governing leakage flow and site-specific characteristics, numerical methods such as finite element, finite difference, discrete element, or finite volume approaches can be employed. Through the utilization of numerical methods, the flow of groundwater leakage into the tunnel environment can be simulated. Then, the leakage values into the tunnel can be computed in different regions of the construction site. Unlike analytical methods, numerical methods are not computationally simple, and they require comprehensive information about the construction site. They are also less reliant on simplifications and assumptions. As a result, numerical methods are more complex and time-consuming to implement, but they yield more accurate results compared to analytical methods [8,9].

The shape of the tunnel is a significant factor affecting the amount of water inflow. The geometry of the tunnel influences the flow patterns and pressure distribution within the tunnel, which in turn affects the rate of water seepage [10].

Several factors related to tunnel shape can influence water inflow, including:

Cross-sectional shape: The cross-sectional shape of the tunnel, such as circular, rectangular, or horseshoe-shaped, can affect the flow velocity and pressure distribution within the tunnel.

Tunnel size: The size of the tunnel, such as its diameter or width and height, can influence the amount of water that can be stored within the tunnel and the rate of water flow.

Tunnel alignment: The alignment of the tunnel, such as its slope and curvature, can affect the direction of water flow and the potential for water to accumulate in certain areas of the tunnel. In other words, the shape and alignment of the tunnel affect the velocity and turbulence of the flowing water. Sudden changes in direction or steep slopes can lead to turbulence, eddies, and areas of low pressure where water may settle. Also, the alignment of the tunnel entrance and exit points also influences water flow. If these points are not well-designed, water can accumulate during heavy rainfall or in situations of high water flow, leading to potential flooding.

The geometry of a tunnel significantly influences water pressure conditions, hydraulic boundary conditions, and flow of seepage. Research indicates that different tunnel shapes can lead to various water flows, where factors such as water velocity and pressure are influenced by tunnel dimensions. Furthermore, the distance from the tunnel excavation surface to geological features, such as faults, can also impact the rate of water ingress. Consequently, the shape of a tunnel plays a crucial role in determining the characteristics of seepage and the magnitude of water flow, making it a focal point in underground construction projects and water management [11-14].
Advantages of circular tunnels regarding water ingress include the following aspects:

1. Uniform Stress Distribution: Circular tunnels distribute loads more uniformly, reducing the risk of stress concentration and potential failure compared to other shapes, such as square tunnels [15].
2. Analytical Solutions: Analytical solutions exist for estimating water ingress into circular tunnels, aiding in tunnel design, construction, and environmental impact assessment [16].
3. Leakage Prevention Effect: Research has demonstrated that the leakage prevention effect of flow by injection can be assessable in circular tunnels, making it significant for water flow management [17].

However, explicitly mentioned disadvantages of circular tunnels in terms of water ingress have not been reported in the conducted studies. Nevertheless, it is essential to note that the design, construction, and maintenance of tunnels can be costly, and there may be specific constraints based on geological and hydrogeological conditions. In this article, an attempt has been made to study the impact of the geometric model of underground spaces on the steady-state groundwater inflow using finite element modeling.

2. Finite Element Method in Solving the Groundwater Inflow Equation to Tunnels:

The Seep/w software is a versatile and comprehensive computer program capable of providing analyses in dynamic and static domains. It employs the finite element method for analyzing and modeling water flow. In essence, this software is a numerical model with the ability to simulate the mathematical representation of the actual physical process of water flow in a porous medium. Seep/w, as part of the GeoStudio software suite, has the capability to analyze various flow conditions, including saturated or unsaturated flows in confined or unconfined aquifers in two-dimensional settings, assuming that hydraulic conductivity and water content are functions of the pore-water pressure [18, 19].

The fundamental equation of groundwater flow in two dimensions, considering both saturated and unsaturated flow conditions, is derived by combining Darcy's law and the continuity equation:

$$\frac{\partial}{\partial x}\left(K_x \frac{\partial h}{\partial y}\right)+\frac{\partial}{\partial y}\left(K_y \frac{\partial h}{\partial y}\right)=C\,\frac{\partial}{\partial t}(h)+Q \qquad (1)$$

In this equation:

Kx and Ky are the coefficients of permeability in the x and y directions, h is the hydraulic head, t is time, x and y are Cartesian coordinates, C is the slope of the moisture characteristic curve, and Q is a flow source such as pumping or recharge.

The hydraulic head (h) is related to the volumetric water content (θ) through the relationship:

$$\frac{\partial \theta}{\partial t} = C \frac{\partial h}{\partial t} \quad (2)$$

In Seep/w, the Galerkin approximation method is used for solving the groundwater flow equation in two dimensions. This method, with appropriate consideration of boundary conditions, provides an approximate solution for the equation. The groundwater flow equation (3) can be written in the following form within the software:

$$L(h) = \frac{\partial}{\partial x}\left(K_x \frac{\partial h}{\partial x}\right) + \frac{\partial}{\partial y}\left(K_y \frac{\partial h}{\partial y}\right) - C \frac{\partial}{\partial t}(h) - Q = 0 \quad (3)$$

The Seep/w software is a valuable tool for modeling and solving various hydrological, hydrogeological, geotechnical, and mining problems. It can be utilized for modeling tunnels with different geometric cross-sections, representing different geological layers with distinct hydraulic properties, and simulating continuous environments. However, it has limitations, such as the inability to model discontinuous environments where water flow is a function of fractures within the rock mass [20,21].

3. The Geometric Shape Effect on Groundwater Inflow into Underground Spaces:

In this study, the finite element software Seep/W was employed to investigate the impact of the geometric shape of underground spaces on groundwater inflow. A two-dimensional numerical model was used to explore variations in several geometric parameters of underground spaces, including the shape of the underground space such as circle, D-shape (combination of a rectangle and a half-circle), irregular hexagon, and rectangle, the area of the underground space (S), the perimeter of the underground space (P), the anisotropic permeability ratio (Ky/kx), and the groundwater table level (H). Two geometric dimensions of the model (domain model) were simulated, measuring 50 by 30 square meters and 100 by 60 square meters. Figure 1 illustrates the schematic geometric model of numerical simulations along with the utilized parameters.

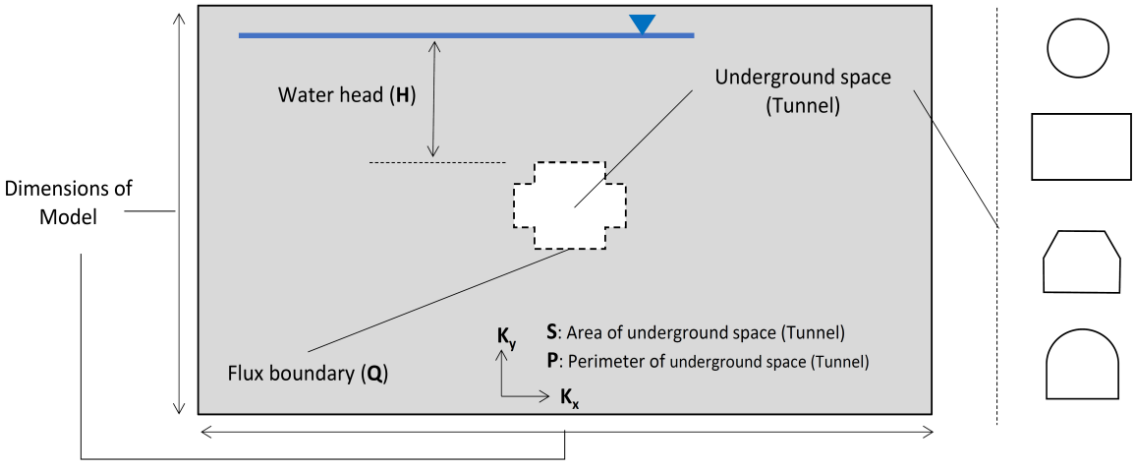


Figure 1: Schematic Geometric Model and Parameters Utilized in Numerical Simulation.

The simulations utilized boundary conditions as follows: constant head at the lateral boundaries on the right and left sides, flow boundary around the tunnel, and a no-flow boundary at the model's base. The modeling and numerical analysis procedure can be outlined as follows:

1. Geometric modeling of the domain and delineation of tunnel.
2. Application of material properties (permeability coefficient).
3. Application of appropriate boundary conditions (as mentioned above) and meshing the model for two-dimensional finite element analysis.

In the numerical analysis, the model domain, configured as a rectangular shape, underwent discretization into finite element meshes. Therefore, the type of square and triangular elements was chosen in the pattern of finite element mesh, and based on the dimensions of the model and its excavated underground spaces, for the 50 by 30 square meters model, the element number was set in the range of 326 to 469, while for the 100 by 60 square meters model, the element number was applied within the range of 342 to 499.

Figure 2 illustrates a sample of the numerical simulation of groundwater inflow into various underground spaces within a 30 square meter area. It is essential to note that the modeling was performed in a steady-state and two-dimensional configuration

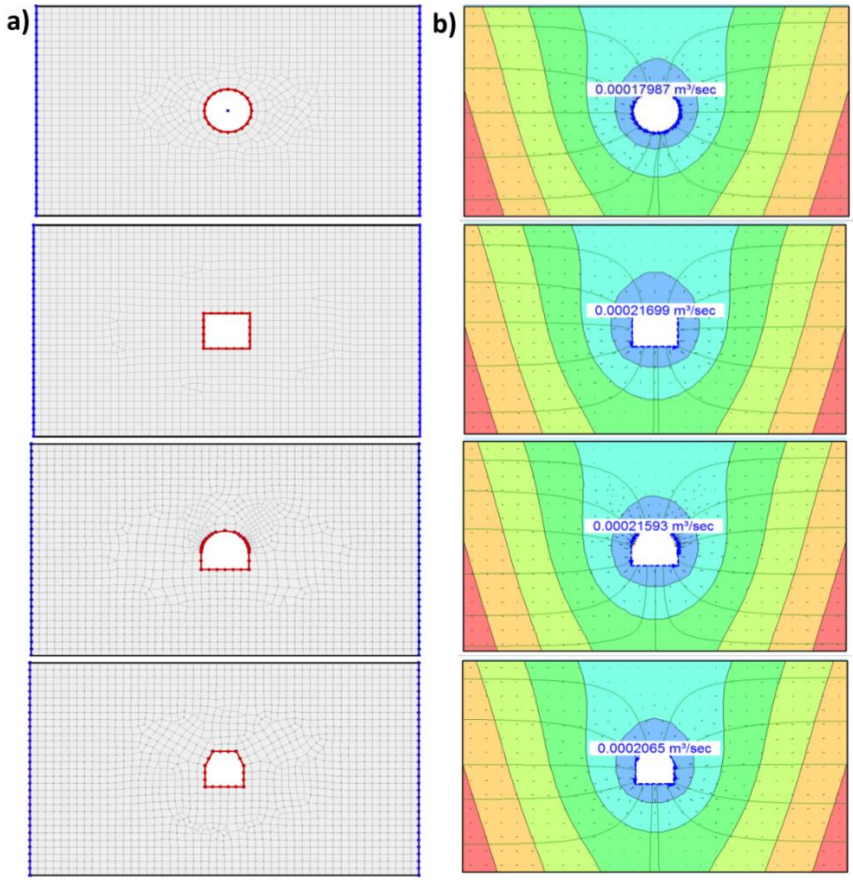


Figure 2: Simulation of various models of groundwater inflow into tunnels in spaces with an area of 30 square meters in dimensions of 50 by 30 square meters. (a) Illustration of the meshing approach and the Define state, (b) Simulated groundwater inflow into the tunnel in the Results state.

3.1 The Effect of Geometric Shape of Underground Space on the Groundwater Inflow Based on the Area of Excavated Space (S):

To investigate the influence of the geometric shape of underground spaces (circular, D-shaped, rectangular, and irregular hexagon) on groundwater inflow under various excavated space areas (5, 10, 20, 30, 40, and 50 square meters) and with different groundwater table levels relative to the center of the excavated space (20, 50, and 100 meters) in two model dimensions (50 by 30 and 100 by 60 square meters) at an anisotropic permeability ratio (ky/kx) of 1, a total of 144 different models were simulated. Figure 3 depicts the groundwater inflow into various spaces in the dimensions of 50 by 30 square meters and 100 by 60 square meters. As observed in these graphs, an increase in the area of the excavated space in different tunnel shapes results in an increased rate of groundwater inflow.

It is evident from these graphs that the circular-shaped tunnel generally exhibits the lowest rate of seepage compared to other shapes of underground spaces, such as D-shaped, rectangular, and irregular hexagon.

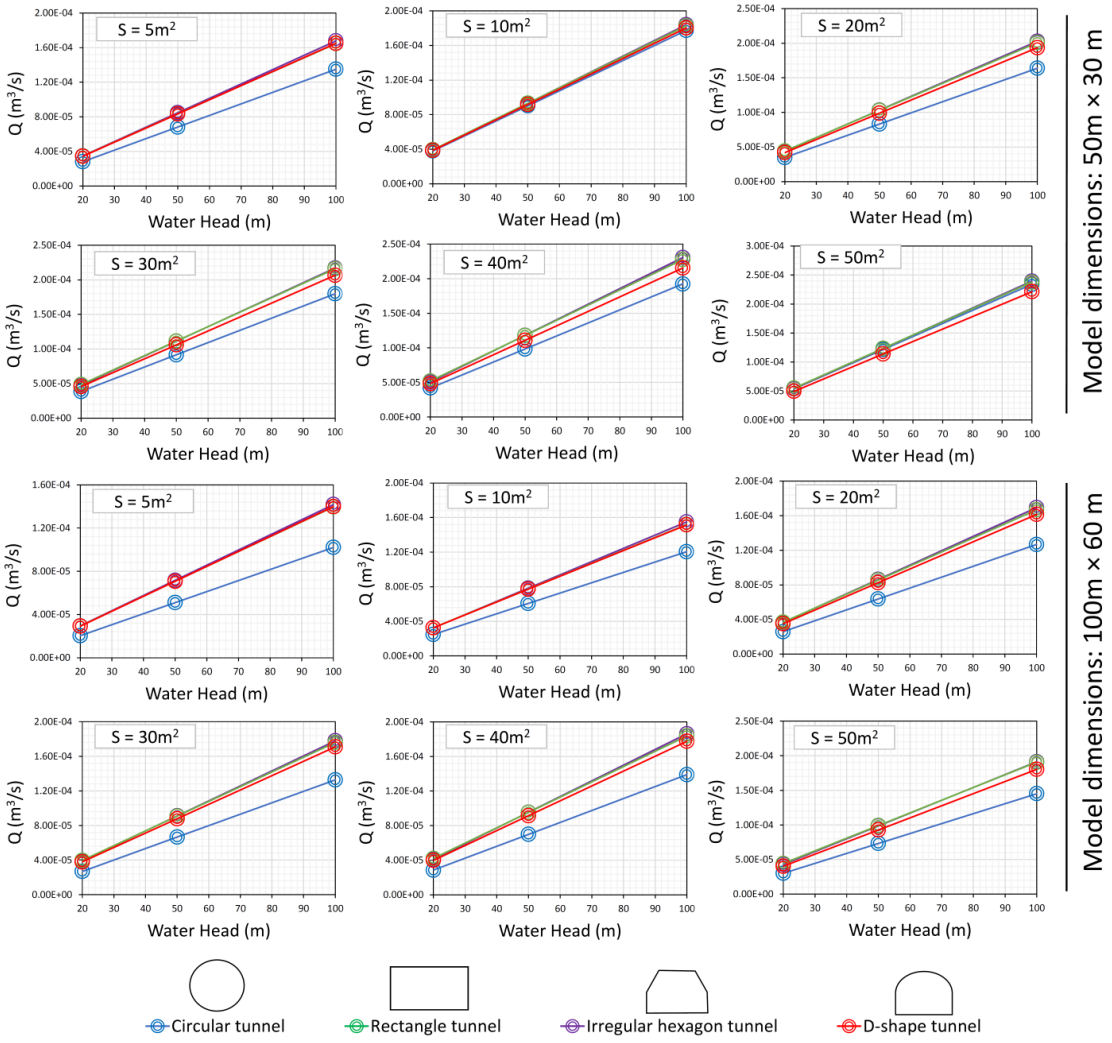


Figure 3: Groundwater inflow into the tunnel based on different geometric shapes of excavated spaces considering various areas and groundwater table levels in two different model dimensions.

3.2 The Effect of Geometric Shape of Underground Spaces on the Groundwater Inflow into the Tunnel Based on Excavated Space Perimeter (P):

To investigate the impact of the geometric shape of underground spaces (circular, D-shaped, rectangular, and irregular hexagon) on groundwater inflow under various excavated space perimeters (P: 5, 10, 20, 30, 40, and 50 square meters) and with different groundwater table levels relative to the ceiling of the excavated space (20, 50, and 100 meters) in two model dimensions (50 by 30 and 100 by 60 square meters) at an anisotropic permeability ratio (ky/kx) of 1, a total of 144 different models were simulated. Figure 4 illustrates the groundwater inflow into various spaces in the dimensions of 50 by 30 square meters and 100 by 60 square meters. As observed in these graphs, an increase in the excavated space perimeter in different tunnel shapes results in an increased rate of groundwater inflow. Although the difference is not significant in smaller areas, an increase in the area or spatial extent results in a more pronounced variation in the inflow of water into the tunnel. For instance, as illustrated in Fig. 6, concerning the model dimensions of 100 by 60 square meters at water head of 50 meter, the water inflow rate for the irregular hexagon tunnel in excavated areas of 5 and 10 square meters are 8.43e-5 m^3/sec and 9.17e-5 m^3/sec , respectively. In the excavated area of 50 square meters, the inflow rate reaches 1.14e-4 m^3/sec.

It is evident from these graphs that the circular-shaped tunnel generally exhibits the lowest rate of seepage compared to other shapes of underground spaces, such as D-shaped, rectangular, and irregular hexagon**.**

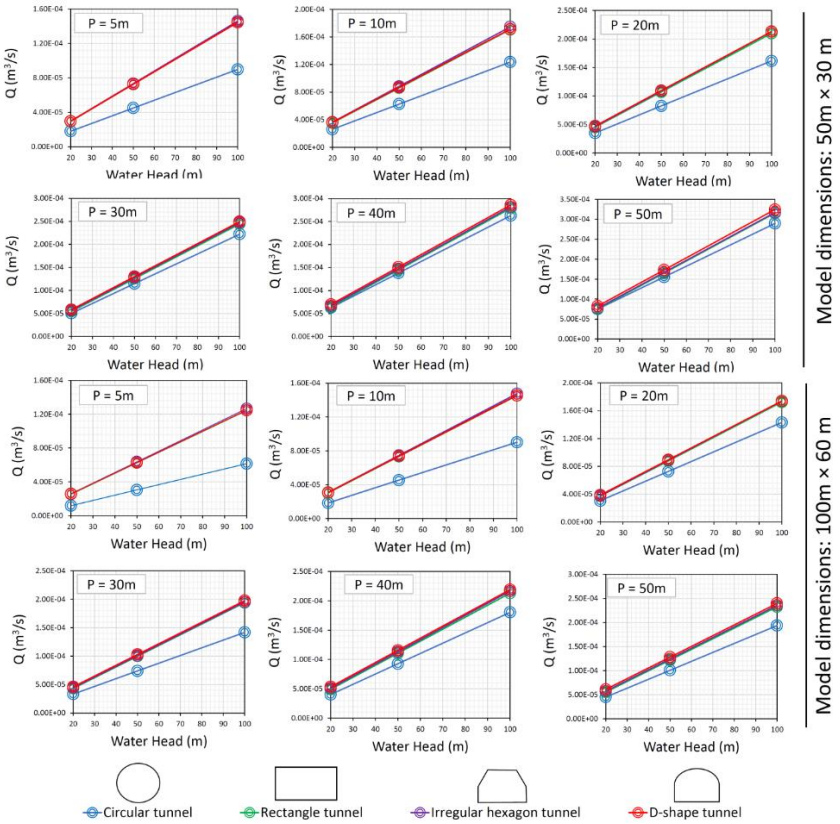


Figure 4: Groundwater inflow into the tunnel based on different geometric shapes of excavated spaces considering various perimeters and groundwater table levels in two different model dimensions.

3.3 The Effect of Geometric Shape of Underground Spaces on Water Inflow Based on Influence Radius:

The geometric shape of an underground space, specifically a tunnel, can indeed have a significant impact on the influence radius of water inflow. The circular tunnel shape offers a balanced influence radius due to its uniform perimeter. However, variations in hydraulic conductivity can still create uneven flow patterns. In the rectangular, wider bases can lead to larger influence zones, especially if water primarily enters from the bottom. However, corners can create complex flow patterns. In the D-shape tunnel, commonly used in soft ground, offers better stability. Its curved top and angled sides can influence water flow depending on the specific dimensions and orientation. Also, in the irregular tunnel, complex or non-standard shapes are harder to predict, requiring detailed analysis considering specific geometries and local hydrogeological conditions.

To investigate the impact of the geometric shape of underground spaces (circular, D-shaped, rectangular, and irregular hexagon) on influence radius as point of water inflow to tunnel view, various scenarios were examined under different excavated space areas, different excavated space perimeters and varying groundwater table levels relative to the ceiling of the excavated space (20, 50, and 100 meters). To examine the influence radius, for excavated areas (excavated perimeters) of 5, 10, 20, 30, 40, and 50 square meters (meters), the flux boundaries were set at 10, 20, 30, 40, 50, and 60 square meters (meters) from the center of the shape. The boundaries were set at 10, 20, 30, 40, 50, and 60 square meters (meters), respectively. Figure 5 illustrates the schematic geometric model of the numerical simulation along with the flux boundary.

The analysis was conducted using model dimensions of 100 by 60 square meters with an anisotropic permeability ratio (ky/kx) equal to 1, resulting in a total of 144 different simulation models. Figure 6 depicts the groundwater inflow into various spaces in the dimensions of 50 by 30 square meters and 100 by 60 square meters.

As depicted in these graphs, based on the mentioned flux boundaries (influence radiuses), with an increase in both the area and the perimeter of the excavated underground space in various tunnel shapes, the water inflow rate has significantly increased. Furthermore, the circular-shaped tunnel, when considering the impact of different geometric shapes based on the excavated area, generally exhibits the highest inflow rate within the influence radius, while the D-shaped tunnel demonstrates the lowest rate.

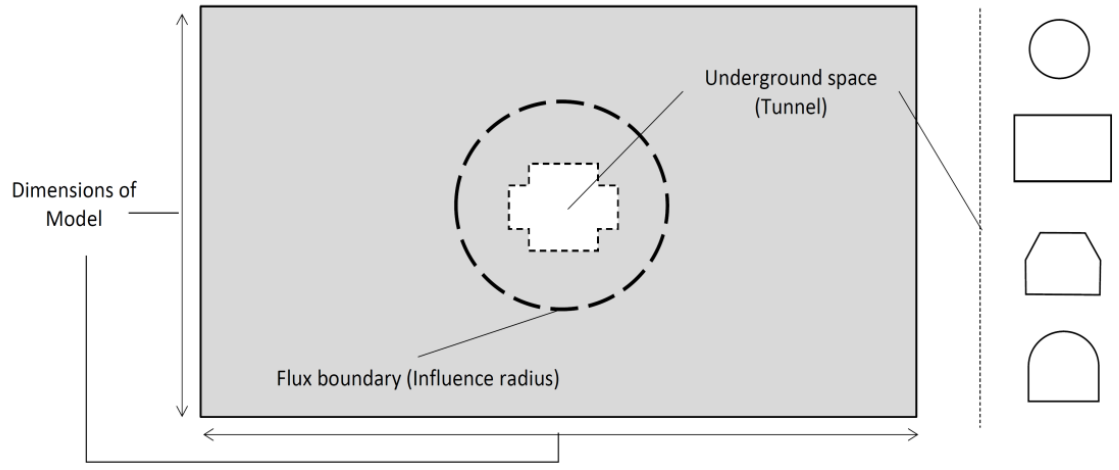


Figure 5: Schematic Geometric Model for Investigating the Influence Radius

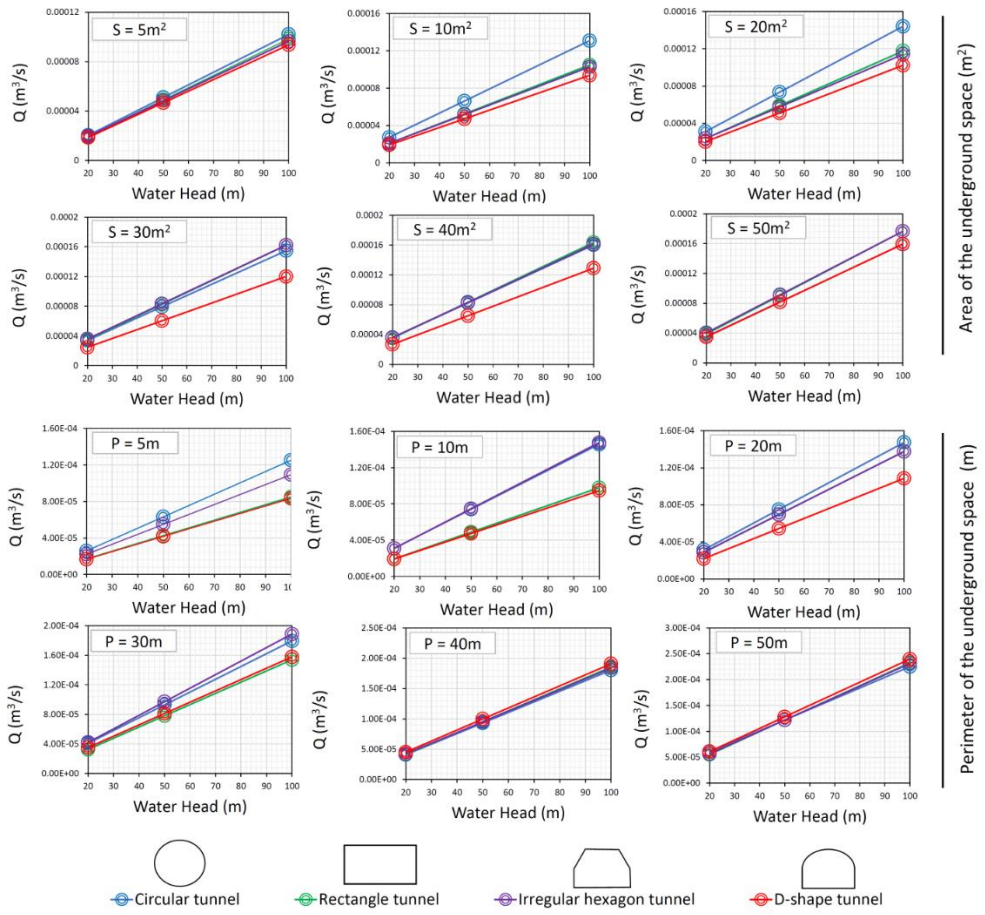


Figure 6: The Effect of Geometric Shape of Underground Spaces on water inflow based on influence radius

Regarding the effect of different geometric shapes based on the excavated perimeter, a specific trend could not be discerned. However, it can be concluded that circular-shaped tunnels, given their higher inflow rates compared to other geometric shapes, facilitate water discharge at a faster pace, especially within the influence radius.

3.4 The Influence of Geometric Shape of Underground Spaces on Water Inflow into Tunnels Considering Anisotropic Conditions of Permeability Coefficient:

To investigate the impact of the geometric shape of underground spaces (circular, D-shaped, rectangular, and irregular hexagon) on water inflow under various anisotropic conditions of permeability coefficient (the ratio of vertical permeability to horizontal permeability - Ky/Kx: 0.1, 0.5, and 1), scenarios were explored for excavated space areas of 20 square meters, and the dimensions of the excavated perimeters were 20 meters. Additionally, different groundwater table levels relative to the ceiling of the excavated space (20, 50, and 100 meters) were considered for various model dimensions, including 50 by 30 square meters and 100 by 60 square meters, resulting in a total of diverse simulation models. Figure 7 illustrates the water inflow into various spaces in the dimensions of 50 by 30 square meters and 100 by 60 square meters.

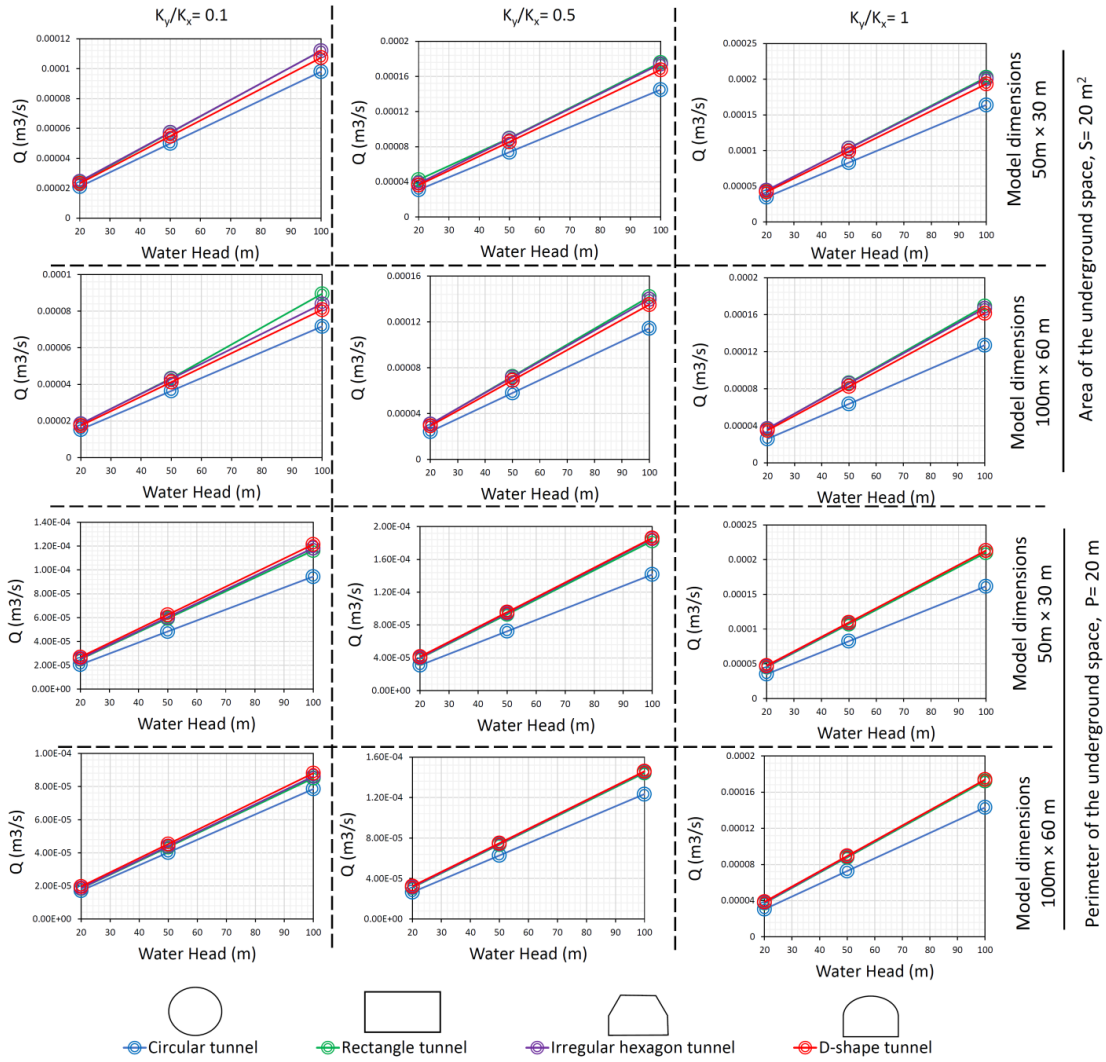


Figure 7: Influence of Geometric Shape of Underground Spaces on Water Inflow into Tunnels Considering Anisotropic Conditions of Permeability Coefficient

As observed in these diagrams, with an increase in both the area and the perimeter of the excavated underground space in various tunnel shapes, the water inflow rate has significantly increased. Notably, applying variations in the anisotropic conditions of the permeability coefficient (sensitivity analysis on Ky/Kx=0.1, 0.5, and 1) did not reveal significant changes in the trend of geometric shape influence on the water inflow into the tunnel. In the majority of simulated models, the water inflow into the circular tunnel exhibits the lowest rate both when considering the impact of the geometric shape based on the excavated area and when considering it based on the excavated perimeter.

4. Discussion:

The geometric shape of underground spaces can significantly influence the water inflow into tunnels. Sensitivity analysis on various parameters indicates that circular-shaped tunnels may be preferable for effective drainage. This preference arises from both having the lowest water inflow rates into the tunnel and the wide influence radius of such tunnels, as illustrated schematically in Figure 8. However, it is crucial to note that the overall dimensions of the geometric model also play a crucial role in the water inflow into the tunnel. The proximity of the model dimensions to the boundaries of the underground space intensifies the impact of boundary conditions on water inflow, leading to a non-linear prediction for water flow. For instance, in the model with dimensions of 50 by 30 meters and an underground space area of 50 square meters, the irregular hexagon-shaped tunnel exhibited the lowest flow rate compared to other shapes. Still, no specific trend can be generalized across various dimensions of the overall model. Conversely, in the model with dimensions of 100 by 60 meters based on the excavated area, a circular-shaped tunnel demonstrated the lowest flow rate, while a rectangular-shaped tunnel exhibited the highest flow rate. This observation extends to different sizes of excavated perimeters, indicating that, for instance, in various excavated area sizes, circular-shaped tunnels generally have the lowest flow rates, while D-shaped tunnels exhibit the highest flow rates. Analysis of the anisotropy of the permeability coefficient indicates that this parameter has no significant effect on the water inflow, and in all cases, the circular-shaped tunnel, in contrast to other geometric shapes studied in this article, has the lowest water inflow rate.

As expected, an increase in the area of the underground space leads to a higher water inflow into these environments. A larger space provides a greater surface for water to flow into the tunnel, and thus, an increase in the tunnel area can result in more groundwater infiltration.

Among the shapes studied, the circular-shaped tunnel has the lowest flow rate, followed by the irregular hexagon-shaped tunnel, then the D-shaped tunnel, and finally, the rectangular-shaped tunnel with the highest water inflow.

The overall dimensions of the model significantly affect the estimation of water inflow. Smaller model dimensions bring the boundary conditions closer to the tunnel boundary, leading to exaggerated estimates. In smaller model dimensions, it becomes challenging to provide accurate insights into the effect of the geometric shape of the underground space on water inflow.

Examination of the influence radius of the geometric shape of the excavated space shows that a circular-shaped tunnel has the highest influence radius, making it highly effective for drainage purposes.

Analysis of the anisotropy of the permeability coefficient indicates that this parameter has no significant effect on the water inflow, and in all cases, the circular-shaped tunnel, in contrast to other geometric shapes studied in this article, has the lowest water inflow rate.

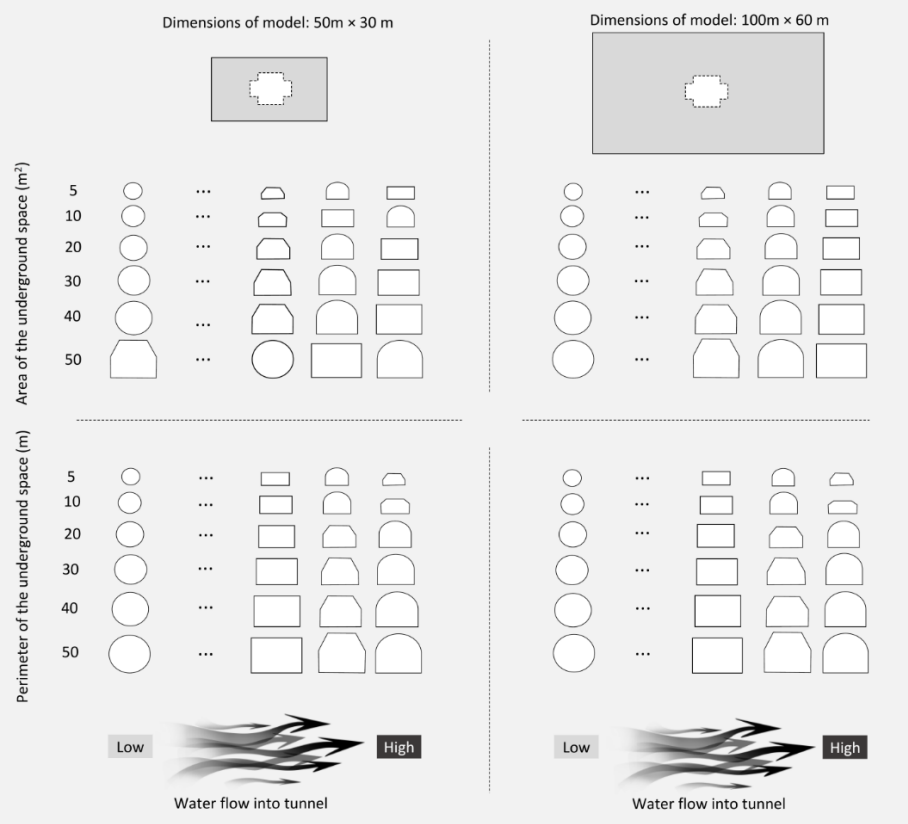


Figure 8: Schematic representation of the geometric shape effect on groundwater inflow into underground spaces

5. Conclusion:

This study aimed to investigate the impact of the geometric shape of underground spaces on water inflow into these environments. Based on calculations performed for 576 different models using Seep/w software, here are some key points:

- Circular tunnels generally have the lowest water inflow rates, regardless of model dimensions or anisotropy of the permeability coefficient. This aligns with the intuition that minimizing surface area exposed to water minimizes inflow.
- Wider influence radius of circular tunnels further helps reduce water inflow by capturing water from a larger area around the tunnel. This is illustrated in Figure 6, which you mentioned.
- Model dimensions and boundary conditions can significantly impact water inflow, making generalizations difficult. While circular tunnels performed well across various parameters, the optimal shape can change depending on the specific situation.
- Irregular hexagon tunnels can be preferable in certain limited cases, such as when model dimensions are close to the underground space boundaries. However, this finding is unlikely to be relevant for most practical tunnel designs.
- Anisotropy of the permeability coefficient, which measures how easily water flows in different directions, has minimal impact on water inflow. This suggests that the shape of the tunnel is a more important factor than the underlying soil properties.

Overall, this research highlights the importance of considering both geometric shape and overall dimensions when designing tunnels for effective drainage. It also suggests that circular tunnels are generally a safe choice, but further analysis might be needed based on specific project details. It's important to note that predicting the exact influence radius requires complex numerical modeling or physical experiments that consider all these factors. The impact of shape is just one aspect; other design and geological factors play equally important roles.

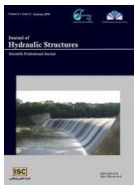
References

1. Cesano D. 1999. Prediction of Groundwater flows into Underground Constructions in Hard Rocks. Royal Institute of Technology, Stockholm, Sweden.
2. Maleki, Z., Farhadian, H., & Nikvar-Hassani, A. (2021). Geological hazards in tunnelling: the example of Gelas water conveyance tunnel, Iran. Quarterly Journal of Engineering Geology and Hydrogeology, 54(1), qjegh2019-114.
3. Bashari Moghaddam, Z., Mohammadvali Samani, H., & Mousavi Jahromi, S. H. (2021). Turbulent Flow Modeling at Tunnel Spillway Concave Bends and Prediction of Pressure using Artificial Neural Network. Journal of Hydraulic Structures, 7(1), 1-15.
4. Farhadian, H. (2021). A new empirical chart for rockburst analysis in tunnelling: Tunnel rockburst classification (TRC). International Journal of Mining Science and Technology, 31(4), 603-610.
5. Ghorbani, E., Ghadernejad, S., Emami, D., & Nejati, H. (2021). Estimating groundwater inflow into Dorud-Khorramabad railway tunnel using analytical and numerical methods. International Journal of Mining and Geo-Engineering, 55(1), 33-41.
6. Farhadian, H., & Nikvar-Hassani, A. (2019). Water flow into tunnels in discontinuous rock: a short critical review of the analytical solution of the art. Bulletin of Engineering Geology and the Environment, 78, 3833-3849.
7. El Tani, M. (2003). Circular tunnel in a semi-infinite aquifer. Tunnelling and underground space technology, 18(1), 49-55.
8. Farhadian, H., & Katibeh, H. (2015). Groundwater seepage estimation into Amirkabir tunnel using analytical methods and DEM and SGR method. International Journal of Civil and Environmental Engineering, 9(3), 296-301.
9. Farhadian, H., Katibeh, H., & Huggenberger, P. (2016). Empirical model for estimating groundwater flow into tunnel in discontinuous rock masses. Environmental earth sciences, 75, 1-16.
10. Farhadian, H., Katibeh, H., Huggenberger, P., & Butscher, C. (2016). Optimum model extent for numerical simulation of tunnel inflow in fractured rock. Tunnelling and Underground Space Technology, 60, 21-29.
11. Yoon, J. U., Han, J. W., Joo, E. J., & Shin, J. H. (2014). Effects of tunnel shapes in structural and hydraulic interaction. KSCE Journal of Civil Engineering, 18, 735-741.
12. Han, G., Hu, M., & Li, Y. (2014). Effects of Tunnel Shape on Water-Sealed Oil Storage Caverns' Seepage Flow. In ICPTT 2014: Creating Infrastructure for a Sustainable World (pp. 724-731).
13. Wu, J., Wu, L., Han, Y. H., Sun, M., & Lu, Y. N. (2023). Numerical investigation of water inflow and seepage characteristics in a tunnel crossing two overlapped parallel faults. Scientific Reports, 13(1), 11806.
14. Wang, J., Wei, Y., Xie, Z., Jiang, X., Zhang, H., & Lu, K. (2020). Influence of the water spray flow rate and angle on the critical velocity in tunnels with longitudinal ventilation. Energy, 190, 116466.

15. Yang, J. H., Jiang, Q. H., Zhang, Q. B., & Zhao, J. (2018). Dynamic stress adjustment and rock damage during blasting excavation in a deep-buried circular tunnel. Tunnelling and Underground Space Technology, 71, 591-604.
16. Su, K., Zhou, Y., Wu, H., Shi, C., & Zhou, L. (2017). An analytical method for groundwater inflow into a drained circular tunnel. Groundwater, 55(5), 712-721.
17. Pan, Y. H., Qi, J. R., Zhang, J. F., Peng, Y. X., Chen, C., Ma, H. N., & Ye, C. (2022). A comparative study on steady-state water inflow into a circular underwater tunnel with an excavation damage zone. Water, 14(19), 3154.
18. Nikvar Hassani, A., Katibeh, H., & Farhadian, H. (2016). Numerical analysis of steady-state groundwater inflow into Tabriz line 2 metro tunnel, northwestern Iran, with special consideration of model dimensions. Bulletin of Engineering Geology and the Environment, 75, 1617-1627.
19. Farhadian, H., Maleki, Z., & Eslaminezhad, S. A. (2021). Assessment of the Optimum Depth of Sealing Cutoff Walls in the Clay Core of Peygham-Chay Dam. Journal of Hydraulic Structures, 7(1), 59-76.
20. Moeini, H., Farhadian, H., & Nikvar-Hassani, A. (2018). Determination of the optimum sealing method for Azad pumped storage dam considering seepage analysis. Arabian Journal of Geosciences, 11, 1-13.
21. Hassani, A. N., Farhadian, H., & Katibeh, H. (2018). A comparative study on evaluation of steady-state groundwater inflow into a circular shallow tunnel. Tunnelling and Underground Space Technology, 73, 15-25.

© 2024 by the authors. Licensee SCU, Ahvaz, Iran. This article is an open access article distributed under the terms and conditions of the Creative Commons Attribution 4.0 International (CC BY 4.0 license) (http://creativecommons.org/licenses/by/4.0/).

Journal of Hydraulic Structures
J. Hydraul. Struct., 2024; 10(1): 80-105
DOI: 10.22055/jhs.2024.46290.1290



OPEN ACCESS

Integrated Hydrodynamic Modeling of Dam Failure and Downstream Flood Inundation near Kathmandu, Nepal using MIKE Hydro River Model

Kuldeep Pareta[1]

Abstract

The integrated hydrodynamic modeling study conducted in the Kathmandu valley, Nepal, utilizing the MIKE Hydro River Model and incorporating diverse datasets, including satellite imageries, ALOS PALSAR RTC DEM data, topographical map at 1:25,000 scale and hydraulic data. Various scenarios, including a probable maximum flood (PMF) routing simulation, were examined, with a focus on assessing impacts on infrastructure, particularly two bridges located at different chainages. The analysis uncovered that the invert level at bridge-1 measured 1384.19 meters, while at bridge-2, it was recorded at 1343.98 meters. Historical records show significant floods in various years, including 1988, 1991, 1995, 1996, 1999, 2018, 2019, 2021, 2022, and 2023. During the flood inundation modeling, it was observed that the water level of the river near Gokarneshwar Mahadev and its adjacent areas experienced an elevation increase to 13 meters. Furthermore, the water level near both modeled bridges was noted to rise to 8 meters. Conversely, in other segments of the modeled river, the water level ranged between 5 to 6 meters. Hydrodynamic modeling emerged as a critical tool for flood risk assessment, providing accurate simulations of water flow behavior and facilitating informed decision-making for flood risk management and infrastructure resilience.

Keywords: Hydrodynamic modeling, dam failure, flood inundation, Kathmandu, MIKE Hydro River.

Received: 06 March 2024; Accepted: 02 April 2024

1. Introduction

Reservoir dams and water conservancy projects play a crucial role in providing various socio-economic benefits, including flood control, hydropower generation, irrigation, water supply, fisheries, and tourism [1]. However, the significant energy potential stored in reservoirs also poses a considerable risk to the safety of downstream communities and infrastructure [2-5]. Recent years

[1] DHI (India) Water & Environment Pvt Ltd., New Delhi, India. Email: kpareta13@gmail.com, kupa@dhigroup.com **(Corresponding author)**

CC BY

have witnessed a rise in the frequency of extreme climate events, which has raised concerns about the adequacy of existing flood control standards based on historical hydrological data [6, 7]. These climate extremes often result in prolonged operation of reservoir dams under unfavorable conditions, leading to increased stress on dam structures and accelerated degradation of hydraulic materials [8-11]. Consequently, the potential for dam failures is heightened, posing a severe threat to downstream areas [12-15]. Historical records of dam failures across different countries highlight the potential for catastrophic consequences, including loss of life and extensive damage to property downstream (Table 1). Dam failures can occur due to various factors such as floodwater infiltration, overtopping, material instability, or external damage [16-18]. The process of dam failure can vary, ranging from gradual deterioration to sudden, catastrophic collapse [19-21]. The nature of dam failure significantly influences the flood dynamics and downstream impacts, which can vary in terms of severity and extent [22-24].

Table 1. List of historical records of dam failures across different countries

Date	Location	Casualty	Details
1894-08-25	Gohna lake dam (Garhwal, India)	3	A landslide dam failed after authorities successfully evacuated the valley [25].
1917-08-19	Tigra dam (Gwalior, India)	1 000	Failure due to water seepage through sandstone foundation, potentially leading to increased casualties [26].
1928-03-12	St. Francis dam (Santa Clarita, California, US)	431	Dam failure attributed to geological instability of east canyon wall. Possible unreported casualties due to undocumented migrant workers below [27].
1943-05-17	Möhne dam (Ruhr, Germany)	1 579	Destroyed by bombing during World War II operation. Eleven factories destroyed, 114 seriously damaged [28].
1959-12-02	Malpasset dam (Côte d'Azur, France)	423	Geological fault possibly enhanced by explosives work during construction; initial geo-study was not thorough. Two villages were destroyed [29].
1961-07-12	Panshet dam (Pune, India)[2]	1,000	Dam wall burst under rainwater pressure. Concrete blocks substituted for steel-reinforced concrete due to steel scarcity [30].
1963-10-09	Vajont dam (Monte Toc, Italy)	2 000	Reservoir filling triggered valley wall geological failure, causing a 110 km/h landslide into the lake. Water overflowed dam in a wave. Misjudged valley stability led to village devastation [31].
1965-03-28	El Cobre new and old dam (Valparaíso, Chile)	400	Earthquake-induced liquefaction led to the release of water and mining waste, burying El Cobre town downstream [32].
1972-06-09	Canyon lake dam (South Dakota, United States)	238	Debris-clogged dam outlets resulted in flooding, causing 3,057 injuries and destruction of over 1,335 homes and 5,000 automobiles [33].
1975-08-08	Banqiao and Shimantan dams	26,000	Extreme rainfall from Typhoon Nina exceeded the dam's design capacity, leading to its failure.

[2]July 12, 1961 Lest We Forget. sakaaltimes.com. Archived from the original on 1 April 2016. Retrieved 6th March 2024.

	(Zhumadian, China)		Eleven million people lost their homes. The dam was reconstructed between 1986 and 1993 [34].
1976-06-05	Teton dam (Idaho, United States)	11	Geological issues, including unsuitable bedrock, seismic activity, and caves, contributed to the dam failure. Water leakage eroded the earthen wall, leading to the collapse. Thirteen thousand head of cattle died as a result [35, 36].
1979-08-11	Machchu-2 dam (Morbi, India)	5,000	Intense rainfall led to observed flow reaching 16307 m^3/s, three times the dam's design capacity, causing its collapse. The dam embankment, measuring 762 meters on the left and 365 meters on the right, collapsed. Floods, reaching heights of 3.6 to 9.1 meter, inundated low-lying areas of Morbi industrial town within 20 minutes [37].
1985-07-19	Val di Stava dam (Tesero, Italy)	268	Inadequate maintenance and narrow design margins resulted in outlet pipe failure, exerting pressure on the dam [38, 39].
2008-08-18	Koshi barrage (Koshi Zone, Nepal/India)	250	Failure to maintain the barrage coupled with weak monsoon and preceding drought led to its collapse, affecting 2.3 million people in northern Bihar [40, 41].
2013-06-17	Chorabari lake (Kedarnath, Uttarakhand, India)	10,000	Intense rainfall led to flash floods and the breach of Chorabari Lake Kedarnath in Uttarakhand, resulting in widespread devastation and loss of life [42, 43, 44].
2018-07-11	Panjshir valley dam (Panjshir Valley, Afghanistan)	10	A deteriorated dam collapsed during heavy summer rainfall, causing 13 individuals to go missing and destroying 300 houses [45].
2019-01-25	Brumadinho dam (Minas Gerais, Brazil)	270	A catastrophic failure of a tailings dam released 12 million cubic meters of tailings slurry [46, 47].
2019-07-02	Tiware dam (Ratnagiri, India)	23	Heavy rains led to the overtopping and breaching of the dam [48].
2021-02-07	Uttarakhand flood (Chamoli, Uttarkhand, India)	61	The Rishi Ganga dam was destroyed by an avalanche or glacier burst, causing a surge of water downstream and breaching the Tapovan Hydropower Plant, with 145 people reported missing [49].
2023-09-11	Derna dam collapses (Derna, Libya)	20,000	Two dams, approximately 75 and 45 meters tall, failed due to heavy rain from Storm Daniel during the Libyan civil war, inundating the city of Derna with around 30 MCM of water [50].

Given the significant risks posed by dam failures and subsequent floods, there is a critical need for comprehensive hydrodynamic modeling and mapping studies to assess and mitigate these risks effectively. This paper presents a hydrodynamic numerical modeling approach utilizing the MIKE Hydro River Model to simulate dam failure scenarios and downstream flood inundation near Kathmandu metropolitan city, Nepal. This study offers significant contributions by generating comprehensive flood inundation maps, which serve as vital tools for emergency preparedness, land-use planning, and infrastructure development initiatives. Furthermore, the insights derived

from this research can inform policy decisions aimed at bolstering dam safety protocols and resilience strategies, particularly in light of evolving climatic conditions. However, it is crucial to recognize the inherent limitations of hydrodynamic modeling, which encompass uncertainties related to input data, model assumptions, and simplifications. Despite these challenges, the study provides valuable insights into the understanding and mitigation of dam failure risks and downstream flood hazards in the Kathmandu region, thereby fostering greater resilience among local communities in the face of water-related disasters.

Additionally, the flood mapping process incorporated considerations for factors such as topography, land use, and infrastructure to accurately depict the extent of flooding. The resulting flood inundation maps provided valuable information for assessing flood risk, identifying vulnerable areas, and informing disaster management and mitigation efforts in the Kathmandu region of Nepal. The river, a significant watercourse in Kathmandu metropolitan city, has been notorious for causing recurrent floods, necessitating the urgent need for flood mapping initiatives. Historical records indicate notable flood events attributed to this river occurring in various years, including 1988, 1991, 1995, 1996, 1999, 2018, 2019, 2021, 2022, and 2023. These flood incidents have posed significant challenges to the inhabitants and infrastructure of Kathmandu metropolitan city, highlighting the importance of comprehensive flood mapping studies to understand the spatial extent, severity, and frequency of flooding along the river.

The primary objectives of this investigation are as follows: (i) to quantify the maximum probable inflow hydrograph into the reservoir utilizing the MIKE Hydro River model; (ii) to explore potential dam failure scenarios; and (iii) to generate predictive inundation maps for the studied basin in response to dam breach events.

The following sections represent a comprehensive literature review of previous dam failure modelling to discern and analyze the latest methodologies employed in research conducted by various authors worldwide. This analysis aids in the selection of an appropriate methodology and numerical model for conducting dam failure study.

Johnson et al. [51] proposed breach shapes for earthen, gravity, and arch dams. They found that earthen dams commonly exhibit a trapezoidal breach shape, with occasional instances of triangular breaches. Singh et al. [52] found that breach widths ranged from 2 to 5 times the dam height in 20 dam failures. The time to complete failure was typically 0.25 to 1 hour. Maximum overtopping depths before failure ranged from 0.15 to 0.61 meters for overtopping failures. MacDonald et al. [53] proposed a breach formation factor, linking outflow volume and water depth at failure. They associated embankment material removal with this factor across dam types. Most breaches had 1h:2v slopes, triangular or trapezoidal shapes, based on depth. An envelope curve for breach formation time versus eroded material volume was suggested for earth fill dams, while non-earth fill dam failures were less predictable due to structural instabilities. Petra et al. [54] showed that breach width and formation time significantly affect discharge, inundation levels, and flood arrival time near the dam. Downstream, breach formation time alters flood peak timing, but peak discharge and inundation levels remain relatively insensitive. Singh et al. [55] compared DAMBRK and HEC-1 for eight breached dams, varying breach parameters to predict peak outflows. Larger reservoirs showed larger peak outflow changes (35-87%) with breach width (BW) variations, while smaller reservoirs exhibited smaller changes (6-50%).

Froehlich [56] developed non-dimensional equations to predict breach width, side-slope factor, and breach formation time based on dam characteristics. Results indicated wider breaches and faster lateral erosion for overtopping-induced failures compared to other causes. Wurbs [57] identified breach simulation as the most uncertain aspect of dam-breach flood wave modeling. In large reservoirs, peak discharge correlates with breach dimensions, while accurate breach

geometry prediction is crucial. In small reservoirs, peak outflow precedes complete breach development, emphasizing the importance of breach formation rate. Singh et al. [58] analyzed breach geometry and failure times from 52 case studies. They found Btop/Bbottom ratio ranging from 1.06 to 1.74, with an average of 1.29. Breach side slopes were typically 10-50°. Most failure times were under 3 hours, with 50% under 1.5 hours. Von Thun et al. [59] and Dewey et al. [60] used data from previous studies to propose guidance for estimating breach parameters. They suggested 1:1 side slope, except for dams with cohesive shells or wide cores, where 1:2 or 1:3 slopes may be suitable.

Horritt et al. [61] evaluated 1D and 2D flood models HEC-RAS, LISFLOOD-FP, and TELEMAC-2D on a 60 km stretch of the River Severn, UK. Using radar remote sensing data, they calibrated models with floodplain and channel friction parameters, finding HEC-RAS and TELEMAC-2D reliable with observed data, while LISFLOOD-FP required calibration against inundated area. Merritt et al. [62] evaluated empirical, conceptual, and physical models for sediment generation and transport processes. They found that empirical and simple conceptual models are suitable for limited input data and computational simplicity, while physical models are data-intensive and complex, posing challenges in areas with limited data availability. Yang et al. [63] developed a direct processing approach for river floodplain delineation using GIS integration with HEC-RAS. They simulated water surface profiles for various storm events and validated the model using a 100-year flood zone. The study emphasizes integrating hydraulic data with GIS for floodplain mapping. Bani Hashemi et al. [64] applied a 2D dam failure model based on Fred and Mac Cormac, enhancing it with second-order accuracy and artificial viscosity. This combination effectively simulated gradual dam failure and shock flow resolution despite its simplicity. Montazeri Naming et al. [65] developed one and two-dimensional numerical models to simulate the wave of Maronik Dam failure and subsequent flooding.

Abareshi et al. [66] assessed the risks associated with Taragh concrete dam failure near Mashhad city using MIKE 11 software. They identified flood-prone areas by combining flood speed and depth maps through a risk matrix, determining risk rates for each area. Esmaili et al. [67] used Fluent software to model hydraulic failure of a dam caused by sudden floods. Their one-dimensional study explored two scenarios: flood and failure, and failure without flood. Results emphasized the significance of the applied network over the time step in influencing outcomes. Ahmadi [68] numerically modeled gradual dam failure, initiating erosion with an initial gap on the crown. Model results were compared with laboratory and field test results, showing relatively good consistency through provided charts. Timbadiya et al. [69] created a hydrodynamic model of the lower Tapi River with HEC-RAS for unsteady flow conditions using surveyed stream data and boundary conditions. Simulated floods closely matched observed flows at various stations, validating the model for flood forecasting in the lower Tapi River. Godariz et al. [70] analyzed the risk of earth dam failure caused by body overflow considering uncertain input parameters. Nejad et al.[71] simulated dam failure and wave propagation using a limited volume numerical method in two dimensions. Seiyfi Zade et al. [72] investigated PolRud dam failure due to breach and flood routing downstream using the BREACH GUI model. Flood effects analyzed with the HEC-RAS model for determining dam failure impacts.

Aureli et al. [73] assessed hydrodynamic forces on dams leading to failure with 2D and 3D models, combining experimental and numerical approaches. Kocaman et al. [74] explored dam failure due to shock waves impacting a vertical wall using empirical testing and computational fluid dynamics (CFD) simulations with the Volume of Fluid (VOF) method. Wood et al. [75] investigated dam failure flows in canals with a 90-degree bend using experimental and numerical methods. The study employed 2-dimensional equations, specifically the Shallow Water Equations

(SWE). Dottori et al. [76] developed high-resolution flood hazard models using daily river discharge data from the Global Flood Awareness System (GloFAS). They evaluated flood hazard maps for different return periods globally, comparing them with official flood maps and studying model sensitivity and limitations. Vermee et al. [77] developed a dam break flow simulation model for Bargi Dam on the Narmada River near Jabalpur. The study focused on overtopping failure of the earthen part, examining its impact on Narmada River, Jabalpur city, and presenting inundation maps using MIKE11-DB.

Palu MC et al. [78] improved 1D routing algorithms for dam-break floods. Classical models showed errors up to ~18% in peak discharge prediction and up to 4-hour differences in peak timing. Their modified approach, using a linear diffusive wave format, reduced errors to less than -0.1% in peak discharge prediction. Li et al. [79] conducted a sensitivity analysis on rock-fill dam break floods for different durations. They found that longer durations decrease peak discharge, extend flood appearance time, and lower water levels downstream. This research aids in optimizing dam design and flood countermeasures. Adityawan et al. [80] conducted numerical modeling of dam break flow through urban areas, comparing three approaches for defining buildings: wall boundary, contour, and Manning. They found the wall boundary approach to be most accurate, recommending it for buildings without height variation or submergence. Annunziato et al. [81] developed a rapid procedure for assessing the consequences of dam break events using the shallow water model NAMI DANCE. This allows quick generation of input decks and output quantities, facilitating fast analysis of flood risk. The method can be integrated into systems like GDACS for timely flood alerts.

2. Methodology

2.1. About the study area

The study area is situated near Kathmandu, Nepal, focusing on the river passing through the Kathmandu metropolitan city and a dam located at the upstream of the city (Figure 1). The study area exhibits a heterogeneous topography, featuring a combination of elevated terrain characterized by hills and low-lying regions represented by valleys. This varied landscape configuration significantly influences the hydrological dynamics within the region. The river network serves as a fundamental component of the local hydrology, functioning as the primary conduit for water flow and distribution throughout the Kathmandu valley. Moreover, the presence of a dam situated upstream of Kathmandu significantly contributes to the management of the region's water resources and the implementation of flood control measures. However, the area's distinctive geographical attributes, coupled with the ongoing processes of urbanization and infrastructural expansion, pose formidable challenges for the accurate modeling of hydrodynamic processes associated with dam failure and subsequent flood inundation events.

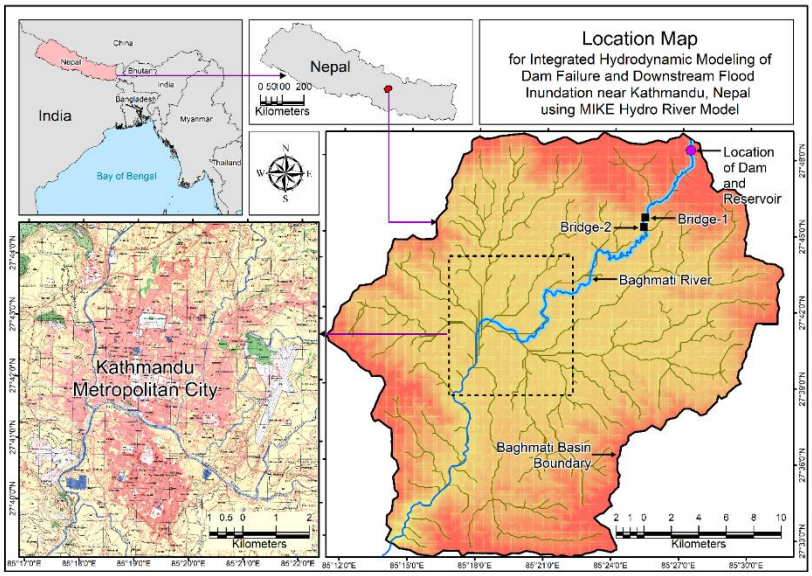


Figure 1. Location map of the study area.

2.2. Data collection

Data collection involved gathering topographic, hydrological, and hydraulic information, including digital elevation models (DEMs), river cross-section data, and reservoir characteristics. The study area's diverse terrain, including steep slopes and complex river networks, posed challenges for accurate modeling. MIKE Hydro River Model facilitated comprehensive analysis by integrating various datasets, enabling a detailed assessment of flood dynamics and inundation extents.

Landsat-9 OLI-2 satellite imagery, characterized by a spatial resolution of 30 meters, was sourced from the USGS Earth Explorer database, dated 14th May 2023. Subsequently, a fusion process was employed to integrate the G-R-NIR bands (30 meters), with the PAN band (15 meters). This fusion technique aimed to enhance the overall spatial resolution of the imagery. The resultant satellite data, thus augmented, facilitated the extraction of general features and Land Use/Land Cover (LULC) information within the study area. Specifically, the LULC data derived from this imagery served as a basis for determining Manning (M) coefficients utilized in the hydrodynamic modeling of the study area.

Sentinel-2 satellite imagery with a spatial resolution of 10 meters, acquired on 23rd May 2023, was procured from the European Space Agency's Copernicus Programme via the Sentinels Scientific Data Hub. This satellite data served as a critical resource for validating the observed flood event against the inundation map predicted by the hydrodynamic model. Through comparative analysis, the accuracy and reliability of the model's predictions were assessed, contributing to the validation and refinement of the flood inundation mapping process.

ALOS PALSAR (radiometric terrain correction) DEM data with a spatial resolution of 12.5 meters, was obtained from the Alaska Satellite Facility (ASF) via Vertex. This high-resolution DEM data facilitated the analysis of the general topography within the study area, enabling the extraction of cross-sectional profiles of the river. The drainage network and basin boundary of the study area were derived from the DEM data as well.

A topographical map, designated as Sheet No. 2785 06A and scaled at 1:25,000, was acquired from the Survey Department, Government of Nepal. This map served as a foundational resource

for the study, facilitating the overlay of flood inundation data to assess the extent of settlement flooding. Additionally, Google Earth satellite imagery was leveraged for comparative analysis and validation of the observed flood inundation patterns. These mapping resources provided essential spatial context and reference points for accurately depicting and analyzing the impacts of flooding on the surrounding landscape and settlements.

Hydrological and hydraulic data, including stage-discharge relations, area-elevation curves of reservoirs, rating curves of spillways, and probable maximum flood information, were sourced from the Department of Hydrology and Meteorology (DHM), Government of Nepal. These datasets were obtained from the DHM's repository. They played a crucial role in defining the boundary conditions of the hydrodynamic model. By utilizing these datasets, accurate representations of the river system's behavior and response to various scenarios were established, enhancing the reliability and validity of the model simulations.

2.3. Component of MIKE Hydro River for dam failure

In the dam failure analysis conducted using the MIKE Hydro River Model, a schematic diagram of the river and reservoir system is essential for accurately simulating the flood inundation dynamics. This schematic diagram encompasses various elements, including the river channel, hydraulic structures such as dams and spillways, and the reservoir area upstream of the dam. Additionally, it incorporates topographic features such as elevation contours and land use/land cover information to capture the spatial distribution of floodwaters. The reservoir model accounts for the storage capacity of the reservoir and the inflow-outflow dynamics, while the river model represents the hydraulic behavior of the river channel and floodplain areas (Figure 2). By integrating these components into a coherent schematic diagram, the MIKE Hydro River Model enables researchers and practitioners to simulate dam failure scenarios with high fidelity, providing valuable insights into flood inundation extent, depth, and propagation patterns for effective flood risk assessment and management.

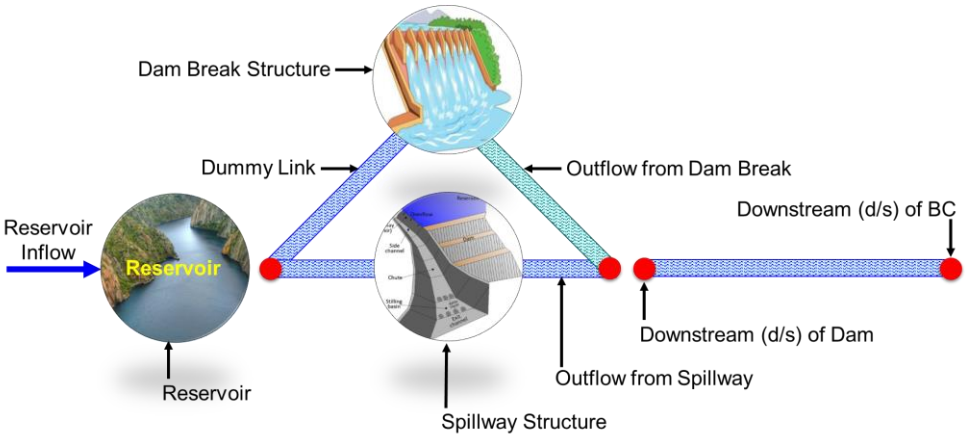


Figure 2. Schematic diagram of MIKE Model for dam failure modelling [82].

2.4. Dam breach parameters

The estimation of dam failure flood characteristics relies on several key parameters related to the dam breach process. These parameters include the initial and final breach width, the shape of the breach, the duration of breach development, and the reservoir level at the onset of breach

initiation. The mechanism governing breach formation predominantly hinges on the type of dam and the underlying cause of dam failure. These factors collectively determine the dynamics of the breach and subsequent flood inundation, highlighting the importance of accurately defining these parameters in dam failure modeling for effective risk assessment and mitigation strategies. The graphical representation of the physical parameters is depicted in Figure 3, providing a visual summary of the key characteristics.

The breach depth, alternatively termed breach height in certain literature, denotes the vertical dimension of the breach, extending from the crest of the dam to the invert of the breach. In certain instances, publications may specify the reservoir head at the breach, measured from the surface level of the reservoir to the breach invert.

The breach width, a critical parameter in dam failure analysis, significantly influences the peak flow rate and subsequent inundation levels downstream. Studies often document either the mean breach width or specify measurements at both the top and bottom of the breach aperture.

The breach side slope factor, in conjunction with breach width and depth, delineates the geometric configuration of the breach aperture. While crucial, precise estimation of breach side slope angles typically assumes lesser significance compared to accurately predicting breach width and depth.

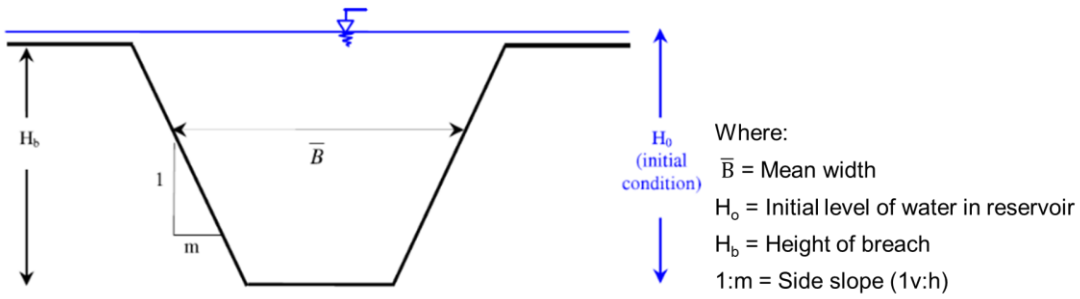


Figure 3. Final dimension of a trapezoidal dam breach approximation

Research on various dam failures suggests that failures in Concrete-Faced Rockfill Dams (CFRDs) often occur due to slumping of the embankment shoulders, resulting in overtopping. Additionally, issues such as cracking and internal erosion of the abutments during initial reservoir filling may lead to piping failures caused by seepage. Furthermore, failure of the spillway can contribute to erosion of the downstream shoulder.

2.4.1. Review of guidance for breach parameters

Several governmental bodies have released regulatory frameworks outlining potential ranges for breach parameters such as width, side slopes, and development time. A comprehensive overview of this guidance is presented in Table 2.

Table 2. Ranges of Possible Values for Breach Characteristics [83].

Dam Type	Average Breach Width (B_{avg})	Horizontal component of breach side slope (H)	Failure time (t_f) in hrs.	References
Earthen / rockfill	(0.5 to 3.0) x HD	0 to 1	0.5 to 4.0	HEC [84]
	(0.5 to 5.0) x HD	0 to 1	0.1 to 4.0*	USACE [85]
	(1.0 to 5.0) x HD	0 to 1	0.1 to 1.0	FERC [86]
	(2.0 to 5.0) x HD	0 to 1 (slightly larger)	0.1 to 1.0	NWS [87]
Concrete gravity	Multiple Monoliths	Vertical	0.1 to 0.5	USACE [85]
	Usually, ≤ 0.5 L	Vertical	0.1 to 0.3	FERC [86]
	Usually, ≤ 0.5 L	Vertical	0.1 to 0.2	NWS [87]
Concrete arch	Entire Dam	Valley wall slope	≤ 0.1	HEC [84]
	(0.8 x L) to L	0 to valley walls	≤ 0.1	USACE [85]
	Entire Dam	0 to valley walls	≤ 0.1	FERC [86]
	(0.8 x L) to L	0 to valley walls	≤ 0.1	NWS [87]
Slag / refuse	(0.8 x L) to L	1.0 to 2.0	0.1 to 0.3	FERC [86]
	(0.8 x L) to L		≤ 0.1	NWS [87]
Where:	*HD = Height of the dam. L = Length of the dam crest*			
** Note*	*Dams characterized by extensive water volumes and extended crest lengths are prone to sustained erosion over prolonged periods, contingent upon the ongoing flow of a substantial water volume through the breach. Consequently, such dams may exhibit broader breach widths and protracted breach development times compared to documented cases.*			

2.4.2. Regression Equations

The regression equations delineated herein have been employed across various dam safety investigations documented in the literature and are under contemplation for integration into the guidance framework for the Portfolio Risk Assessment study conducted by the Corps of Engineers: (i) Froehlich [56, 88, 89]; (ii) MacDonald et al. [53]; and (iii) Von Thun et al. [59].

Froehlich equation [56, 88, 89] conducted an analysis incorporating 63 datasets pertaining to various dam types, including earthen, zoned earthen, earthen dams with a core wall (i.e., clay), and rockfill dams. The study aimed to derive equations for estimating average breach width, side slopes, and failure time. In the application of these equations, it was assumed that the breach extends from the crest of the dam to the natural ground elevation at the centerline of the breach location. The empirical equation is:

$$B_{avg} = 0{,}1803 K_0 V_w^{0,32} h_b^{0,19}$$
$$t_f = 0{,}00254 (V_w)^{0,53} h_b^{-0,9}$$

MacDonald and Langridge-Monopolis equation [53] conducted an analysis using 42 datasets primarily comprising earthfill, earthfill with a clay core, and rockfill dams. They aimed to establish a relationship known as the "Breach Formation Factor," which is the product of the volume of water released from the dam (V_{out}) and the water height above the dam. This factor was correlated with the volume of material eroded from the dam's embankment. The parameter V_{out}, representing the water volume passing through the breach, is typically unknown prior to breach analysis and is initially estimated as the reservoir water volume at breach initiation. Subsequently, after performing breach analysis and obtaining a better estimate of the actual water volume passing through the breach, parameters can be recalculated iteratively. The empirical equation is:

$$V_{er} = 0{,}0261 (V_w h_w)^{0,769}$$ for earthfill

$V_{er} = 0{,}00348(V_w h_w)^{0{,}852}$ for noneartfill
$t_f = 0{,}0179 V_{er}^{0{,}364}$

Von Thun and Gillette equation [59] analyzed data from 57 dams sourced from [56] [53]. Their methodology proposes breach side slopes typically set at 1.0H:1.0V, with exceptions for dams with cohesive soils, where slopes range from 0.5H:1V to 0.33H:1V. They formulated two sets of equations to estimate breach development time, contingent on the embankment material. The empirical equation is:

$B_{avg} = 2{,}5h_w + C_b$
$C_b = 54.9$ for b_w for reservoir storage greater than 12.8 Mcum
$t_f = 0{,}015h_w$ highly erodible
$t_f = 0{,}020h_w + 0{,}25$ erosion resistant

Breach parameters: In the current study, the initiation point, and initial breach level correspond to the crest level of the breaching section and the riverbed level, respectively. A sensitivity analysis was conducted, varying breach width, breach time, and breach slope. The breach parameters outlined in Table 3 were chosen for the dam failure investigation.

Table 3. Breach parameter for investigative dam.

Average breach width (m)	Time of failure (hr)	Slope (H)	Breach level (m)		Remarks
			Initial	Final	
20	0.5 1 2 4	0.5	2095.5	2076	Scenario-1
30	0.5 1 2 4	1.0	2095.5	2076	Scenario-2
45	0.5 1 2 4		2095.5	2076	Scenario-3

2.5. Model setup MIKE Hydro River HD Model

The MIKE Hydro River HD Model was configured to simulate dam failure and subsequent flood inundation near Kathmandu, Nepal. The model setup involved defining the hydraulic characteristics of the river, dam, and reservoir. Detailed topographic and bathymetric data were incorporated to accurately represent the river and reservoir geometry. Boundary conditions such as upstream flow conditions and downstream water levels were specified to mimic real-world scenarios. The model was calibrated and validated using observed data to ensure its accuracy in predicting river flow and flood inundation extents. Additionally, the dam failure parameters obtained from sensitivity analysis were integrated into the model setup to simulate various dam failure scenarios.

2.5.1. River network and topography

The network comprises the reservoir of the dam and the river downstream of the dam. Figure 4 illustrates the network layout, including the precise positioning of the dam and bridges. The reservoir extends over a length of 688 meters, while the river spans a length of 33.7 km. The river is discretized into 241 cross-sections spaced at regular intervals along its length. This comprehensive representation of the network's geometry and hydraulic properties ensures accurate modeling of dam failure and flood inundation dynamics.

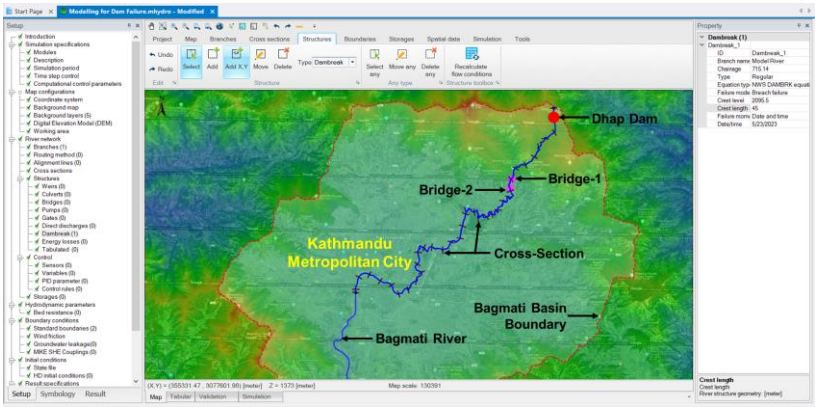


Figure 4. MIKE Hydro River model setup for dam failure analysis

2.5.2. Reservoir and dam

In the model, the reservoir is depicted through a distinct reservoir branch, with its elevation-surface area relationship delineated at chainage "0" km of the reservoir branch. The corresponding data detailing this relationship is provided in Table 4. This approach ensures that the reservoir's behavior and characteristics are accurately captured within the modeling framework, facilitating a comprehensive analysis of dam failure and subsequent flood inundation dynamics.

Table 4. Area-elevation curve of reservoir

Elevation (m)	Surface Area (m^2)	Elevation (m)	Surface Area (m^2)	Elevation (m)	Surface Area (m^2)	Elevation (m)	Surface Area (m^2)
2075.86	0.00	2081.00	11136.94	2086.50	62322.90	2092.00	111108.90
2076.00	3.32	2081.50	12971.78	2087.00	67495.95	2092.50	115406.83
2076.50	515.27	2082.00	15041.71	2087.50	73011.19	2093.00	119612.97
2077.00	867.48	2082.50	16454.74	2088.00	78883.13	2093.50	123815.64
2077.50	1260.03	2083.00	17902.54	2088.50	83203.16	2094.00	128015.24
2078.00	1686.16	2083.50	19388.34	2089.00	87406.61	2094.50	132793.17
2078.50	2182.52	2084.00	20912.66	2089.50	91529.07	2095.00	137438.62
2079.00	2797.87	2084.50	23143.60	2090.00	95544.41	2095.50	142125.02
2079.50	3558.56	2085.00	26681.10	2090.50	99409.71		
2080.00	4451.89	2085.50	31702.84	2091.00	103246.60		
2080.50	9533.45	2086.00	57547.00	2091.50	107146.14		

2.5.3. Spillway

In the model, the spillway is represented as an overflow weir, designed to manage excess water flow from the reservoir. This hydraulic structure plays a crucial role in controlling the water level within the reservoir and preventing overtopping during periods of high inflow. The spillway's hydraulic performance is characterized by its rating curve, which delineates the relationship

between the water level in the reservoir and the corresponding discharge through the spillway. This rating curve provides crucial information for accurately simulating the spillway's behavior under varying hydrological conditions (Figure 5 (A)). This information is vital for effectively modeling the spillway's operation and assessing its capacity to handle potential flood events. By incorporating the spillway's characteristics into the model, researchers can simulate various scenarios and evaluate the spillway's performance in mitigating flood risks and safeguarding downstream areas from potential inundation.

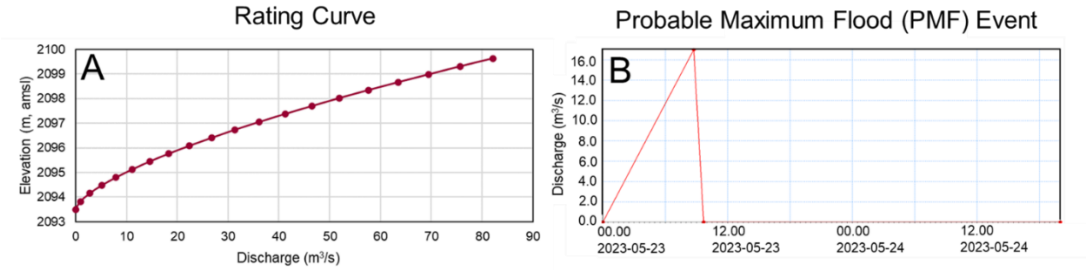


Figure 5. (A) Rating curve of spillway, (B) Probable Maximum Flood (PMF) used as U/S boundary condition

2.5.4. Boundary condition

In the MIKE Hydro River Model for dam failure analysis, boundary conditions play a crucial role in defining the hydraulic behavior of the river system [90]. At the upstream boundary, the Probable Maximum Flood (PMF) is employed as the boundary condition. The PMF represents the extreme flood event that could potentially occur in the upstream catchment area, thus providing a rigorous test of the dam's resilience to severe flooding scenarios. PMF shown in Figure 5 (B) is used as upstream boundary condition.

Conversely, at the downstream boundary of the river model, the boundary condition is defined by a stage-discharge relation. This relation specifies the relationship between the water level (stage) in the river and the corresponding discharge rate. By incorporating the stage-discharge relation at the downstream boundary, the model can accurately simulate the outflow from the river system under varying hydraulic conditions.

The downstream boundary condition for dam failure analysis is derived from Manning's equation. By applying Manning's equation, the stage-discharge relation establishes the correlation between the water stage (depth) in the river and the corresponding discharge rate. Table 5 provides the stage-discharge relation, delineating specific water stage levels and their corresponding discharge rates for the downstream boundary of the river model.

Table 5. Stage-discharge relation used as downstream boundary condition.

Stage (m, amsl)	Discharge (m^3/s)	Stage (m, amsl)	Discharge (m^3/s)	Stage (m, amsl)	Discharge (m^3/s)	Stage (m, amsl)	Discharge (m^3/s)
1277.56	0.00	1279.25	26.61	1280.94	177.56	1282.62	478.63
1277.90	0.65	1279.59	44.57	1281.27	226.10	1282.96	556.18
1278.24	3.34	1279.92	68.92	1281.61	280.55	1283.30	639.52
1278.57	8.22	1280.26	98.99	1281.95	340.80	1283.64	728.33
1278.91	15.36	1280.60	135.12	1282.29	406.84	1283.97	824.37

2.6. Critical condition for dam failure study

In the dam failure study, a critical scenario occurs when the reservoir is at its full reservoir level (FRL) and subjected to the probable maximum flood (PMF) hydrograph. In this study, the initial step involved reservoir routing by introducing the PMF into the reservoir while considering the water level at the FRL of 2093.5 m and assuming full openness of the spillway gates. The reservoir routing analysis revealed that the maximum water level reached was 2093.81 m, occurring one hour after the application of the PMF. The time series data illustrating the variation in reservoir level during the routing of the PMF is depicted in Figure 6. As the top of the dam is situated at an elevation of 2095.5 m, there is no overtopping of the dam anticipated. Consequently, for the hypothetical scenario of simulating a dam breach and to ascertain the maximum flood peak resulting from the breach, it is deemed appropriate to initiate the breach when the reservoir level reaches elevation 2093.81 m. This approach ensures a comprehensive assessment of the dam failure scenario and facilitates the determination of peak flood magnitudes accurately.

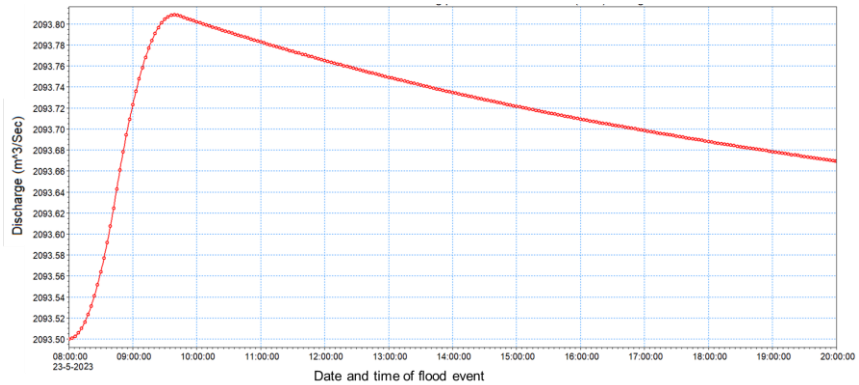


Figure 6. Time series of reservoir level during probable maximum flood (PMF) routing

2.7. Downstream flood inundation mapping

The methodology for downstream flood inundation mapping involved several key steps. Initially, the dam failure scenario was simulated using the MIKE Hydro River model, considering various breach parameters and hydraulic conditions. Once the dam breach was modeled, the resulting flood wave propagation downstream was simulated using the hydraulic model [91]. The downstream flood inundation mapping methodology included the delineation of flood extents based on water levels obtained from the hydraulic simulations. This involved overlaying the simulated water levels onto digital elevation models (DEMs) of the study area to identify areas prone to inundation.

2.8. Simulation of dam failure scenarios

In the context of assessing the potential impacts stemming from a dam failure event, the modeling endeavors focused on the evaluation of flood flow, depth, and velocity at specific locations along the river, particularly at two bridge sites [92, 93]. Through rigorous numerical simulations conducted within the framework of the dam failure modeling approach, the dynamics of flood propagation were comprehensively examined. This involved capturing the complex interactions between the released floodwaters and the natural and built environment surrounding the river corridor. Specifically, the flood flow characteristics, including flow rates and depth, were meticulously analyzed to understand the extent of inundation and the corresponding hydraulic

forces exerted on infrastructure such as bridges. Furthermore, the velocity of the floodwaters was scrutinized to gauge the intensity of flow and its potential impact on structural integrity and safety at the bridge locations.

Bridge-1, positioned at a longitudinal distance of 3241 meters along the river, traverses through a region characterized by a deep valley. Within this topographical context, minimal human habitation is observed until elevations surpass approximately 10 meters above the riverbed level. Conversely, **Bridge-2**, situated at a distance of 4128 meters along the river, marks a transition point where the river corridor widens, leading into a floodplain area that is habituated. The typical elevation of this floodplain area is recorded at approximately 1355 meters above sea level (Figure 4). Such delineation of the bridge locations based on the surrounding landscape and human settlement patterns provides crucial insights into the potential vulnerability of infrastructure and communities to flood hazards resulting from dam failure scenarios.

Multiple dam failure scenarios have been simulated, incorporating variations in breach widths and failure times. This approach allows for the exploration of a range of potential outcomes under different breach conditions, facilitating a comprehensive understanding of the associated flood dynamics and inundation extents resulting from dam failure events. Following the methodology outlined in Section 3.5, the modeling results are presented in the subsequent tables. These tables provide a detailed analysis of the simulated scenarios, allowing for an informed assessment of the implications and effectiveness of the applied modeling approach in capturing the dynamics of dam failure-induced flood events.

3. Results

3.1. Effect at bridge-1 (chainage 3241 m)

Among the dam failure scenarios simulated, the one yielding the greatest flood depths entails a breach width of 45 m and a failure time of 0.5 hours. In this scenario, the model predicts a peak water depth of 3.58 m, which stands approximately 3 meters below the level of habitation, alongside a peak velocity of 10.4 m/s. The corresponding time series of water level fluctuations is depicted in Figure 7 (A), providing a comprehensive visualization of the hydrodynamic dynamics over time (Table 6).

Table 6. Effect at Bridge-1 at chainage 3241 m

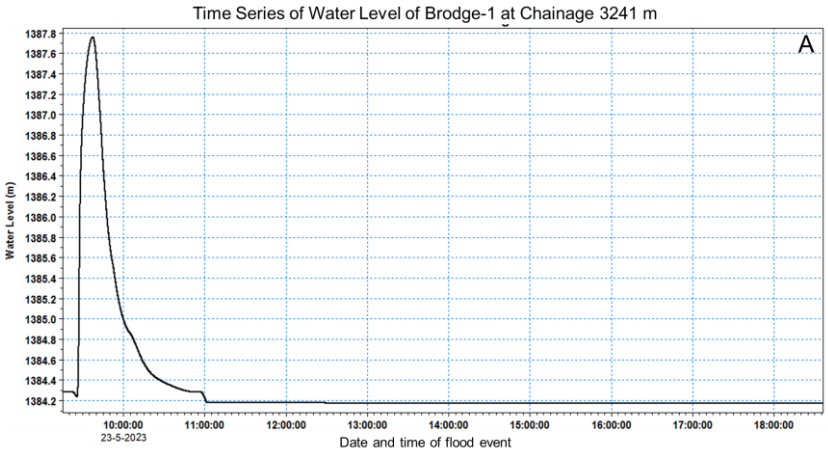
Average breach width (m)	Time of failure (hr)	Slope (H)	Breach level		Dam failure discharge (m^3/s)	Water level at bridge-1 (m, amsl)	Invert level at bridge-1 (m, amsl)
			Initial	Final			
20	0.5	1.0	2095.5	2076	858.52	1387.46	1384.19
	1				483.54	1386.83	
	2				260.34	1386.20	
	4				138.45	1385.76	
30	0.5	1.0	2095.5	2076	977.73	1387.72	
	1				526.64	1386.93	
	2				280.19	1386.26	
	4				147.51	1385.79	
45	0.5	1.0	2095.5	2076	1005.30	1387.76	
	1				540.10	1386.95	
	2				286.86	1386.28	
	4				150.50	1385.80	

3.2. Effect at bridge-2 (chainage 4128 m)

The dam breach scenario yielding the most substantial flood depths involves a breach width of 110 m and a failure time of 0.5 hours. In this scenario, the modeled peak water elevation reaches 1348.05 m, situated below habitation levels on both riverbanks. Concurrently, the peak velocity of the flood wave is recorded at 4.2 m/s. The hydrodynamic characteristics of this scenario are visually represented in Figure 7 (B), illustrating the propagation of the flood wave over time (Table 7).

Table 7. Effect at Bridge-2 at chainage 4128 m

Average breach width (m)	Time of failure (hr)	Slope (H)	Breach level (m)		Dam failure discharge (m^3/s)	Water level at bridge-2 (m, amsl)	Invert level at bridge-2 (m, amsl)
			Initial	Final			
20	0.5	1.0	2095.5	2076	858.52	1347.70	1343.98
	1				483.54	1346.98	
	2				260.34	1346.24	
	4				138.45	1345.65	
30	0.5	1.0	2095.5	2076	977.73	1348.08	
	1				526.64	1347.10	
	2				280.19	1346.32	
	4				147.51	1345.71	
45	0.5	1.0	2095.5	2076	1005.30	1348.05	
	1				540.10	1347.13	
	2				286.86	1346.34	
	4				150.50	1345.73	



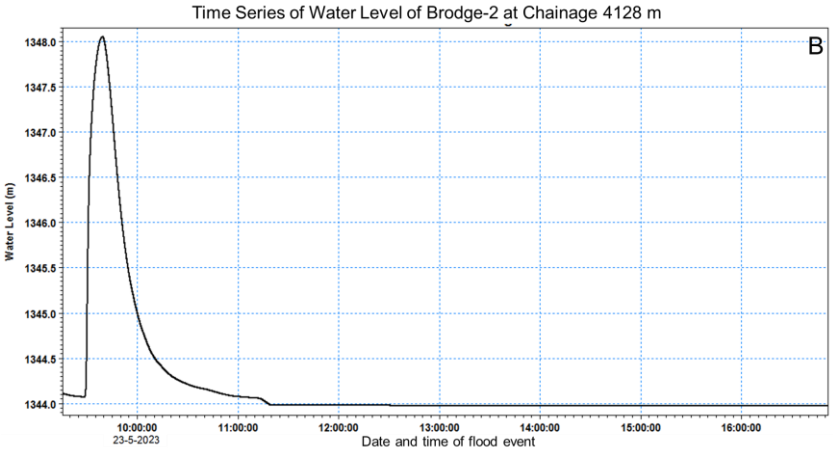


Figure 7. Time series of water level of (A) Brodge-1 at chainage 3241 m, and (B) Brodge-2 at chainage 4128 m.

3.3. Flood map

The flood maps provide a spatial interpretation of the model outputs derived from the one-dimensional simulations. In essence, the process involves interpolating the results from individual grid points across the grid space to construct comprehensive flood map. Flood map, depicted in Figure 8, encompass various land use categories such as settlement areas, cultivation land, and forested areas on GoogleEarth image. Such representations offer valuable insights into the extent and distribution of flood inundation across the study area, aiding in informed decision-making and disaster management efforts.

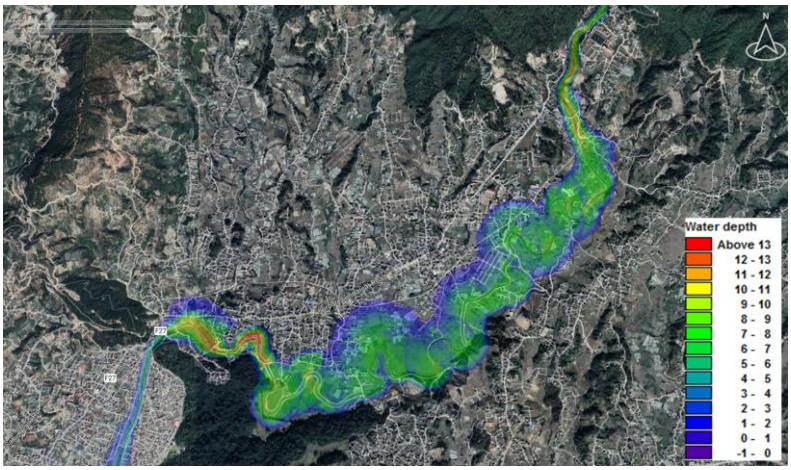


Figure 8. Flood map of model area, near Kathmandu metropolitan city.

The figures depicted in Figure 9 offer a two-dimensional representation derived from a one-dimensional model interpretation. Specifically, Figure 9 A and B illustrate flood maps corresponding to two specific locations along the river (chainage 3241 m and 4128 m). Within these maps, a red circle is employed to demarcate areas of impacted habitation. Notably, the

visualization indicates a limited number of habitations affected by the flood event, suggesting localized inundation. This observation underscores the significance of the flood mapping exercise in identifying specific areas prone to inundation and assessing the extent of habitat exposure to flood risks.

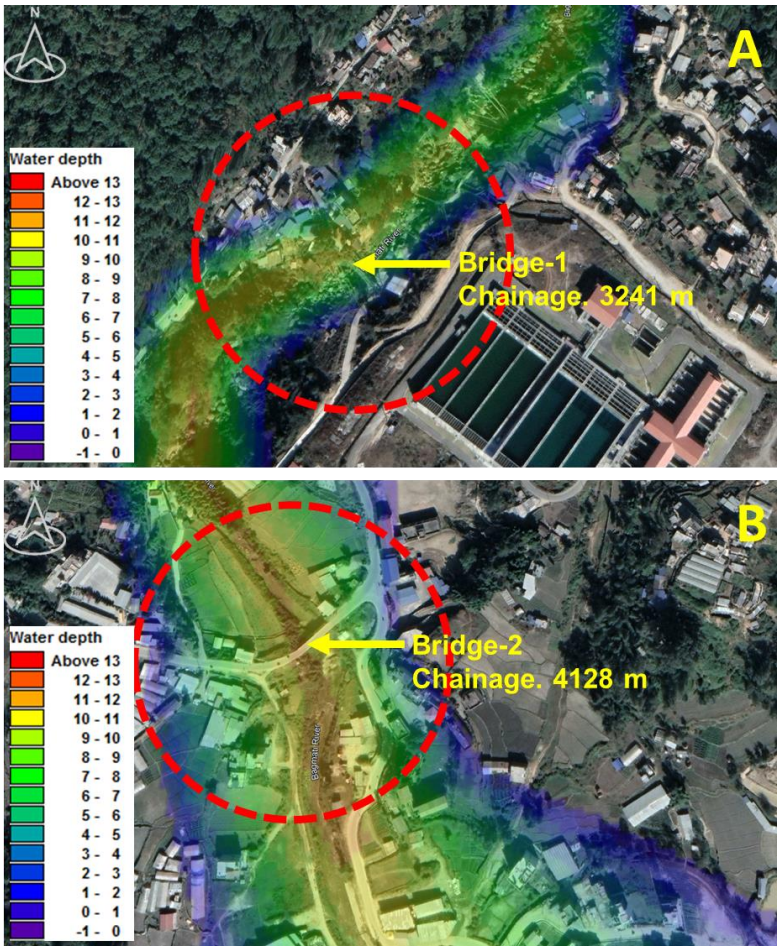


Figure 9. Flood map at (A) chainage 3241 m, and (B) chainage 4128 m.

3.4. Effect further downstream

The investigation delves deeper into the mechanism of flood peak attenuation, shedding light on the temporal dynamics of water level fluctuations. Figure 10 illustrates a series of time series depicting variations in water level over a specific period. The data showcased in the figure elucidate the process whereby the depth of the flood wave gradually diminishes, transitioning from an initial magnitude of 10 meters to a reduced level of 6 meters. This attenuation phenomenon underscores the inherent capacity of natural systems to mitigate the intensity of flood events over time, highlighting the role of hydraulic processes in regulating flood dynamics and minimizing the impact of inundation on vulnerable regions.

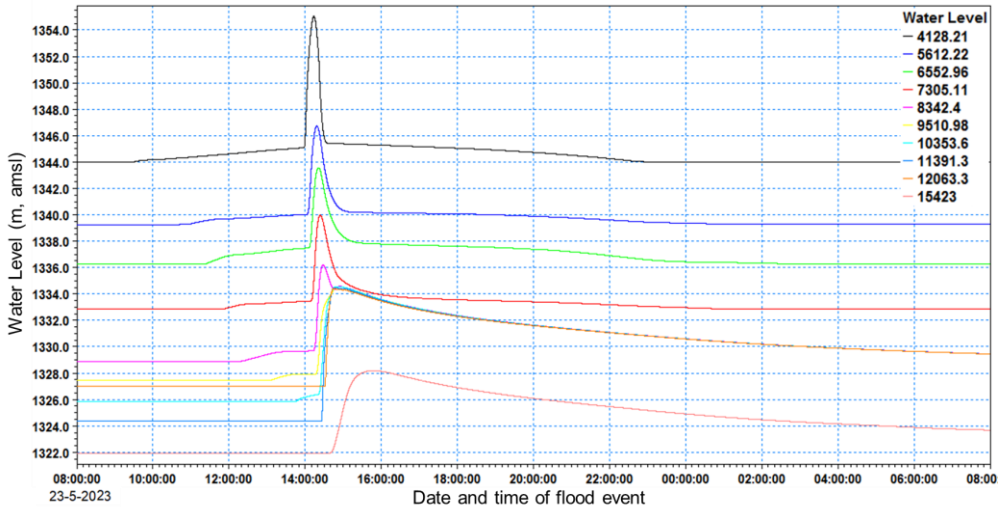


Figure 10. Flood wave attenuation at downstream of bridge (chainage 4128 m)

4. Conclusion

The integrated hydrodynamic modeling study in Kathmandu Valley, Nepal, utilized the MIKE Hydro River Model and diverse datasets including satellite imagery (Landsat-9 OLI-2, Sentinel-2), ALOS PALSAR RTC DEM data, topographical map at 1:25,000 scale, and hydraulic data to analyze flood dynamics. Sensitivity analysis of dam failure scenarios enhanced flood risk understanding and supported disaster management. Various scenarios, including the simulation of a probable maximum flood (PMF) routing, were conducted. The assessment focused on evaluating the impacts on infrastructure, specifically bridge-1 situated at chainage 3241m, and bridge-2 situated at chainage 4128m. Analysis revealed that the invert level at bridge-1 was determined to be 1384.19 m, whereas the invert level at bridge-2 was found to be 1343.98 m. Hydrodynamic modeling has emerged as a crucial tool in flood risk assessment, offering accurate simulations of water flow behavior and enabling informed decision-making for flood risk management and infrastructure resilience in vulnerable regions like Kathmandu metropolitan city. Historical data documents significant flood occurrences associated with this river across multiple years, encompassing 1988, 1991, 1995, 1996, 1999, 2018, 2019, 2021, 2022, and 2023. Historical data highlighted significant flood events from 1988 to 2023. Inundation modeling indicated river water levels of 13 meters near Gokarneshwar Mahadev, 8 meters near modeled bridges, and 5 to 6 meters elsewhere.

Hydrodynamic modeling holds significant implications for enhancing dam safety and flood management in Kathmandu metropolitan city. Through comprehensive assessments of dam safety and the creation of flood risk maps, authorities can effectively prioritize mitigation measures, formulate robust emergency response plans, and enact land use regulations to mitigate flood hazards. Furthermore, hydrodynamic modeling supports community awareness and facilitates the development of long-term adaptation strategies, promoting resilience and sustainable development practices in light of escalating flood risks. Addressing knowledge gaps through ongoing research endeavors, such as refining modeling techniques, integrating climate change scenarios, and adopting multi-hazard approaches, will further bolster flood risk assessment and management strategies. Ultimately, these efforts contribute to building resilience and reducing vulnerability in flood-prone regions like Kathmandu metropolitan city.

Funding statement

The author(s) received no financial support for the research, authorship, and/or publication of this article.

Authorship contribution statement

The author confirms being the sole contributor of this work and has approved it for publication.

Conflict of interest

The author reports no conflict of interest.

Acknowledgements

Author is grateful to Managing Director, DHI (India) Water & Environment Pvt Ltd, New Delhi, India for providing the necessary facilities to carry out this work.

References

1. Herschy, R.W. (2012). Dams and Reservoirs, Role. In L. Bengtsson, R.W. Herschy, & R.W. Fairbridge (Eds.), Encyclopedia of Lakes and Reservoirs. Encyclopedia of Earth Sciences Series. Springer, Dordrecht. https://doi.org/10.1007/978-1-4020-4410-6_155
2. Luixá-Sanmartín, J., Altarejos-García, L., Morales-Torres, A., & Escuder-Bueno, I. (2018). Climate change impacts on dam safety. Natural Hazards Earth System Sciences, 18, 2471–2488. https://doi.org/10.5194/nhess-18-2471-2018
3. DeNeale, S. T., Baecher, G. B., Stewart, K. M., Smith, E. D., & Watson, D. B. (2019). Current State-of-Practice in Dam Safety Risk Assessment. US Department of Energy, US. Retrieved from https://www.osti.gov/servlets/purl/1592163
4. Kenichiro, K., Zhongbo, Y., Guillermo, T.Q., Norlida, M.D., Ignasius, S.D.A., Yasuto, T., & Hans, T. (2021). Catalogue of hydrologic analysis for Asia and the Pacific, Volume 2: dam reservoir operation for addressing water related disasters, water scarcity and quality. UNESCO Intergovernmental Hydrological Programme. https://unesdoc.unesco.org/ark:/48223/pf0000380004
5. Kondolf, M., & Yi, J. (2022). Dam Renovation to Prolong Reservoir Life and Mitigate Dam Impacts. Water, 14(9), 1464. https://doi.org/10.3390/w14091464
6. Agonafir, C., Lakhankar, T., Khanbilvardi, R., Krakauer, N., Radell, D., & Devineni, N. (2023). A review of recent advances in urban flood research. Water Security, 19. https://doi.org/10.1016/j.wasec.2023.100141
7. Pakhale, G., Khosa, R., & Gosain, A. K. (2023). Are flood events really increasing? A case study of Krishna River Basin, India. Natural Hazards Research, 3(3), 374-384. https://doi.org/10.1016/j.nhres.2023.06.007
8. De Wrachien, D., & Mambretti, S. (2009). Dam-break Problems, Solutions and Case Studies. WIT Press, Southampton, Boston. Retrieved from https://www.witpress.com/images/stories/content_images/contents/c41429.pdf
9. Marcinkowski, P., & Grygoruk, M. (2017). Long-Term Downstream Effects of a Dam on a Lowland River Flow Regime: Case Study of the Upper Narew. Water, 9(10), 783. https://doi.org/10.3390/w9100783
10. Lyu, Z., Chai, J., Xu, Z., Qin, Y., & Cao, J. (2019). A Comprehensive Review on Reasons for Tailings Dam Failures Based on Case History. Advances in Civil Engineering. https://doi.org/10.1155/2019/4159306
11. Herbozo, J.E., Muñoz, L.E., Guerra, M.J., Minaya, V., Haro, P., Carrillo, V., Manciati, C., & Campozano, L. (2022). Non-Stationary Hydrological Regimes Due to Climate Change: The

Impact of Future Precipitation in the Spillway Design of a Reservoir, Case Study: Sube y Baja Dam, in Ecuador. Atmosphere, 13, 828. https://doi.org/10.3390/atmos13050828
12. Khosravi, K., Rostaminejad, M., Cooper, J. R., Mao, L., & Melesse, A. M. (2019). Dam break analysis and flood inundation mapping: The case study of Sefid-Roud Dam, Iran. In Extreme hydrology and climate variability (pp. 395-405). Elsevier. https://doi.org/10.1016/B978-0-12-815998-9.00031-2
13. Psomiadis, E., Tomanis, L., Kavvadias, A., Soulis, K. X., Charizopoulos, N., & Michas, S. (2021). Potential dam breach analysis and flood wave risk assessment using HEC-RAS and remote sensing data: A multicriteria approach. Water, 13, 364. https://doi.org/10.3390/w13030364
14. Ahmad, I., Waseem, M., Ashraf, A., et al. (2023). Hydrological risk assessment for Mangla Dam: compound effects of instant flow and precipitation peaks under climate change, using HEC-RAS and HEC-GeoRAS. SN Appl. Sci., 5, 344. https://doi.org/10.1007/s42452-023-05579-2
15. Paşa, Y., Peker, I. B., Hacı, A., & Gülbaz, S. (2023). Dam failure analysis and flood disaster simulation under various scenarios. Water Science and Technology, 87(5), 1214-1231. https://doi.org/10.2166/wst.2023.052
16. Awal, R. (2007). Study on landslide dam failure due to sliding and overtopping. Kyoto University. https://core.ac.uk/download/pdf/39199517.pdf
17. You, L., Li, C., Min, X., & Xiaolei, T. (2012). Review of dam-break research of earth-rock dam combining with dam safety management. Procedia Engineering, 28, 382–388. https://doi.org/10.1016/j.proeng.2012.01.737
18. Jiang, X., Meng, J., Fan, B., Zhao, C., Zheng, Y., Xiao, Q., Zhang, C., & Ma, D. (2023). Comparative analysis and risk assessment of dam-break floods: Taking Pingshuijiang Reservoir as an example. Hydrology Research, 54(2), 265–275. https://doi.org/10.2166/nh.2023.129
19. Costa, J. E., & Schuster, R. L. (1987). The formation and failure of natural dams. US Geological Survey Open-File Report 87-392, US Geological Survey, Vancouver, Washington. Retrieved from https://pubs.usgs.gov/of/1987/0392/report.pdf
20. Hancock, G. R., & Coulthard, T. J. (2022). Tailings dams: Assessing the long-term erosional stability of valley fill designs. Science of The Total Environment, 849. https://doi.org/10.1016/j.scitotenv.2022.157692
21. Shu, A., Wang, L., Zhu, F., Zhu, J., Pi, C., Zhang, Z., & Christian, H. (2022). Hydrodynamic process of partial and en masse dam failure induced debris flows. Frontiers in Environmental Science, 10, 905499. https://doi.org/10.3389/fenvs.2022.905499
22. Xu, F., Zhou, H., Zhou, J., & Yang, X. (2012). A mathematical model for forecasting the dam-break flood routing process of a landslide dam. Mathematical Problems in Engineering, 12. https://doi.org/10.1155/2012/139642
23. Prakash, M., Rothauge, K., & Cleary, P. W. (2014). Modelling the impact of dam failure scenarios on flood inundation using SPH. Applied Mathematical Modelling, 38(23), 5515-5534. https://doi.org/10.1016/j.apm.2014.03.011
24. Yang, Q., Guan, M., Peng, Y., & Chen, H. (2020). Numerical investigation of flash flood dynamics due to cascading failures of natural landslide dams. Engineering Geology, 276. https://doi.org/10.1016/j.enggeo.2020.105765
25. Korup, O., Strom, A., & Weidinger, J. (2006). Fluvial response to large rock-slope failures: Examples from the Himalayas, the Tien Shan, and the Southern Alps in New Zealand. Geomorphology, 78(3-4), 3-21. https://doi.org/10.1016/j.geomorph.2006.01.020

26. Pittman, J.M. (1917). Tigra Dam Failure, Gwalior, India-A Case of Sedimentary Sliding. Schnabel Engineering. Retrieved from https://damsafety.org/sites/default/files/Pittman%20Jonathan-decade%20dam.pdf
27. Rogers, J. D. (2006). Lessons learned from the St. Francis Dam failure. Geo-Strata, 2, 14-17. https://web.mst.edu/~rogersda/st_francis_dam/lessons_learned_from_the_st_francis_dam_failure(geostrata_mar-apr_2006).pdf
28. Moehne Dam. (1943). Bombing Moehne Dam Germany. https://caspir.warplane.com/eventdetail/eventid/3003000871943-05-17/
29. Duffaut, P. (2013). The traps behind the failure of Malpasset arch dam, France, in 1959. Journal of Rock Mechanics and Geotechnical Engineering, 5(5), 335-341. https://doi.org/10.1016/j.jrmge.2013.07.004
30. Nema, M. K., Mishra, P. K., & Jain, S. K. (2022). Dam decommissioning: An option for India's ageing water storage infrastructures. International Commission on Large Dams (INCOLD), New Delhi. http://www.incold.co.in/conf_2022/Papers/Dam%20decommissioning%20An%20option%20for%20India%E2%80%99s%20ageing%20water%20storage%20infrastructures.pdf
31. Ward, S. N., & Day, S. (2011). The 1963 landslide and flood at Vaiont reservoir Italy: A tsunami ball simulation. Italy Journal of Geoscience, 130(1), 16-26. https://websites.pmc.ucsc.edu/~ward/papers/Vaiont.pdf
32. Stava. (1985). The El Cobre Tailings dam failure, 1965. Stava. Retrieved from https://www.stava1985.it/the-el-cobre-disaster-chile/?lang=en
33. Carter, J. M., Williamson, J. E., & Teller, R. W. (1972). The 1972 Black Hills-Rapid City Flood Revisited. USGS Fact Sheet FS-037-02, U.S. Geological Survey, Rapid City, SD. Retrieved from https://pubs.usgs.gov/fs/fs-037-02/pdf/fs-037.pdf
34. Bai, S. N., & Zhen, Z. S. (2014). Study on the seepage defect at the connection of the overflow dam and the earth dam of Banqiao Reservoir. Advanced Materials Research, 3465, 287-291.
35. Arthur, H. G. (1977). Teton Dam Failure. In The Evaluation of Dam Safety: Engineering Foundation Conference Proceedings. ASCE, New York, New York, 61-71.
36. Solava, & Delatte. (2003). Teton Dam failure case study: Lessons from the failure of the Teton Dam. In Proceedings of the 3rd ASCE Forensics Congress, October 19 - 21, 2003, San Diego, California. Retrieved from https://faculty.washington.edu/kramer/521/TetonDamDescription.pdf
37. Coleman, N. M. (2018). Johnstown's Flood of 1889 - Power Over Truth and The Science Behind the Disaster. Springer International AG.
38. Luino, F., & Graff, J. V. D. (2012). The Stava mudflow of 19 July 1985 (Northern Italy): A disaster that effective regulation might have prevented. Natural Hazards Earth System Sciences, 12, 1029–1044. https://doi.org/10.5194/nhess-12-1029-2012
39. Simeoni, L., Tosatti, G., Lucchi, G., & Longo, M. (2017). The Stava catastrophic failure of 19th July 1985 (Italy): Technical-scientific data and socioeconomic aspects. Planning and Land Safety, Issue-1.
40. Reddy, D., Kumar, D., Saha, D., & Mandal, M. (2008). The 18 August 2008 Kosi River breach: An evaluation. Current Science, 95(12), 1668-1669.
41. Kafle, K.R., Khanal, S.N., & Dahal, R.K. (2017). Consequences of Koshi flood 2008 in terms of sedimentation characteristics and agricultural practices. Geoenviron Disasters, 4, 4. https://doi.org/10.1186/s40677-017-0069-x

42. Rautela, P. (2013). Lessons learnt from the deluge of Kedarnath, Uttarakhand, India. Asian Journal of Environment and Disaster Management (AJEDM), 5(2). https://rpsonline.com.sg/journals/101-ajedm/2013/0502/S1793924013002824.php
43. Allen, S. K., Rastner, P., Arora, M., Huggel, C., & Stoffel, M. (2015). Lake outburst and debris flow disaster at Kedarnath, June 2013: hydrometeorological triggering and topographic predisposition. Landslides. https://gaphaz.org/files/publications/allen_kedarnath_glof_landslides15.pdf
44. Lindell, M. K., Arlikatti, S., & Huangc, S. K. (2019). Immediate behavioral response to the June 17, 2013 flash floods in Uttarakhand, North India. International Journal of Disaster Risk Reduction, 34, 129–141. https://doi.org/10.1016/j.ijdrr.2018.11.011
45. ICIMOD. (2019). Learning from a disaster event: Investigating the 2018 Panjshir flood in Afghanistan. Mountain Environment Regional Information System. Retrieved from https://www.icimod.org/success-stories/learning-from-a-disaster-event-investigating-the-2018-panjshir-flood-in-afghanistan/
46. Rotta, L., Alcantara, E., Park, E., Negri, R., Lin, Y., Bernardo, N., & Mendes, T. (2020). The 2019 Brumadinho tailings dam collapse: Possible cause and impacts of the worst human and environmental disaster in Brazil. International Journal of Applied Earth Observation and Geoinformation, 90, 102119. https://doi.org/10.1016/j.jag.2020.102119
47. Cheng, D., Cui, Y., Li, Z., & Iqbal, J. (2021). Watch out for the Tailings Pond, a Sharp Edge Hanging over Our Heads: Lessons Learned and Perceptions from the Brumadinho Tailings Dam Failure Disaster. Remote Sensing, 13, 1775. https://doi.org/10.3390/rs13091775
48. Down-To-Earth. (2019). Ratnagiri dam breach: Flooding causes 44% of dam failures in India. Retrieved from https://www.downtoearth.org.in/news/water/throwback-how-china-s-sponge-cities-aim-to-re-use-70-of-rainwater-65399
49. BBC. (2021, February 8). Uttarakhand dam disaster: Race to rescue 150 people missing in India. BBC News. Archived from the original on February 9, 2021. Retrieved February 8, 2021.
50. NBC. (2023). Bodies wash ashore in Libya as devastated city races to count its dead. NBC News. Archived from the original on 2023-09-14. Retrieved 2023-09-14.
51. Johnson, F.A., & Illes, P. (1976). A Classification of Dam Failures. Waterpower and Dam Construction, 28(12), 43-45.
52. Singh, K. P., & Snorrason, A. (1982). Sensitivity of outflow peaks and flood stages to the selection of dam breach parameters and simulation models. University of Illinois, State Water Survey Division, Surface Water Section.
53. MacDonald, T. C., & Langridge-Monopolis, J. (1984). Breaching characteristics of dam failures. Journal of Hydraulic Engineering, 110(5), 567–586. https://doi.org/10.1061/(ASCE)0733-9429(1984)110:5(567)
54. Petra Check, A. W., & Sadler, P. A. (1984). Routing of dam break floods. International Waterpower & Dam Construction, 36, 29-32.
55. Singh, K. P., & Snorrason, A. (1984). Sensitivity of outflow peaks and flood stages to the selection of dam breach parameters and simulation models. Journal of Hydrology, 68(1-4), 295-310.
56. Froehlich, D. C. (1987). Embankment-Dam Breach Parameters. In Hydraulic Engineering, Proceedings of the 1987 National Conference, ASCE, Williamsburg, VA (pp. 570 - 575).
57. Wurbs, R. A. (1987). Dam breach flood wave models. Journal of Hydraulic Engineering, 113, 29-46.

58. Singh, V. P., Scarlatos, P. D., Collins, J. G., & Jaurdan, M. R. (1988). Breach erosion of earthfill dams (BEED) model. Natural Hazards, 1, 161-180.
59. Von Thun, J. L., & Gillette, D. R. (1990). Guidance on breach parameters. Unpublished internal document, U.S. Bureau of Reclamation, Denver, CO.
60. Dewey, R. L., & Gillette, D. R. (1993). Prediction of Embankment Dam Breaching for Hazard Assessment. In Proceedings, ASCE Specialty Conference on Geotechnical Practice in Dam Rehabilitation, Raleigh, North Carolina, April 25-28, 1993.
61. Horritt, M.S., & Bates, P.D. (2002). Evaluation of 1D and 2D Numerical Models for Predicting River Flood Inundation. Journal of Hydrology, 268, 87-99. https://doi.org/10.1016/S0022-1694(02)00121-X
62. Merritt, W. S., Letcher, R. A., & Jakeman, A. J. (2003). A review of erosion and sediment transport models. Environmental Modelling & Software, 18(8–9), 761-799. https://doi.org/10.1016/S1364-8152(03)00078-1
63. Yang, J., Townsend, R., & Daneshfar, B. (2006). Applying the HEC-RAS model and GIS techniques in river network floodplain delineation. Canadian Journal of Civil Engineering - CAN J CIVIL ENG, 33, 19-28. https://doi.org/10.1139/l05-102
64. Bani Hashemi et al. (2008). 2-dimension dam failure model by Fred and Mac Cormac approach. In 4th national conference of Civil Engineering, May 2008, University of Tehran, Iran. Retrieved from https://www.jmaterenvironsci.com/Document/vol6/vol6_N11/363-JMES-2015-Soleymani.pdf
65. Montazeri naming, et al. (2008). Simulation of the wave caused by dam failure through 1- and 2-dimension models; case study: Maroon Dam. In 4th National Conference of Civil Engineering, University of Tehran, Tehran.
66. Abareshi, M., Hosseini, S. M., & Jafarzade, M. R. (2010). Studying the risks of Taragh dam failure. In Fifth national conference of Civil Engineering, May 4-6, 2010, Ferdowsi University of Mashhad, Mashhad, Iran.
67. Esmaili, K., & Abbasi, B. (2010). Modeling of Dam Hydraulic Failure caused by sudden flood through Fluent software. In Fifth national conference of Civil Engineering, 4-6 May 2010, Ferdowsi University of Mashhad, Mashhad, Iran.
68. Ahmadi, & Toufani. (2011). Numerical modeling of dam gradual failure. In 6th national conference of Civil Engineering, April 26-27, 2011, Semnan University, Iran.
69. Timbadiya, P. V., Patel, P. L., & Porey, P. (2012). HEC-RAS based hydrodynamic model in prediction of stages of lower Tapi river. ISH Journal of Hydraulic Engineering, 17. https://doi.org/10.1080/09715010.2011.10515050
70. Godariz et al. (2013). Analyzing risk and uncertainty of earthen dam; case study: Doroudzan Dam in Fars province. Iran water research journal, fall and winter 2013, Shahr e- Kurd University.
71. Nejad, M., et al. (2014). Dam failure and its resulting wave propagation through using finite volume numerical method. Quarterly of Environment and Civil Engineering, University of Tabriz.
72. Seiyfi Zade et al. (2014). Studying Polroud dam failure caused by passing and flood routing at downstream. Research Journal of Watershed Management, Sciences and Natural Resources University, Sari.
73. Aureli, F., Dazzi, S., Maranzoni, A., Mignosa, P., & Vacondio, R. (2015). Experimental and numerical evaluation of the force due to the impact of a dam-break wave on a structure. Advances in Water Resources, 76, 29–42.

74. Kocaman, S., & Cagatay, H. (2015). Investigation of dam-break induced shock waves impact on a vertical wall. Journal of Hydrology, 525, 1–12. https://doi.org/10.1016/j.jhydrol.2015.03.048
75. Wood, A., & Wang, K. (2015). Modeling dam-break flows in channels with 90-degree bend using an alternating-direction implicit based curvilinear hydrodynamic solver. Computers & Fluids, 114, 254–264.
76. Dottori, F., Salamon, P., Bianchi, A., Alfieri, L., Hirpa, F. A., & Feyen, L. (2016). Development and evaluation of a framework for global flood hazard mapping. Advances in Water Resources, 94, 87–102. https://doi.org/10.1016/j.advwatres.2016.05.002
77. Vermee, S., Sachin, & Patra, K. C. (2022). Dam break flow simulation model for preparing emergency action plans for Bargi Dam failure. In R. Jha, V. P. Singh, V. Singh, L. B. Roy, & R. Thendiyath (Eds.), Hydrological modeling (Water Science and Technology Library, Vol. 109). Springer. https://doi.org/10.1007/978-3-030-81358-1_21
78. Palú, M. C., & Julien, P. (2020). Test and improvement of 1D routing algorithms for dam-break floods. Journal of Hydraulic Engineering, 146(6). https://doi.org/10.1061/(ASCE)HY.1943-7900.0001755
79. Li, C., Gao, H., Xu, Z., & Huang, Y. (2021). Sensitivity Analysis of Rock-Fill Dam Break Flood on Different Dam Break Durations. Open Journal of Safety Science and Technology, 11(3), 90-100. https://doi.org/10.4236/ojsst.2021.113008
80. Adityawan, M. B., Sandi, C., Harlan, D., Farid, M., Kuntoro, A. A., Widyaningtias, X. X., Chaidar, A. N., & Nugroho, J. (2023). Numerical modeling of dam break induced flow through multiple buildings in an idealized city. Results in Engineering, 18. https://doi.org/10.1016/j.rineng.2023.101060
81. Annunziato, A., Guney Dogan, G., & Yalciner, A. C. (2023). Modeling dam break events using shallow water model. Eng, 4, 1851-1870. https://doi.org/10.3390/eng4030105
82. DHI. (2023). MIKE HYDRO RIVER user guide. MIKE Powered by DHI. https://manuals.mikepoweredbydhi.help/latest/Water_Resources/MIKEHydro_River_UserGuide.pdf
83. HEC. (2014). Using HEC-RAS for Dam Break Studies, Training Document-39. U.S. Army Corps of Engineers, Hydrologic Engineering Center, 609 Second Street, Davis, CA. Retrieved from https://www.hec.usace.army.mil/publications/TrainingDocuments/TD-39.pdf
84. HEC. (1980, June). Flood Emergency Plans - Guidelines for Corps Dams, RD-13. U.S. Army Corps of Engineers, Hydrologic Engineering Center, 609 Second Street, Davis, CA. Retrieved from https://www.hec.usace.army.mil/confluence/rasdocs/ras1dtechref/latest/performing-a-dam-break-study-with-hec-ras/estimating-dam-breach-parameters/estimating-breach-parameters
85. USACE. (2007). HEC-ResSim-Reservoir system simulation, user's manual (Ver-3). U.S. Army Corps of Engineers, Hydrologic Engineering Center, 609 Second Street, Davis, CA. Retrieved from https://www.hec.usace.army.mil/Software/hec-ressim/documentation/HEC-ResSim_30_UsersManual.pdf
86. FERC. (1988, February 22). Notice of Revised Emergency Action Plan Guidelines. United States Federal Energy Regulatory Commission (FERC), USA. https://www.ferc.gov/sites/default/files/2020-04/02-22-88.pdf
87. Fread, D. L. (2006). Course notes on "Dam Break Floods". National Weather Service, NWS. U.S. Army Corps of Engineers, Hydrologic Engineering Center, 609 Second Street, Davis, CA.

88. Froehlich, D. C. (1995a). Embankment Dam Breach Parameters Revisited. In First International Conference, Water Resources Engineering, Environmental and Water Resources Institute (EWRD), 14 - 18 August 1995. ASCE, Water Resources Engineering Proceeding (pp. 887 - 891).
89. Froehlich, D. C. (1995b). Peak Outflow from Breached Embankment Dam. ASCE Journal of Water Resources Planning and Management, 121(1), 90 - 97.
90. Pareta K. 2023. Hydrological modelling of largest braided river of India using MIKE Hydro River software with rainfall runoff (RR), hydrodynamic (HD) and snowmelt modules. Journal of Water and Climate Change. Vol. 14(4), 1314, pp. 1-25. https://doi.org/10.2166/wcc.2023.484
91. Lompi, M., Mediero, L., Soriano, E., & Caporali, E. (2023). Climate change and hydrological dam safety: A stochastic methodology based on climate projections. Hydrological Sciences Journal, 68(6), 745-763. https://doi.org/10.1080/02626667.2023.2192873
92. Schultz, B. (2002). Role of Dams in Irrigation, Drainage and Flood Control. International Journal of Water Resources Development, 18(1), 147-162. https://doi.org/10.1080/07900620220121710
93. Xu, F., Yang, X., & Zhou, J. (2017). Dam-break flood risk assessment and mitigation measures for the Hongshiyan landslide-dammed lake triggered by the 2014 Ludian earthquake. Geomatics, Natural Hazards and Risk, 8(2), 803-821. https://doi.org/10.1080/19475705.2016.1269839

© 2024 by the authors. Licensee SCU, Ahvaz, Iran. This article is an open access article distributed under the terms and conditions of the Creative Commons Attribution 4.0 International (CC BY 4.0 license) (http://creativecommons.org/licenses/by/4.0/).

Journal of Hydraulic Structures

Volume 10 – Issue 1 – January 2024

Contents:

01 Using PAT for Energy Recovery and Pressure Reduction in Water Distribution Networks

Hamed Mohammadi; Mahnaz Ghaeini-Hessaroeyeh; Ehsan Fadaei-Kermani

13 Experimental evaluation of dune formation downstream of pier scour hole with upstream debris accumulation

Ali Mahdian Khalili; Pouria Akbari Dadamahalleh; Mehdi Hamidi

29 Investigating the settlement of the stone boulders breakwater located on the marine soft fine-grained soil

Amin Falamaki; Amir Hossein Shafiee; Jamal al-Din Iranmahboob; Farzad Arjmand

46 Investigation of the Performance of Soft Computing Methods in the Hydraulic Evaluation of the Slot Fishway on the Inclined Drop

Ehsan Aminvash; Farhoud Kalateh; Rasoul Daneshfaraz; John Abraham

66 Numerical Study of Permanent Deformations of Embankment dams under Seismic Loading, A case study of Kheyrabad Dam

Hydraulic Response to Geometry: Finite Element Modeling of Underground Spaces in Saturated Environments

80 Integrated Hydrodynamic Modeling of Dam Failure and Downstream Flood Inundation near Kathmandu, Nepal using MIKE Hydro River Model

Kuldeep Pareta

Shahid Chamran University of Ahvaz